RADIO POLARIMETRIC IMAGING OF THE SOLAR CORONA AT LOW FREQUENCIES

A Thesis
Submitted for the Degree of
Doctor of Philosophy (Technology)

Submitted by
ANSHU KUMARI

Department of Applied Optics & Photonics
University College of Technology
University of Calcutta

December 2019

To my Parents

Abstract

The coronal magnetic field (B) plays an important role in the formation, evolution, and dynamics of the small, as well as large scale structures in the solar corona. Measurements of the coronal magnetic field strengths, particularly in the radial distance range $\approx$ 1.1 - 3.0 $R_\odot$ ($R_\odot$ is the radius of photospheric Sun) is presently difficult because of practical reasons. Polarization observations, by measuring the Stokes-V parameter of the received radio signal, are generally used as a tool to measure the magnetic field strength associated with the radio emission; the latter is one of the widely pursued areas of research in the solar coronal physics, in addition to the currently available but limited methods of estimating the magnetic field strength using simultaneous radio imaging and spectral observations. Ground based radio observations provide an excellent tool to observe and study the corona in the aforesaid height range.

Therefore, the primary objectives of this thesis are to :

1. design, develop and characterize spectro-polarimeter that can receive the polarized radio emission (at low frequencies) from the Sun with high temporal, spectral resolution, etc.;
2. compare the data obtained using the new instruments with the existing instruments in order to improve the observing capabilities of new instruments;
3. estimate the magnetic field strengths from the observed polarized radio emission associated with various forms of solar coronal activities observed at other wavelength parts of the electromagnetic spectrum.

As for the first objective is concerned, **I designed and developed** two spectro-polarimeters :

i Near ionospheric cut-off frequency spectro-polarimeter that can operate over 15 - 85 MHz frequency range.

ii Wide-band spectro-polarimeter that can operate over 50 - 500 MHz frequency range.

For the first spectro-polarimeter system, **I designed and characterized** a Log-Periodic Dipole Antenna (LPDA) that works in the 15 - 85 MHz range. The VSWR (Voltage Standing Wave Ratio) of the antenna is $\leq$ 3.0 throughout the band. It has a directional gain of 6 dBi and has an effective collecting area of $\approx 0.3\lambda^2$. Two identical antennas were fabricated and kept in mutually orthogonal orientations to arrange the frontend. Since the signal strength received by the

antennas from the background sky were found to vary drastically over the observing bandwidth it was difficult to handle the entire frequency band with a single digital backend system. Therefore, the signal was split into two sub-bands (15 - 25 MHz & 25 - 85 MHz) using appropriate filters designed as part of the thesis work. The signals were then amplified using Low Noise Amplifier (LNA) and were fed to a digital backened receiver. The latter consists of an Analog to Digital Converter (quad ADC) and a Field Programmable Gate Array (FPGA). **I have characterized the ADC** for its linear range of operation, signal-to-noise ratio (SNR), spurious free dynamic range (SFDR), etc. The FPGA used in the digital receiver is ROACH (Reconfigurable Open Architecture Computing Hardware) designed by CASPER community[1]. The spectro-polarimeter was implemented **by me on ROACH FPGA to process** the signals real time using Fast Fourier transforms (FFT), polyphase filter banks (PFBs), correlators, etc. The data acquisition system consists of a vector accumulator, packetizer, and a 10 Gbe data transfer module and a PC. As a part of calibration, the Galactic Center (GC) was observed with the entire system and the Stokes-I and Stokes-V flux profiles were obtained. MATLAB and Python codes were written to analyze the observed spectro-polarimetric data.

The spectra obtained with the FPGA based system and the old Spectrum Analyzer (SA) based spectro-polarimeters were compared to study the performance of the former. **The SA is a product of M/s. Agilent Technologies. I have developed the data acquisition program for recording the signal from the antenna system desgined by me.** In that study, it was found that the SNR of the FPGA system was 10 times better than the SA system. Also, the new instrument was able to detect weak bursts in the presence of strong bursts as the dynamic range ($\approx$ 48 dB) got improved in addition to sensitivity ($\approx 10^{-6}$ mW). Comparison for the latter was done by integrating data from both instruments for a time interval of 1 sec and for a bandwidth of 1 MHz. The FPGA system is better than the SA based system because the latter works on sweep mode using the superheterodyne principle. It takes up to 4 ms to sweep through the observing band and takes $\approx$ 240 ms to write the data; It does not take any observations while writing the data. Whereas the FPGA backend neither sweeps nor has an idle time. So, it fetches more data as compared to SA system during an acquisition period.

For the second spectro-polarimeter system, **I designed and characterized** a

[1] https://casper.ssl.berkeley.edu/wiki/ROACH

compact Cross Polarized Log-Periodic Dipole Antenna (CLPDA) that works in the 50 - 500 MHz range. The VSWR of the antenna is < 2.0 throughout the band. It has a directional gain of about 6.9 dBi, an effective collecting area of $\approx 0.3\ \lambda^2$ and a polarization cross-talk of about -30 dB. The outputs of the CLPDA were amplified using LNAs and were given to Quadrature Hybrid (QH). The latter is a device that has two transmission lines pass close enough to each other for coupling the signal travelling on one line with the other line; This splits the input signal into two parts whose amplitude are nearly equal but with 90^o phase difference between them. The outputs of the QH were given to two commercial SA to record the Stokes-I and Stokes-V flux of the received radio waves. The entire setup was characterized by feeding known linear and circularly polarized signals; The error in the **degree of circular polarization (DCP)** was measured to be ≤ 2 %. Since the FPGA was not available in the beginning, SA based system was developed. But, later on it became available and a FPGA based system was also developed with a spectral and temporal resolution of 100 kHz and 100 ms, respectively. Both systems were calibrated by observing the GC. Then both of them were kept for solar observations to compare their performances. It was found that the SNR of the FPGA based system was higher than the SA based system by 18 dB. Also, the new instrument was able to detect weak bursts in the presence of strong bursts as the dynamic range ($\approx$ 48 dB) got improved in addition to sensitivity ($\approx 10^{-6}$ mW).

With the first spectro-polarimeter, a narrow band (24 - 28 MHz) type-II radio burst was observed on July 23, 2016. It is well known that the type II solar radio bursts are considered to originate from plasma waves excited by magnetohydrodynamic (MHD) shocks and converted into radio waves at the local plasma frequency and/or its harmonics. They are the direct diagnostic of MHD shocks in the solar atmosphere. A closer inspection of the above type II burst indicated that it is split, and appears as two bands (upper frequency band [UFB] and lower frequency band [LFB]). The LFB and UFB bands relate to emission from the coronal regions ahead of and behind the associated MHD shock, respectively. The type II burst was found to have temporal association with a white-light Coronal Mass Ejection (CME) observed by the SOHO/LASCO-C2 and STEREO-A/COR1 coronagraphs. The onset of the type-II burst was almost at the peak time of the Hα and X-ray flares occurred around the same time. Using the spherically symmetric inversion technique, the electron density (N_e) of the background solar corona and during the CME as well were determined using the measured polarized brightness from the

coronagraph data. The values are 0.4×10^6 cm^{-3} and 2.2×10^6 cm^{-3} ($\approx$ 5 times the background electon density), respectively. Combining the background density estimates of the two coronagraphs a 5th order polynomial was fitted to describe the density over the radial distance range 1.5 - 6.4 R$_\odot$. Also from the observed type-II burst data, the electron density corresponding to the observed frequency was determined. Its value is 2.2×10^6 cm^{-3}. Using the electron density model and the drift rate measured from the LFB and UFB of the type-II burst, the velocity of the agent responsible for the generation of type-II was calculated to be $\approx$ 800 km/s. The latter is almost equal to the speed of the associated CME observed with the above mentioned coronagraphs. Since one of the objectives of this thesis work is to estimate the coronal magnetic field strength, using $B(G) = 5.1 \times 10^{-5} v_A f_p$ (v_A is the Alfv́en speed and f_p is the plasma frequency), the strength of the magnetic field was estimated. The value varies from 0.51 to 0.48 ($\pm$ 0.02) Gauss in the radial distance range 2.65 - 2.82 R$_\odot$. The white-light data were also used to estimate B, by following shock stand-off distance method. It was found that $B = 0.32$ G at $r = 3.11$ R$_\odot$ (STEREO-A/COR1) and $B = 0.12$ G at $r = 4.40$ R$_\odot$ (SOHO/LASCO-C2). By combining the radio and white-light measurements of B, a single power-law for B was obtained. As per that $B(r) = 6.7 \times r^{-2.6}$ in the radial distance range 1.8 - 4.6 R$_\odot$. The power-law index is in good agreement with the values published already.

With the SA based second spectro-polarimeter, a type-V burst was observed on May 02, 2016. Type-V bursts are the signature of propagating non-thermal electron beams along curved paths in the solar atmosphere. They are due to synchrotron radiation when the electrons moves spirally in the solar magnetic fields with near relativistic speed. The DCP of the burst was found to vary from 1 % to 6 %. Assuming second harmonic plasma emission, the magnetic field strength was estimated using $B = \frac{f_p \times DCP}{2.8 \times a(\theta)}$, where θ is the viewing angle. The power-law fit to the data points gave $B(r) = 6.3 \times r^{-3.9}$ in the radial distance range 1.1 - 1.9 R$_\odot$.

With the FPGA (ROACH) based second spectro-polarimeter, a high frequency type-II burst (50 - 430 MHz) was observed on November 4, 2015. The bursts were attributed to MHD shocks driven by flare blast waves. GRAPH also imaged the burst at 80 MHz. SOHO/LASCO-C2 running difference image showed the onset of a CME erupted around that time. Wind/WAVES instrument also observed the above burst upto 14 MHz. GOES-15 recorded an M1.9 class soft X-ray flare (and Hα flare as well) from AR 12445 located at N14W64 on the Sun during the

above time. SDO/AIA showed Extreme Ultra-Violet (EUV) wave associated with the above AR. The empirical relation between the frequency of the type-II burst and its radial height, as given by Gopalswamy, was used to determine the electron density. The height vs time details of the CME leading Edge (LE) using white-light data, EUV wavefront LE from SDO/AIA data, location of type-II burst using radio observations, showed a close association between type-II burst and CME LE. The superimposition of shock speed at different instant of time and the X-ray light curve showed that the onset time of type-II is close to the time of maximum shock speed. Also, the consistency in the speeds and the initial agreement between their h–t measurements indicate that the type II burst and the EUV wave are both driven by the same CME. The probable location of the type II burst (when the shock speed was at maximum) was estimated based on its deprojected location and the kinematics of the associated MHD shock. Calculations indicate that the burst should have been located at ≤ 1.12 $R_\odot$. This is reasonably consistent with the location of the CME LE in the SDO/AIA 211 Å image. There is a good correspondence between the time profile of the type-II burst shock speed and the X-ray light curve of the flare. The cross-correlation coefficient between the shock speed and the X-ray flux is ≈ 0.86. Furthermore, the maximum in both cases occurred at almost the same time. And finally the strength of the magnetic field associated with this event was estimated to be ≈ 3 G at about 1.5 $R_\odot$.

Yet another type-II burst was observed on March 16, 2016 with the newly built spectro-polarimeter. The frequency range of the burst is $\approx$ 50 - 90 MHz. The peak DCP varies in the range $\approx$ 8 - 11 %. It has a split-band structure. It is associated with a C2.2 class soft X-ray (SXR) flare (observed with GOES-15 satellite) from the NOAA sunspot active region AR12522 located at N12W83. The optical data were obtained in EUV at 211 Å with the SDO/AIA, and in whitelight with STEREO-A/COR1 and the SOHO/LASCO. COR1 observed a CME around the same time as the type-II burst. SDO/AIA showed a flux rope structure and a diffuse shock ahead of it, beneath the CME location. The radial height of the layers that are responsible for the type-II emission were calculated at 40 and 26.7 MHz; The values are 1.6 and 1.9 $R_\odot$. The corresponding electron densities are 1.98×10^7 cm^{-3} and 8.8×10^6 cm^{-3}, respectively. As mentioned earlier, the spherically symmetric inversion technique was used to calculate the electron density from white-light observations. A power-law fit to all the data points gives $N_e = 2.3 \times 10^8 r^{-5.3}$ in the range $r = 1.6 - 2.2$ $R_\odot$. The same power-law was used to obtain the electron

density over the height (1.1 - 1.3 $R_\odot$) of the flux rope and the values were found to be in good agreement with those published earlier. Combining all the height-time data, the trajectory of the CME was constructed. From the latter, it was inferred that the CME had undergone a high acceleration during its onset phase whereas it is constant in the coronagraph field of view. From the SDO/AIA data, using shock stand-off distance method, the strength of the magnetic field (B) were determined at different radial heights. And, with the band splitting technique, radio spectro-polarimeter data were used to determine B, again at different radial heights. Finally a common power-law was fitted to arrive at a single coronal magnetic field distribution to cover the height range 1.1 - 2.2 $R_\odot$. The equation of the fit is $B(r) = 2.6 \times r^{-2.21}$.

One of the most common radio signature of any flicker on the Sun is a solar type-III burst. The latter are the fast drifting structures in the solar dynamic spectra, which occur when the electrons get accelerated along the open magnetic filed lines in the solar atmosphere. These radio bursts give information regarding electron acceleration along magnetic field lines in the middle corona as well as near-Earth region, which can not be studied currently in any other wavelengths. High spatio-temporal and spectral observations of these bursts obtained with LOFAR (LOw Frequency ARray) were used to study the structure of the open coronal magnetic field lines in the middle corona. On March 30, 2018, there was a B2.1 X-ray flare at active region (AR) 22703, which was recorded by GOES-2 satellite. The radio signature of that activity was observed with e-CALLISTO (Compound Astronomical Low cost Low frequency Instrument for Spectroscopy and transportable Observatory) and LOFAR spectrometers. The radio bursts were imaged with Low Band Antennas (LBAs) of the LOFAR which operates over 10 - 90 MHz. Interferometric tied-array beam imaging observations were carried out with high dynamic range, high spatial resolution between 80 and 20 MHz. The core LOFAR stations were used with spectral and temporal resolution of $\approx$ 195 kHz and $\approx$ 160 ms, respectively. Snapshot synthesis images of five type-III bursts were developed for the analysis. Taurus sky model was used to calibrate the images. The five trails in the spectra seem to follow five different lanes in the solar maps made with the interferometric observations at various times in different frequency channels. The densities at various heliocentric distances for the observed type-III were calculated. The values were comparable to those estimated earlier using white-light and EUV data. Using the observed DCP (25 % – 30 %) and second harmonic approximation,

B was estimated. The spectral index of B was found to vary between 1.6 and 3.4.

The spectro-polarimeter instruments designed in the PhD work may be improved further by increasing the bit resolution of the ADC and increasing the frequency and time resolution. For calibration, a more accurate method can be adopted, for example, circularly polarized emission from the satellites. A realistic approach for real time automatic detection of solar radio bursts can be done on-board. Real time RFI mitigation could be a way to effectively use all the bits in the ADC, to improve the DR of the system further. This would increase the probability of detecting weak bursts. The ROACH based digital spectro-polarimeter backend can serve the first step for developing the new digital backend for polarimetric imaging of the Sun with the augmented-GRAPH. The latter would overcome the limitations such as fixed bandwidth and fixed frequency observations, etc. This FPGA based correlator may be implemented on ROACH-2 board.

Contents

List of Publications

Refereed Journal Articles (related to this thesis)

1. *New Evidence for a Coronal Mass Ejection-driven High Frequency Type II Burst near the Sun*
   Anshu Kumari, R. Ramesh, C. Kathiravan and N. Gopalswamy, 2017, **The Astrophysical Journal**, 843, 10.

2. *Strength of the Solar Coronal Magnetic field - A Comparison of Independent Estimates Using Contemporaneous Radio and Whitelight Observations*
   Anshu Kumari, R. Ramesh, C. Kathiravan and T. J. Wang, 2017, **Solar Physics**, 292, 161.

3. *Addendum to: Strength of the Solar Coronal Magnetic field - A Comparison of Independent Estimates Using Contemporaneous Radio and Whitelight Observations*
   Anshu Kumari, R. Ramesh, C. Kathiravan and T. J. Wang, 2017, **Solar Physics**, 292, 177.

4. *Direct Estimates of the Solar Coronal Magnetic Field Using Contemporaneous Extreme-ultraviolet, Radio, and White-light Observations*
   Anshu Kumari, R. Ramesh, C. Kathiravan, T. J. Wang and N. Gopalswamy, 2019, **The Astrophysical Journal**, 881, 24.

Refereed Journal Articles (not related to this thesis)

1. *The First Low-frequency Radio Observations of the Solar Corona on 200 km Long Interferometer Baseline*
   V. Mugundhan, R.Ramesh, C.Kathiravan, G.V.S Gireesh, **Anshu Kumari**, K. Hariharan, Indrajit V. Barve, 2018, **The Astrophysical Journal Letters**, 855, L08

2. *On the usefulness of existing solar wind models for pulsar timing corrections*
   C. Tiburzi, W. A. Coles, J. P. W. Verbiest, .., **Anshu Kumari**, *et. al.*, 2019, **Monthly Notices of the Royal Astronomical Society**, 487, 394.

Articles under preparation

1. *LOFAR Interferometric Observation of a group of Type III Solar Radio Bursts*
   Anshu Kumari, P. Zucca, R. Ramesh and C. Kathiravan, 2020, **Astronomy & Astrophysics** (under preparation).

2. *Strength of the Coronal Magnetic Fields - A Comparison of Direct & Indirect Methods using Radio Observations*
   Anshu Kumari, R. Ramesh and C. Kathiravan, 2020, **Journal of Astronomy and Astrophysics** (under preparation).

Presentations

Oral Talks

1. *Simultaneous Multi-wavelength observations of a CME on 04th Nov, 2015* at Neighbourhood Astronomy Meeting, Bangalore, India - 2018.

2. *Multi wavelength analysis of type II bursts using space and ground based observations* at COSPAR Workshop, University of Mekele, Ethiopia - 2018.

3. *LOFAR observations of a group of radio type III solar bursts* at ASTRON, The Netherlands - 2018.

4. *Tracing the path of electrons beams in the solar atmosphere using LOFAR observations (Remote)* at CESRA Workshop, 2018.

5. *The Sun as seen in multi wavelength observations* at ISCIIA, Bangalore, India - 2018.

6. *Low Frequency Solar Spectro-polarimeter for Gauribidanur Radio Observatory* at ISCIIA, Bangalore, India - 2018.

7. *Low frequency observations of a type II radio burst* at Astronomical Society of India meeting,, Bangalore, India - 2019.

8. *New Evidence for a Coronal Mass Ejection-driven High Frequency Type II Burst near the Sun* at URSI-APRASC, Delhi, India - 2019.

9. *A radio spectro-polarimeter for monitoring the activities on the Sun* at ISWI Workshop, ICTP, Italy - 2019.

Posters

1. *Cross-Polarized Log-Periodic Dipole Antenna for Low Radio Frequency Solar Observations* at Astronomical Soceity of India Meeting, University of Kashmir, India - 2016 **Best poster award**.

2. *New Evidence for a Coronal Mass Ejection-driven High Frequency Type II Burst near the Sun* at IAU340-Long-term datasets for the understanding of solar and stellar magnetic cycles, Jaipur, India - 2018.

3. *Estimates of Solar Coronal Magnetic Fields with Full Stokes Observations of the Sun using LOFAR* at 9th East-Asia School and Workshop on Laboratory, Space, and Astrophysical Plasmas, Nagoya University, Japan - 2019.

List of Figures

List of Tables

Chapter 1
Introduction

1.1 The Sun

The Sun is a G-type main-sequence star. It is made up of $\sim$ 74.9 % hydrogen (H), $\sim$ 23.8 % helium (He) and $\leq$ 2% of oxygen (O), carbon (C), iron (Fe), and other heavy metals (Ross and Aller, 1976; Stix, 2004). It has a mass of $\sim 1.99 \times 10^{30}$ kg and a radius of $\sim$ 696000 km. The surface temperature of the Sun is $\sim$ 5780 K. We study the Sun as it is the closest star and the main source of energy to the Earth, and the only star that can be observed in detail in almost the entire part of electromagnetic (EM) spectrum. Since the atmosphere of the Sun is a magnetized plasma, it gives us insights about turbulence in plasma medium and its interactions with magnetic fields.

1.1.1 History

The oldest date record of any solar observations traces its path in 12th century BC, when the oldest eclipse record was found (Zirker, 1995) in the ancient city of Ugarit. In 8th century BC, the first time sunspots were recorded (Mossman, 1989). Attempts to measure the Sun-Earth distance was done by Aristarchus of Samosa in the 200 BC. The solar corona, the outermost layer of the Sun, which can only be seen during the solar eclipse, was mentioned by Leo Diaconus in 968 AD (Hetherington, 1996). The first record of a solar prominence dates back to 1185 AD; it was described as 'sudden bursting fires eating a chunk of the sun'. The new theory of Sun put forth by Nicholas Copernicus in 1543 AD established the fact that the Sun is at the centre of all of its planets (Copernicus, 1543). Using several years of accurate observations of planetary motions by astronomer Tycho Brahe, in 1609, Johannes Kepler deduced that all planets orbit in elliptical path around the Sun (Gingerich, 1999). The first telescopic observations of the sunspots were carried out in first decade of 16th century by Galileo Galilei in Italy, Johann Goldsmid in Holland, the Jesuit Christoph Scheiner in Germany and Thomas Harriot in England

[1]. The Sun's mass was first estimated by Isaac Newton in 1687 (Newton, 1987).

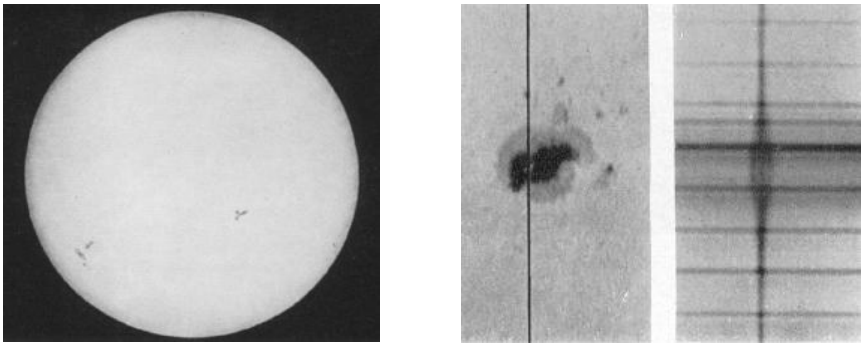

(a) (b)

Figure 1.1: Left panel: The first image of the Sun taken on a photographic plate; Right panel: The magnetically-induced Zeeman splitting in the spectrum of a sunspot (Hale *et al.*, 1919).

In late 1800 AD, William Herschel suggested that the sunspots were locations on the Sun's surface which were cooler than the surroundings. He also suggested that there are invisible (other wavelength) emission from the sun. William Hyde Wollaston observed absorption (dark) lines in the spectrum of the Sun in 1802, which later led to the birth of solar spectroscopy. Joseph von Fraunhofer independently rediscovered these absorption lines, which were later used to infer the composition of the solar atmosphere. In the mid 19th century the sunspot cycle was discovered by Samuel Heinrich Schwabe. J. N. Niepce and Louis Daguerre obtained the first photograph of the Sun in 1845 (see Figure 1.1a). The Sun's differential rotation was explained by Richard C. Carrington and Gustav Spörer, independently in 1858. Carrington also observed the first solar flare (Carrington, 1860). Robert Wilhelm Bunsen and Gustav Kirchhoff identified the chemical composition of the Sun using spectroscopy in 1859. They demonstrated that the Sun's atmosphere has the components which are also present on the Earth. On 18 July 1860 during eclipse, the first solar coronal mass ejection was observed (Eddy, 1974). Undoubtedly, the 19th century was the Golden age for solar astronomy.

The magnetic nature of sunspots were demonstrated by George Ellery Hale in 1908 (Hale, 1908). Figure 1.1b shows Zeeman splitting in sunspot, which indicated the presence of the strong magnetic field inside sunspot. In 1919, G. E. Hale et. al. also gave Hale's polarity laws, which state that large sunspots pairs show opposite polarity patterns; if a positive polarity leads in one cycle then the negative polarity leads in the subsequent cycle (Hale *et al.*, 1919). In 1931, French solar physicist Bernard Lyot designed an instrument called coronagraph with which he emulated an artificial solar eclipse (Lyot, 1939). Then onward the field had progressed dramatically.

[1] https://www2.hao.ucar.edu/Education/SolarPhysicsHistoricalTimeline

1.1.2 The Sun's Interior

1.1.2.1 The Core

The core is a hot, dense central region, which consists of $\sim$ 10% of the Sun's mass, where the energy is produced by 'Hydrogen Burning' i.e. nuclear fusion. It is at a temperature of $\sim$ 16 MK, which makes it adequate for the nuclear fusion reaction to take place. Although several types of fusion reaction exists, the proton-proton reaction is most likely reaction that takes place inside the Sun's core. The nuclear reaction chain wherein two protons fuse to yield deuterium, which further fuses with a third proton to form He^{+3}. The latter fuses with another He^{+3} and form He^{+4}, along with the release of two protons, and energy. This zone consists of $\sim$ 15% of the Sun's interior.

1.1.2.2 The Radiative Zone

The name radiative zone is given to a zone in which the major fraction of energy transport is through radiative processes. The energy is carried outwards by emission and absorption of photons. There is hydrostatic and thermal equilibrium in the plasma. It takes $\approx$ 70,000 years, on average for the energy to get into the next layer, i.e. convection zone. This zone includes nearly 70% of the Sun's interior.

1.1.2.3 The Convective Zone

In this zone, the energy is transported by bulk motions of gas, a process called convection. As the temperature is lesser than the radiative zone, there is formation of highly ionized atoms, hence the plasma becomes optically thick. There is thin layer between the radiative and convective zones, namely 'tachocline'. Due to the temperature gradient and differential rotation, it is believed that the solar magnetic fields are generated here.

The study of the solar interior using observations of waves on the Sun's surface is known as helioseismology[2]. Figure 1.2 shows an illustration of structure of the Sun. Table 1.1 contains the solar interior properties.

Table 1.1: The details of interiors of the Sun.

Zone	Temperature	Density	Energy Transport	Extent
	$\times 10^6$ K	(g cm^{-3})		$R/R_\odot$
Core	15-8	160-10	Radiative	0.0 - 0.25
Radiative	8-0.5	10-0.01	Radiative	0.25 - 0.85
Convective	0.5-0.01	$\leq$ 0.01	Convective	0.85 - 1.00

[2] http://ase.tufts.edu/cosmos/view_chapter.asp?id=24&page=4

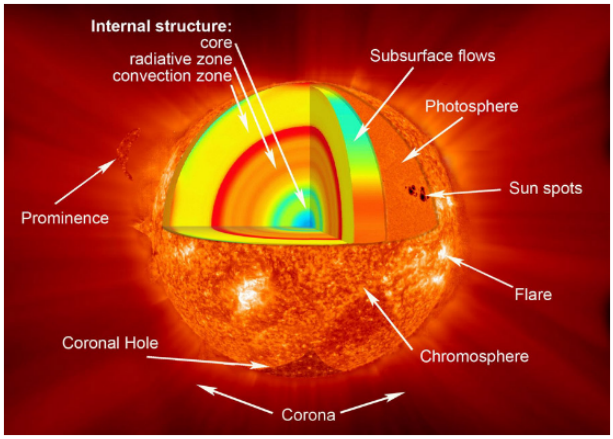

Figure 1.2: Illustration showing the regions of the Sun from interior to outer atmosphere (Courtesy: UCAR).

1.1.3 The Sun's Exterior/Atmosphere

1.1.3.1 The Photosphere

The visible layer of the Sun is known as photosphere. It has a radius of ≈ 696000 km (1 $R_\odot$). The optical depth of this layer is ≈ 1. The surface temperature is ≈ 5780 K and it has an extent of ≈ 500 km. There are various features present on the surface of the Sun, viz

Sunspots - These are the regions of high magnetic field (≈ 1000-2000 G). Due to high magnetic field the convection is inhibited and thus they are cooler (≈ 3500-4000 K) than the surrounding photosphere. Since they are cooler, they appear as dark patches on the photosphere (Cowling, 1933; Stix, 2004).

Granules - They are formed due to the convection pattern. They resemble convection cells where the blobs of plasma rise and fall down on the surface (Orozco Suárez *et al.*, 2008; Stix, 2004). They have a typical size of ∼1500 km and a lifetime of few minutes. Figure 1.3 shows a sunspot and granulation on the solar photosphere.

Supergranules - These are large scale granulation pattern having a horizontal scale of approximately 30,000 km (Rincon and Rieutord, 2018; Stix, 2004). The supergranulation boundaries are associated with kilogauss magnetic fields. It has been shown that several coronal features such as plumes are rooted in the supergranulation boundaries (DeForest *et al.*, 1997).

1.1.3.2 The Chromosphere

The lower region of the solar atmosphere is called the chromosphere; it derives the name from *chroma*, meaning color in Greek, as it appears red during the solar eclipse. Hydrogen emits light in red color (656.3 nm) which can be seen above

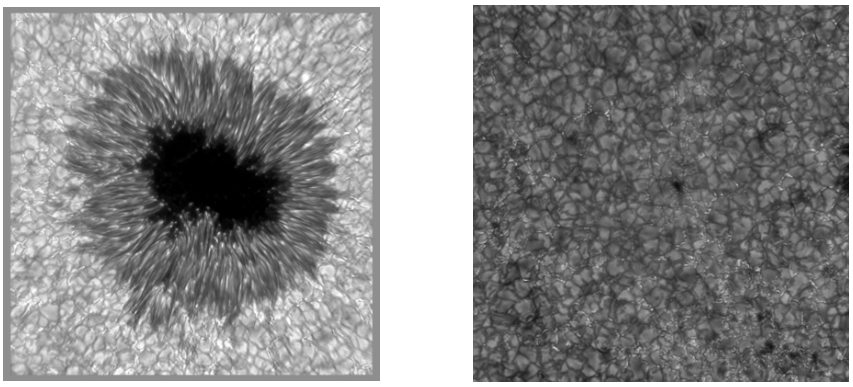

(a) (b)

Figure 1.3: Left panel: Image of a sunspot. The central black area (umbra) and the ring around it (penumbra) together constitute the sunspot; Right panel: The honeycombed structure as seen in the image is known as granules. (courtesy: Leibniz-Institut fuer Sonnenphysik).

the prominences at the time of total solar eclipse. The chromosphere has a spread over ≈ 3000-5000 km and the temperature first decreases to ≈ 4000 K and then increases to ≈ 20000 K towards the transition region. The prominent features in the chromosphere are[3] (Stix, 2004):

Spicules - These are the dense jet of gases ejected from the solar chromoshpere. These are thought to be formed either due to the p-modes leaking from the photosphere or due to the magnetic reconnection. They have a typical lifetime of few tens of seconds.

Filaments - These are dark, large arc of plasma slightly above the Sun's photosphere. These consist of cool plasma hanging in the corona due to the Lorentz force (Kippenhahn and Schlüter, 1957; Stix, 2004). They are thought to be formed due to chromospheric evaporation and thermal instability leading to the condensations of the plasma. The lifetime of filaments can range from hours to days. Filaments mostly form at the polarity inversion lines. Figure 1.4 shows various chromosphere features.

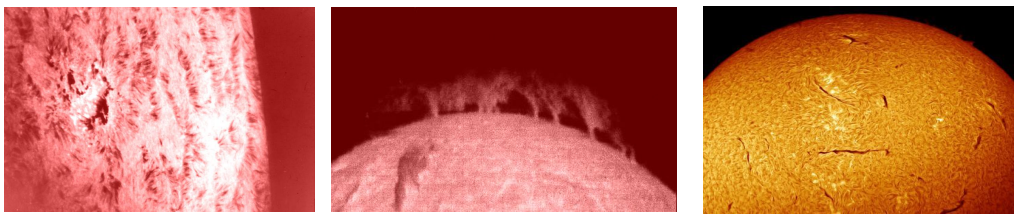

(a) (b) (c)

Figure 1.4: (a) Solar spicules; (b) Solar prominences; (c) Solar Filaments (courtesy: NASA Marshall Space Flight Center).

[3] http://astronomy.swin.edu.au/cosmos/C/Chromosphere

1.1.3.3 The Transition Region

It is a thin layer of ≈ 100 km thickness, where the temperature abruptly raises from 20000 K to 10^6 K. Due to sharp change in density and temperature, this region is crucial for understanding the coronal heating. After the launch of Interface Region Imaging Spectrgraph (IRIS), our understanding of the transition region has completely changed. Several jet-like features, transition region (TR) jets, have been observed (Tian *et al.*, 2014). These jet-like features are associated with propagating disturbances seen in the corona (Pant *et al.*, 2015). Transition region is also important for wave propagation because this is the layer where most of the wave reflection happens due to sharp change in the density. Spectral observations show absorption lines indicating the presence of various heavier metals, e.g. carbon (C), silicon (Si), iron (Fe), etc. Figure 1.5 shows temperature and density variation across the solar atmosphere.

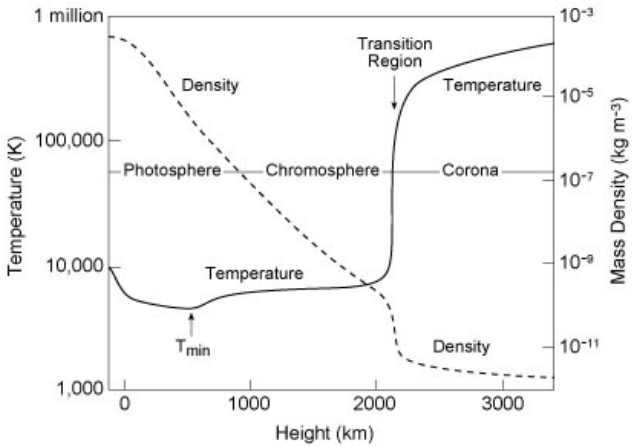

Figure 1.5: The variation of temperature and density in the solar interior and atmosphere (Courtesy: Professor Kenneth R. Lang, Tufts University).

1.1.3.4 The Corona

Corona, the extended outer region of the Sun, is believed to exist from a heliocentric distance of ∼ 1.01 $R_\odot$ to more than 1 AU (Newkirk, 1967; Kaiser *et al.*, 1998; Kojima *et al.*, 2004), and it is a highly tenuous plasma medium with a temperature ≈ 10^6 K. The corona is ∼ 10 million times less dense than the Sun's surface, hence it is not as bright as the solar photosphere. It appears to be a crown to the moon during solar eclipse and hence the name corona. The inner corona is confined to the Sun due to the presence of strong and closed magnetic field lines. There are several conspicuous structures/features present on the corona (Stix, 2004; Aschwanden, 2005); They are

Active Regions - These consist of small regions in the corona where the magnetic fields are strong and responsible for one or many activities. The active regions

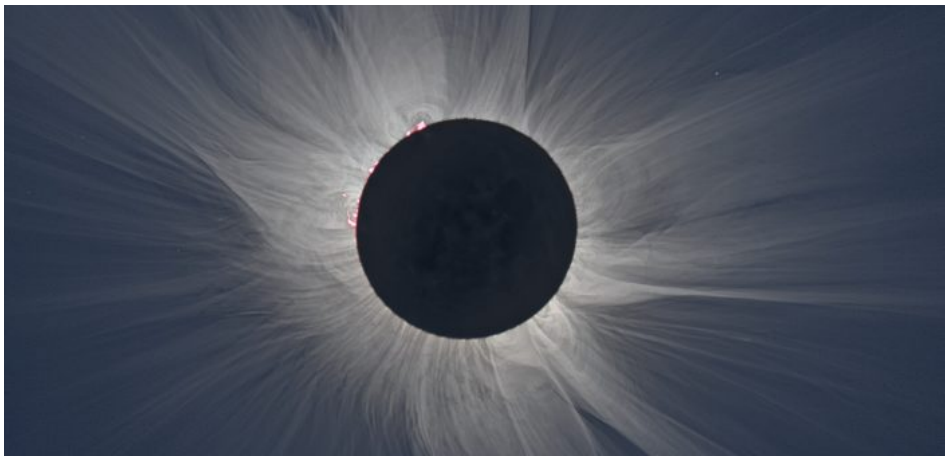

Figure 1.6: The total solar eclipse of 2015 in Svalbard, Norway (Courtesy: S. Habbal, M. Druckmüller and P. Aniol).

are associated with sunspots. These are seen as sunspot groups in visible wavelengths. Active regions have magnetic fields (Aschwanden, 2005).

Quiet Sun - The area free from active regions wherein there is no/minimal activity is known as quiet Sun. However, there are many small scale dynamic processes like nanoflares, heating events etc. continuously goes on in this region. This also harbors large scale structures such as loops and coronal arches.

Streamers - The long-lived large extended structures that are found near the equatorial region, are streamers. They are connected to the active regions. These large cap-like structures are a network of magnetic loops. These are responsible for slow solar wind.

X-ray Jets - The hot plasma flow along open magnetic field lines are called x-ray jets. These jets are thought to be the precursors of coronal plumes. These are visible till the plasma flow fades out.

Coronal Loops - These are bright arc like magnetic field structures of the solar corona. Two footpoints of a coronal loop are associated with different polarities. Coronal loops act like waveguides and harbour several types of waves viz., kink waves, sausage waves, slow waves, etc.

Coronal Holes - These are the open magnetic field line regions near the poles that allow the outflow of coronal gases. They are the sites for fast solar wind. These are darker regions and were first discovered in X-ray.

Solar Wind - The outer region of the corona comprised plasma particles having an average density of 7.1 atoms/cm^3 and that flow at a rate of 200-400 km/sec into the interplanetary space (Kivelson, 1995). Figure 1.7 shows various coronal structures/features.

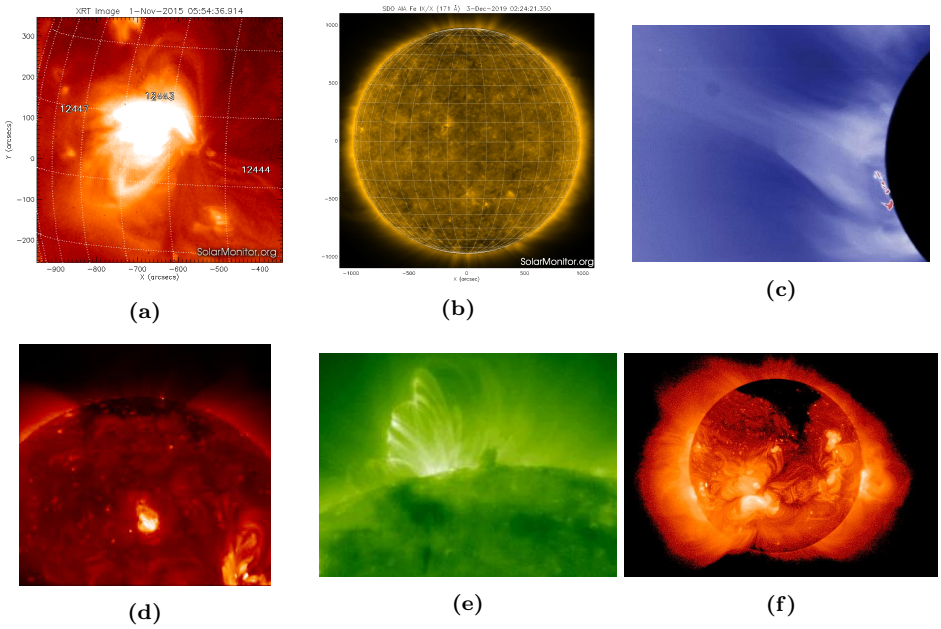

Figure 1.7: Various coronal structures/features: (a) Active region ; (b) Quiet Sun ; (c) Helmet streamers ; (d) X-ray jets ; (e) Coronal loops ; (f) Coronal Holes (courtesy: SolarMonitor, NASA Marshall Space Flight Center. Note that all the images were not taken at the same epoch.

1.1.3.5 Transient mass and energy releases from the corona

Coronal mass ejections (CMEs) - The intermittent injection of huge mass of coronal material from the solar corona into the interplanetary space. CMEs have speed $\sim$ few km/s to few thousands of km/s (Howard *et al.*, 1985; Hundhausen, 1999). They play vital roles in deciding the weather of near-Earth atmosphere, i.e. space-weather. CMEs are important for understanding and predicting the effects of solar activity on the Earth and in space (Kahler, 1992; Gopalswamy, 2006b). If a CME collides with the Earth, it can excite a geomagnetic storm, which can affect on the electrical and communication systems. A large CME can contain a billion tons of matter (Gosling, 1997).

Flares - Any sudden, bright explosion with large amount of energy release in the corona is called flare (Zirin, 1988; Vršnak, 2001). In a short duration (few seconds), they heat material to million degrees and radiate across the entire EM spectrum. If the flare intensity is very high and directed towards the Earth, it can cause radio blackouts. According to **their** X-ray brightness, the solar flares are classified as X, M, C and B class, where X being the most intense and B being the least (Kahler, 1992). Flares also release energetic particles into space which can affect Earth's ionosphere and radio communications (Mitra, 1974; Hudson, 1991). Figure 1.8 shows a massive flare (X1.3 class) and a CME occurred on Sep 7, 2017.

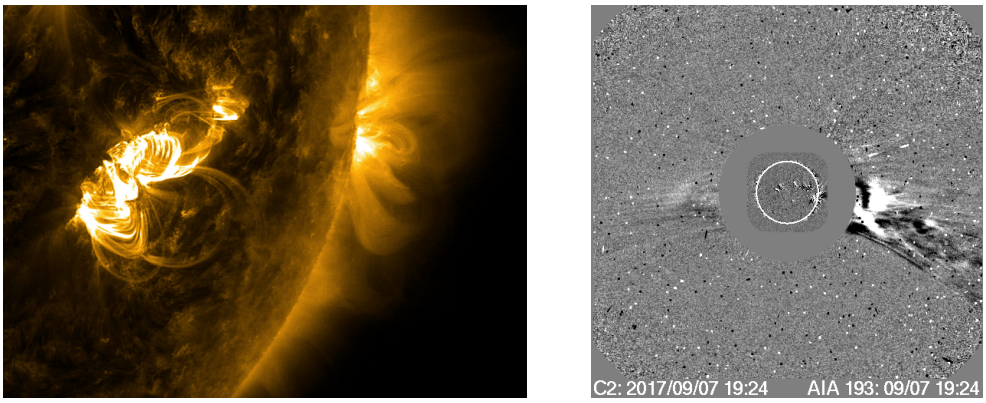

(a) (b)

Figure 1.8: Left panel: A solar flare observed on Sep 7, 2017 in EUV (courtesy: Solar Dynamics Observatory); Right panel: A CME observed with in a whitelight coronagraph on the same day (courtesy: Solar and Heliospheric Observatory).

1.2 Radio Astronomy

Radio frequency band is the second atmospheric window to do astronomy using ground based instruments after visible band (Jansky, 1933; Kraus, 1966; Burke and Graham-Smith, 1996). Radio astronomy unraveled the multi-wavelength astronomy doors which was earlier limited only to visible wavelength part of the spectrum (Reber, 1949). In radio astronomy, the frequencies lie between approximately 10 MHz to 1000 GHz (30 m to 0.3 mm in wavelengths) are used for observing the celestial sources (Monnier, 2003; Rodríguez, 2007). The lower and upper frequency cut-off of the radio window is set by the ionospheric cut-off and the absorption in the the troposphere by molecules, respectively (Wilson, Rohlfs, and Hüttemeister, 2009). After the explanation by James Clerk Maxwell that electromagnetic radiation is associated with electricity and magnetism (Clerk Maxwell, 1865; Clerk Maxwell and Niven, 2011), and it is true for any wavelength, there were several attempts to detect the radio emission from the Sun (Tesla, 1912) but were unsuccessful due to the above frequency cut-off mentioned.

Nevertheless, the attempt was successful when Jansky (1933) from the Bell laboratory, tried to figure out the origin of a source of noise that was showing up in receivers around the 20 MHz region of the radio spectrum. He found that the disturbances were from extra-terrestrial sources (Jansky, 1933) and that opened up the door for radio astronomy. However, the actual radio astronomy had its roots in 1937 when Grote Reber, after learning that Karl Jansky had found radio emission from the milky way galaxy, followed up the study (Reber, 1988). He designed a parabolic dish and receivers for 3300 MHz and 900 MHz but failed to detect any extra-terrestrial radio emission. At the end, he designed a receiver for 160 MHz which detected and confirmed Jansky's results. Figure 1.9 shows the first sky map contours drawn by Reber.

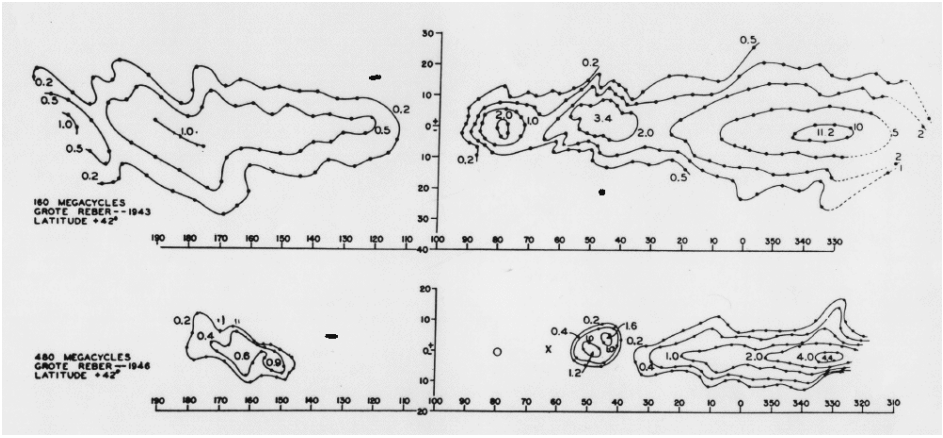

Figure 1.9: Radio contour **map (160 MHz)** showing radio emission from the Milky Way.

Post the work of Reber, Southworth and Hey (1948) observed the radio emission from the Sun. There were other important milestones in radio astronomy i.e. observations of radio emission from the Sun Pawsey, Payne-Scott, and McCready in 1946, solar observations by Ryle in 1948, discrete radio source observed by Bolton in 1948, **sporadic emission from Jupiter at 22 MHz by Burke and Franklin in 1955**, radio radiation from interstellar molecules by Townes in 1957, the serendipitous discovery of CMB by Penzias and Wilson in 1965, pulsars by Hewish in 1970, etc. The pulsars, quasars, radio galaxies, center of the Milky Way galaxy, the Sun, black hole, active galactic nuclei (AGNs), merging galaxy clusters, supernova remnants, cosmic microwave background are the major astronomical sources (Kraus, 1966). The brightest radio source in the sky is the Sun.

1.3 Solar Observations

1.3.1 Multi-wavelength Observations

The Sun exhibits several distinct features that can be studied using multi-wavelength observations (Chiuderi-Drago *et al.*, 1982; Harra-Murnion *et al.*, 1998; Warmuth *et al.*, 2004). The Sun emits almost over the entire visible band of the electromagnetic radiation; for example, Figures 1.10a shows Sun's photosphere, Figure 1.10b shows the Sun's chromosphere and Figure 1.10c shows the Sun's transition region. In Extreme-Ultravoilet (EUV) image or a video, one can see the structures in the transition region, viz. the EIT waves, flux ropes, active regions, etc. (see Figure 1.10d). The X-ray image or a video of the Sun (see Figure 1.10e) reveals that the corona has different types of structures such as coronal holes, loops, jets. The radio observations cover most of the 'inner' and 'middle' corona (see Figure 1.10f).

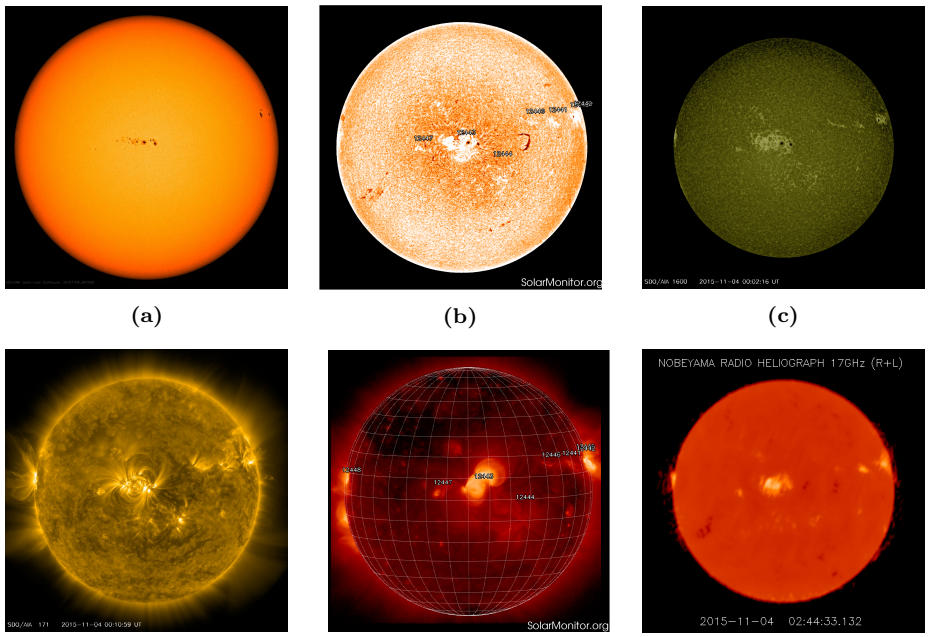

(a) (b) (c)

(d) (e) (f)

Figure 1.10: The Sun as seen in different wavelength: (a) A continuum image of the photosphere with the Solar Dynamics Observatory's (SDO) Helioseismic and Magnetic Imager; (b) The Hα 6562.8 Å image from chromoshpere (Solar Monitor); (c) The transition region image of the Sun with SDO/AIA ; (d) Extreme Ultraviolet image of the Sun (171 Å) with the SDO/AIA; (e) Soft X-Ray image of the Sun with the Hinode spacecraft; (f) The radio Sun at 17 GHz imaged by Nobeyama Solar Radio Observatory. Note that all the images were not taken at the same epoch.

1.3.2 Solar Radio Observations

The radio emission from the Sun can be classified into two types: (1) Thermal emission and (2) Non-thermal emission. The thermal emission is generated by the thermal motion of the charged particles and the radiation energy distribution follows Planck's law. The Non-thermal Emission is generated when the charged particles gyrate along the magnetic field lines in the solar atmosphere, and therefore the energy distribution does not obey Planck's law (Dulk, 1985; McLean and Labrum, 1985b; Shibasaki, Alissandrakis, and Pohjolainen, 2011). The foundation of solar radiophysics was laid by the following physicists **(refer McLean and Labrum (1985b) and the references therein for more details)** :

Heavyside (1904): He showed that the electrons gyrate in the presence of a constant magnetic field. The electron gyration frequency is given as

$$f_B = \frac{eB \times \sqrt{(1-\beta^2)}}{m} \tag{1.1}$$

Here, B is magnetic field, β is relativistic speed of electrons, f_B is gyrofrequency, e and m are charge and mass of the electron.

Lorentz (1909): He showed that plasma behaves as a dispersive medium. According to him, the relationship between the refractive index and the plasma frequency is written as,

$$n^2 = 1 - (f_p/f)^2 \tag{1.2}$$

where f_p and f are plasma and observing frequency, respectively.

Schott (1912): He explained that there would be a harmonic emission from an electron gyrating with f_g frequency. A single relativistic electron of energy E orbiting in a magnetic field of H Gauss radiates a series of harmonics of fundamental frequency,

$$f_1 = f_H \sqrt{1 - \beta^2} \tag{1.3}$$

where f_1 and f_H are fundamental and harmonic frequency, respectively and β is relativistic speed of electron.

Tonks & Langmuir (1929): They stated that an electron behaves as an oscillator in the plasma medium when subjected to linear displacement. Due to plasma processes, the Sun radiates in radio wavelengths, and the emission height and frequency depends upon the electron density of the corona. According to Newkirk (1961) the variation of f_p and heliocentric distance (r) follow equation 1.4,

$$N_e = 42000 \times D \times 10^{4.321/r} \mathrm{cm}^{-3} \tag{1.4}$$

where, N_e is the electron number density, D is the enhancement factor.

There were several important milestones in solar radio astronomy; to name a few: observations of radio emission from the Sun by Pawsey, Payne-Scott, and McCready in 1946, solar radio noise by Allen in 1947, study of the slow drifting radio bursts by Wild and McCready in 1950, continuum burst observations by Boischot in 1957, type II radio bursts by Roberts in 1959, interferometric studies of continuum bursts by Kundu and Firor in 1961, radio spectrum of solar activity by Maxwell, Swarup, and Thompson in 1958.

1.3.3 Solar Radio Bursts

The radio emission from the Sun can be classified into two types, i) the quiet Sun component which is thermal in nature (Piddington and Davies, 1953), and ii) the emission from the active Sun which is non-thermal in nature (Lin and Hudson, 1976). The latter can be of two types, the slowing varying component which is also thermal in nature and comes from the regions above sunspots; and the transient emission, which is known as the rapidly varying component. The first one has a temperature of $\sim 2 \times 10^6$ K, whereas, the second one has temperature anywhere

between $\sim 10^7$ and 10^{12} K (Dulk, 1985). These transients are further classified based on their appearance in the solar dynamic spectra (Wild, Smerd, and Weiss, 1963; Wild and Smerd, 1972). They are:

Type I Bursts - These are also known as noise storms. These bursts last for a few seconds to hours or days (Tapping, 1978). Associated with active regions and flares, these are narrow, short bandwidth enhancements. The normal frequency range of occurrence is $\sim 80 - 200$ MHz (Elgaroy, 1977; Mugundhan *et al.*, 2018).

Type II Bursts - These are often associated with shocks due to CMEs and at times with flare eruptions (Dulk, 1970; Mancuso and Raymond, 2004; Lin, Mancuso, and Vourlidas, 2006; Cho *et al.*, 2013). These are slowing drifting features in the dynamic spectra, which can last for $3 - 30$ minutes. They appear as individual, or fundamental & harmonic pairs or structures with split-band. These normally occur between $15 - 150$ MHz.

Type III Bursts - These are intense fast drifting bursts which occur individually or group and last for a few seconds to few minutes. Often associated with flares and active regions, these bursts have frequency range from few kHz to 1 GHz (Fainberg and Stone, 1970; Kishore *et al.*, 2017; Mugundhan, Hariharan, and Ramesh, 2017).

Type IV Bursts - These are also slow drifting, broadband continuum in the spectra. Their lifetime vary from a few minutes to a few days, depending upon whether they are moving or remaining stationary. These are associated with proton emission, eruptive prominences and magneto hydrodynamic (MHD) shocks (Riddle, 1970; Hariharan *et al.*, 2016), and occur between 20 MHz and 2 GHz.

Type V Bursts - These are very similar to type III bursts and becomes broader at lower frequencies (Suzuki and Dulk, 1985). Associated with active regions and flares, they last from a few sec to few minutes and occur between 10 and 200 MHz.

Figure 1.11 shows the flux density variation of the Sun during active and quiet period.

1.3.4 Radio Observational Facilities

1.3.4.1 Space based Observatories

The observing facilities are either on-board space telescopes or on the ground. The solar spectral data observed from space are classified into type II, type III and type IV, to a large extent. These are signatures of accelerated and trapped electrons by the magnetic fields (Cane and Stone, 1984). These are used to study the electron instabilities in the corona. Radio and Plasma Wave Investigation (WAVES) Solar Terrestrial Relations Observatory on-board WIND spacecraft by Goddard Space Flight Center, National Aeronautics and Space Administration (GSFC/NASA) and the Paris-Meudon Observatory, the University of Minnesota (Bougeret *et al.*, 1995a), is an instrument that can measure such instabilities. WIND/WAVES has three dipole antennas, and five receivers: (1) Low Frequency FFT receiver called

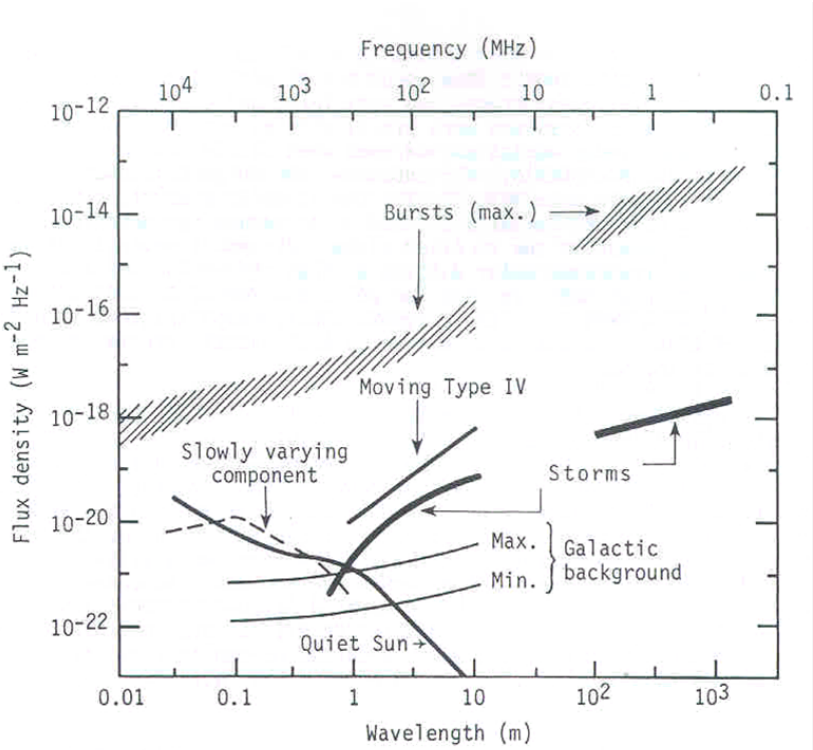

Figure 1.11: The flux density of the radio Sun (as a function of wavelength) during quiet and active phase. The flux density of galactic background is shown for comparison (Courtesy: D. E. Gary).

FFT (0.3 Hz-11 kHz); (2) Thermal Noise Receiver called TNR ($4 - 256$ kHz); (3) Radio receiver band 1 (RAD1) (20–1040 kHz); (4) Radio receiver band 2 (RAD2) ($1.075 - 13.825$ MHz) and (5) the Time Domain Sampler (TDS). This instrument investigates the radio and plasma wave[4] in interplanetary medium. Another instrument is S-WAVES on-board Solar Terrestrial Relations Observatory (STEREO). S-WAVES measures the radio emission from a few kHz up to 16 MHz, with three radio antennas and five receivers[5].

1.3.4.2 Ground based Observatories

The ground based radio observations of the Sun are made with two type of instruments: (1) heliographs and (2) spectrographs. The following are some of the telescopes dedicated to image the Sun. Metsähovi Radio heliograph (MRH; 37 GHz), Nobeyama Radioheliograph (NoRH; 17 & 34 GHz), Siberian Solar Radio Telescope (SSRT; 5.7 GHz), Owens Valley Solar Array (OVSA; 1.2-18 GHz), Nancay Radio Heliograph (NRH; 150-450 MHz), and Gauribidanur RAdioheliograPH (GRAPH; 40-120 MHz). At present, the only dedicated imaging instrument that is in operation to observe the Sun at meter wavelengths is GRAPH. There are **a**

[4] https://wind.nasa.gov/inst_info.php
[5] https://solar-radio.gsfc.nasa.gov/index.html

few other non-dedicated radio telescopes available for observing the Sun. They are Atacama Large Millimeter/submillimeter Array (ALMA; 83 – 936 GHz), Giant Metrewave Radio Telescope (GMRT; 50 – 1500 GHz), LOw Frequency ARray (LOFAR; 10 – 250 MHz). Also, there are several spectrographs, working from few MHz to few GHz around the globe. For example Hiraiso Radio Spectrograph (HiRAS; 25 – 2500 MHz), Culgoora Solar Radio Spectrograph (18 – 1800 MHz), ARTEMIS–Jean Louis Steinberg Radiospectrograph (20 – 650 MHz), Green Bank Solar Radio Burst Spectrometer (18 – 70 MHz), Nancay Decametric Array (10 – 100 MHz), etc[6]. There is a network of Compound Astronomical Low cost Low frequency Instrument for Spectroscopy and Transportable Observatory (CALLISTO) spectrographs commissioned at various parts of the world to monitor the transient solar radio emission. The instrument works at 20 to 800 MHz (but range of operation varies from one observatory to another)[7].

Along with above instruments, there are **a few** more radio instruments in operation to measure the total flux of the Sun at spot frequencies. They are Nobeyama Radio Polarimeters, Solar Submillimeter-wave Telescope (SST), Siberian Radioheliograph (SRH), etc. Despite it has to be pointed out that the spectro-polarimetric observations of the Sun are very rare. The latter are important to study the coronal magnetic field strength associated with various form of coronal activities. Therefore, this thesis intends to develop of high resolution spectro-polarimeter to observe the Sun at low radio frequencies.

1.4 The Gauribidanur Observatory

The first radio observation of the Sun in India was done in the year 1952 at the Kodaikanal Solar Observatory (KSO). The total flux of the Sun was recorded at 100 MHz using Yagi antenna elements and Dicke receiver. Later in 1970s, the recording of solar bursts at 25 MHz was also commenced[8]. The first solar radio noise storm observations were done in 1953 by Das and Bhargava (1953).

In the late 1970s, the Gauribidanur Radio Observatory (GRO) was founded in collaboration with Raman Research Institute (RRI). A 'T' shaped decameter array of 1000 dipoles was built to operate at 34.5 MHz (Sastry, 1989). That array was used to obtain the first synthesis map of the Sun at 34.5 MHz and to study the fine structures in the radio bursts. Gauribidanur Radioheliograph (GRH), the imaging instrument was commissioned in the late 1990s (Ramesh *et al.*, 1998). It was a 'T' shaped interferometer array. The array had 128 log-periodic dipoles antennas (LPDA) in the E-W direction and 64 LPDA in the N-S direction. Every 8 LPDA in the E-W were combined into one group whereas 4 LPDA in the N-S formed a group. Each group signal was correlated with the other using 1024 channel digital

[6] https://www.astro.gla.ac.uk/users/eduard/cesra/?page_id=187
[7] http://www.e-callisto.org/
[8] https://www.iiap.res.in/?q=history.htm

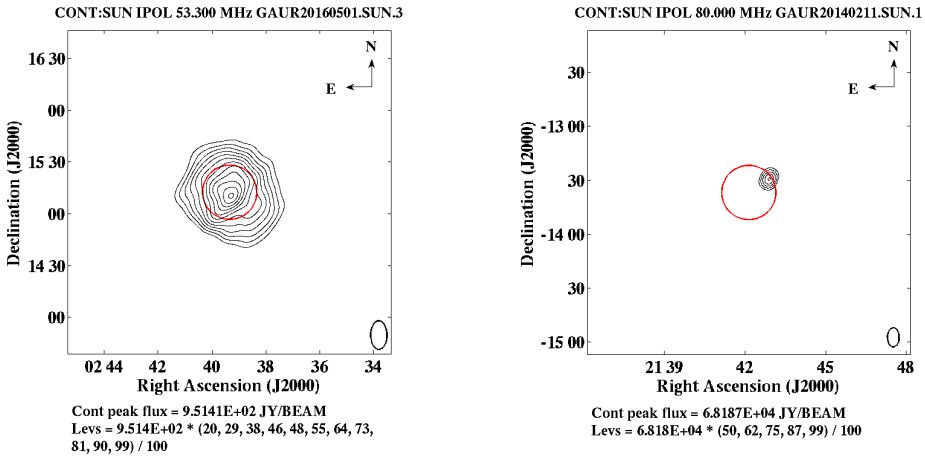

(a) **(b)**

Figure 1.12: a) GRAPH image for the quiet Sun at 53.3 MHz observed on 01 May, 2016. The centre circle represents 1 $R_{\odot}$; (b) GRAPH image for the active Sun at 80 MHz observed on 11 Feb, 2014. During the activity, the intensity increases drastically and hence, the quiet Sun is not visible.

coorelator. The observations were made at few interference free spot frequencies in the 40 - 120 MHz frequency range. The array was expanded in late 2010 and was named as GRAPH. Now it has 396 LPDAs, divided into 64 groups (Ramesh, 2011), with 32 groups each in East-West (EW) and North-South (NS) directions. GRAPH has been used to study the solar coronal transients, quasi-periodic radio emissions (Sasikumar Raja and Ramesh, 2013), 'Halo' CME (Ramesh *et al.*, 2003), magnetic fields of quiet (Ramesh *et al.*, 2006; Kathiravan *et al.*, 2011) and active Sun (Kishore *et al.*, 2017; Kumari *et al.*, 2017c), electron distribution in the corona (Mugundhan *et al.*, 2018), etc.

To study the spectral characteristics of the corona in 30-150 MHz, the Gauribidanur RAdio Solar Spectrograph (GRASS; Ebenezer *et al.*, 2007) was commissioned in 2007. It was an one dimensional (1D) array of 8 LPDAs and the backend was a commercial spectrograph. That was upgraded to the Gauribidanur Low Frequency Solar Spectrograph (GLOSS; Kishore *et al.*, 2014) in 2014, which is now observing the Sun in 40 - 440 MHz. There has been an interferometric polarimeter in operation at GRO. It is called as the Gauribidanur Radio Interferometric Polarimeter (GRIP). It records the total and circular polarized flux from the whole Sun at **a few** interference free spot frequencies. A spectro-polarimeter instrument was commissioned in the year 2014 at GRO. It is called as the Gauribidanur RAdio Spectro-Polarimeter (GRASP; Kishore *et al.*, 2015). It operates in $35 - 85$ MHz range. The spectrograph instruments comprise of superhetrodyne receiver backends. The spectra recorded at any given time has information at only one spot frequency because the receivers work in sweep mode. Figure 1.12 and 1.13 shows

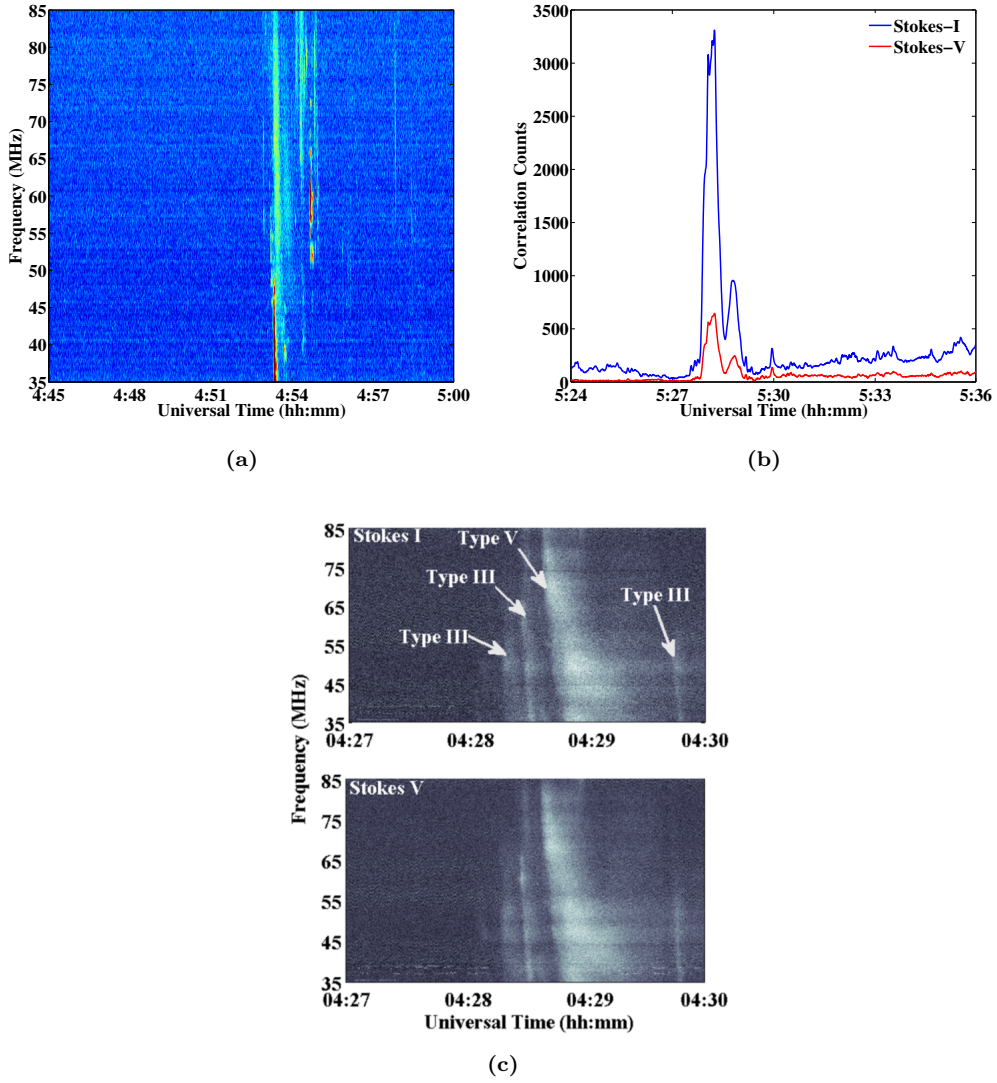

(a) (b)

(c)

Figure 1.13: The spectra obtained with different instruments at GRO: (a) GLOSS spectrum of a type III burst observed on 30 June, 2014; (b) Plot of temporal profiles obtained for a type III burst at 65 MHz with GRIP on 23 June, 2016; (c) GRASP spectra of a group of type III and type V bursts (in Stokes-I and Stokes-V) observed on 14 Dec, 2014.

a few observations obtained with the above mentioned suite of instruments.

1.5 Thesis Objective

1.5.1 Motivation

Corona harbors large scale structures, as multi-frequency observations reveal, such as coronal helmet streamers (white-light), coronal holes (X-ray and EUV), and coronal condensations (radio), etc. (Krucker and Benz, 2000; Aschwanden, 2005). It is recognized to exhibit incessant and inhomogeneous outward flow of plasma

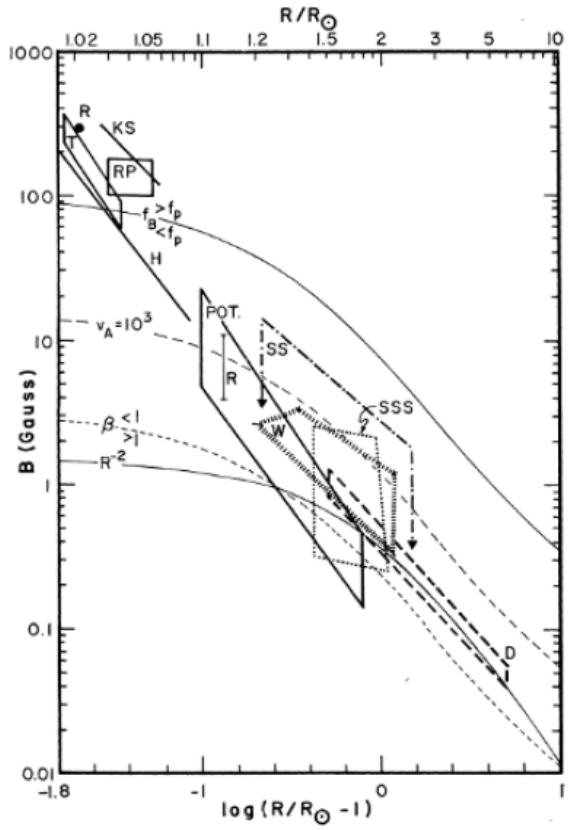

Figure 1.14: The magnetic field distribution in the solar corona (Dulk and McLean, 1978).

material, named solar wind (Gosling *et al.*, 1978; Marsch, 2006), and to exemplify intermittent injection of huge mass of coronal material, called Coronal Mass Ejections (CMEs) (Gosling, 1997), in to the interplanetary medium, and therefore the region appears to be highly dynamic. The onset of CMEs are often preceded / accompanied by H-alpha, X-ray, EUV and radio enhancements and are followed by particle acceleration in the interplanetary space (Gopalswamy *et al.*, 1999). Under conductive circumstances, if Earth happens to be in their way, the solar particles can enter in to Earth's atmosphere and can trigger geomagnetic storms, which can perturb technological systems deployed in the near-Earth space which in turn give rise to severe socio-economic losses to humankind. Therefore safeguarding them by forecasting the near-Earth climate (i.e. called the space weather forecast) becomes inevitable. Theories claim that the large and small scale variation in the spatio-temporal distribution of the magnitude and topology of the magnetic field determine the formation, evolution, lifetime etc. of the above mentioned large-scale structures and **transient** outflows (Sheeley, 1967; Bumba and Howard, 1965). But measurements of the solar coronal magnetic field are presently limited due to practical difficulties (see for e.g., Lin, Penn, and Tomczyk (2000); Tomczyk *et al.* (2008)). It is inferred by extrapolating the observed solar surface magnetic field distribu-

tion using the potential or force-free field approximations (see for e.g. Wiegelmann, Petrie, and Riley (2017)). The estimation of the magnetic field strength (B) in the solar corona is one of the widely pursued areas of research in observational solar physics. Circular polarization observations in the radio frequency range 1 – 20 GHz have been extensively used to measure B above active regions. The corresponding heliocentric distance range is typically $r \approx 1.05 - 1.10$ $R_\odot$ (Gelfreikh, 2004; Ryabov, 2004; White, 2004). Observations of Stokes-V profiles of the coronal emission line Fe XIII λ10747 resulting from the longitudinal Zeeman effect were used by Lin, Penn, and Tomczyk (2000) to estimate B over $r \approx 1.12 - 1.15$ $R_\odot$. These measurements in the radio and optical/infrared regimes are limited to the inner corona ($r \lesssim 1.2$ $R_\odot$). In the outer corona ($r > 3$ $R_\odot$), Faraday rotation observations are generally used to derive the magnetic field (Patzold *et al.*, 1987; Spangler, 2005; Mancuso and Garzelli, 2013b). Compared to these two regions of the corona, estimates of B in the middle corona ($r \sim 1.2 - 3.0 R_\odot$) primarily use different types of transient non-thermal radio emission observed at low frequencies ($\lesssim$ 150 MHz) with ground-based instruments. The radio methods, although indirect in contrast to the Zeeman effect in optical wavelengths, have provided the bulk of the quantitative information on B in this distance range (Dulk and McLean, 1978). Figure 1.14 shows the magnetic field distributions across the corona.

Therefore, this thesis aims to design and develop an observing system to overcome the shortcomings such as temporal and spectral resolution, bandwidth, etc. of the existing systems and thereby improving the determination of coronal magnetic field strength. To realize the system, new wideband (50-500 MHz), low frequency antennas, new digital backends were developed and characterized. The backend was implemented on a Field Programmable Gate Array (FPGA). Real time signal processing using Fourier transforms (FT), polyphase filter banks (PFBs), correlations, etc. were performed on FPGA board. New digital back-end also has the flexibility to detect weak bursts as the dynamic range had increased. The complete system was calibrated, new pipelines were written to reduce and analyze the data. Some of the observations obtained with the new system were used to determine the coronal magnetic field strength.

1.5.2 Thesis Outline

The thesis is structured as follows: In chapter 2, design and development of a very low radio frequency (85 – 15 MHz) spectro-polarimetric instrument has been discussed. Chapter 3 describes a wideband (50 – 500 MHz) antenna front-end and analog back-end designed and developed for spectro-polarimetric observations. This chapter also includes the new digital backend and its performance comparison with the traditional spectrum analyzer based backend. In Chapter 4, analysis and results obtained from the data observed with new instruments are described. Chapter 5 contains the interferometric observations of group of type-III bursts using

tied array beam imaging of the Sun using LOw Frequency ARray (LOFAR). The analysis and results are also given. The thesis is concluded in chapter 6 by listing the advantages of high spectral and temporal digital instruments over conventional low frequency instruments, especially from the point of view of solar observations.

Chapter 2
Low-Frequency (15 - 85 MHz) Spectro-polarimeter

Strength of the Solar Coronal Magnetic field - A Comparison of Independent Estimates Using Contemporaneous Radio and Whitelight Observations
Anshu Kumari, R. Ramesh, C. Kathiravan and T. J. Wang, 2017, **Solar Physics**, 292, 161.

Addendum to: Strength of the Solar Coronal Magnetic field - A Comparison of Independent Estimates Using Contemporaneous Radio and Whitelight Observations
Anshu Kumari, R. Ramesh, C. Kathiravan and T. J. Wang, 2017, **Solar Physics**, 292, 177.

2.1 Introduction

As described in Chapter 1, the Sun is a highly variable source and it continuously emits electromagnetic radiation and energetic particles, at different energy scales, into the inter-planetary space (Zirin, 1988; Beck, 1995; Aschwanden, 2005). Due to abrupt reconfiguration and re-connection of the solar magnetic fields, huge amount of energy is released instantaneously, which triggers events like Flares (Švestka, 1966; Alfvén and Carlqvist, 1967; Lu and Hamilton, 1991), Coronal Mass Ejections (CMEs) (Sheeley *et al.*, 1985; Kahler, 1992; Forbes, 2000) and Solar Energetic Particle (SEPs) (Breneman and Stone, 1985; Reames, 1995) showers. Of these events, CMEs are of particular importance because, when they are earth directed, they trigger geo-magnetic storms (Gosling *et al.*, 1990; Srivastava and Venkatakrishnan, 2002), and affect power and communication grids. When the plasma ejected by a CME propagates through the corona, and if its speed is greater than the local Alfvén speed, a shock wave is created, where electrons are accelerated and radio emission is subsequently produced. This signature, the so-called type II burst (Roberts, 1959; Cliver, Webb, and Howard, 1999), is seen in the dynamic-spectrum as a slowly drifting feature from high frequencies to low frequencies, as it propagates from its point of origin (in the corona) into the interplanetary space. From

the drift-rate of such a burst, the speed of the shock driver can be inferred with the help of an appropriate electron density model and this provides a vista to detect earth-directed CME at least 20 hours (assuming maximum speed of 2000 km/s for a CME) before it impacts the earth.

The radio emission from these events is detected in the meter-wavelengths. The heliocentric distance ranges of these bursts correspond to $\approx 1.6\ R_\odot$ - $3\ R_\odot$ (Kundu and Stone, 1984; Cane and Stone, 1984), the lowest of which can be detected even down to ionospheric cut-off of various places on the Earth. Thus, to probe such bursts that escape into interplanetary space, and to provide complementary observations to space-craft based spectrometers e.g. WAVES experiment[1] on the Wind spacecraft (Bougeret *et al.*, 1995b), we commissioned a new spectro-polarimeter system to monitor radio bursts from the Sun down to the local ionospheric cut-off of our observatory, that occurs at $\approx$ 15 MHz. At the higher frequencies, we monitor up-to 85 MHz, beyond which the RF band is dominated by FM signals. In this chapter, we describe the design, characterization and commissioning of the spectro-polarimeter and observations obtained with it. The observing set-up here consists of low-frequency radio antennas and a receiver system. The following sections describe various components of the entire system.

2.2 Analog Frontend

The design, development and characterization of the antenna, analog and digital receiver components used to build the observing system are described in the following sections and subsections.

2.2.1 Antenna Design

The first component in the observing set-up is a radio antenna. An antenna is a device used to transmit, receive or transceive electromagnetic (EM) radiation (Stutzman and Thiele, 1981). **I have** designed a log-periodic dipole antenna (LPDA; Isbell (1960)), that can operate in the range from $15 - 85$ MHz. The lower cut-off for this antenna is chosen as 15 MHz because that is the observed ionospheric cut-off of the Gauribidanur observatory. The higher cut-off is chosen to eliminate the FM band ($88 - 108$ MHz)[2]. Antenna structures which are defined in terms of angle, rather than their linear dimensions, exhibit frequency independent impedance, gain characteristics,etc (Rumsey, 1966). The reason behind the selection of this particular antenna type is that it can operate over a broad bandwidth (DuHamel and Isbell, 1966). LPDA is a broadband antenna that has uniform characteristics throughout the operational bandwidth (Carrel, 1961; Sasikumar Raja *et al.*, 2013). The design and fabrication of this antenna is described in the next section.

[1] https://solar-radio.gsfc.nasa.gov/wind/index.html
[2] https://en.wikipedia.org/wiki/FM_broadcast_band

2.2.1.1 Design and fabrication of LPDA

I extensively used Carrel's empirical relations (Carrel, 1961) for designing the antenna. Figure 2.1 shows the schematic of a LPDA for which the lowest and highest frequencies, f_1 and f_n, respectively are related in a fashion as, $f_1 = \tau^{n-1}/f_n$, where τ is a constant, known as geometric constant and is one of the design parameters. The relationship between adjacent dipole arms, L_n and L_{n-1}, the spacing between them, d_n and their distance from the apex, R_n of a LPDA is given in equation 2.1. The length of longest arm is equal to half of the maximum wavelength λ_1 of operation.

$$\tau = \frac{L_{n-1}}{L_n} = \frac{R_{n-1}}{R_n} = \frac{d_{n-2}}{d_{n-1}} \tag{2.1}$$

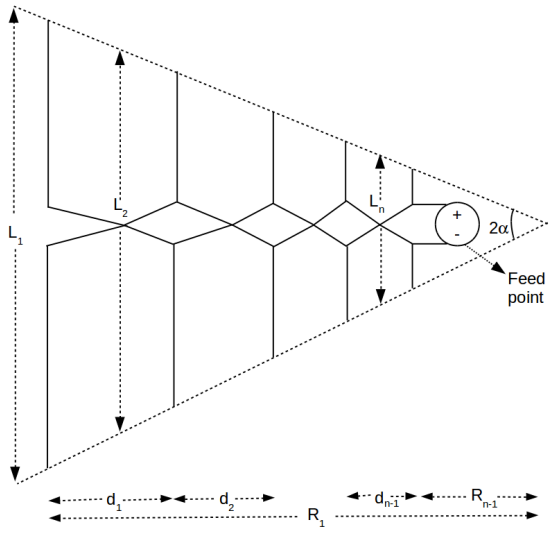

Figure 2.1: Schematic of a log periodic dipole antenna (not to scale).

Another important design parameter is the spacing factor σ. It depends upon the half apex angle α which decides the operating bandwidth of LPDA. The spacing factor, the geometric constant and the half apex angle are related to each other through equation 2.2, i.e.

$$\sigma = \frac{1-\tau}{4\tan\alpha} \tag{2.2}$$

The geometrical relationship between the dipole arms of the antenna, half apex angle and inter-element spacing is shown in Figure 2.2. **I** used the optimum design curve of a LPDA given by Carrel (1961). This curve gives a set of values of design parameters τ ans σ for the directional gain (G) between 6.0 dBi[3] to 10.5 dBi of a LPDA. Total number of dipoles which should cover the operational bandwidth is determined using:

[3]Antenna gain (in Decibles) with respect to an isotropic antenna.

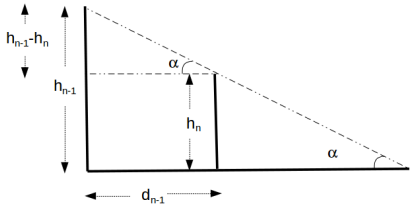

Figure 2.2: Geometrical relation between LPDA dipole arms and inter-dipole spacing.

$$N = \frac{ln(\beta)}{ln(1/\tau)} \tag{2.3}$$

where β is called the bandwidth ratio ($= \frac{f_n}{f_1}$), and tau is the design constant.

Table 2.1: Design parameter values for LPDA (15 – 85 MHz)

S. No.	distance from top (cm)	Inter-element spacing (cm)	Dipole length (cm)	Frequency (MHz)
1.	0.0	0.0	77.6	96.7
2.	18.7	18.7	93.5	80.2
3.	41.2	22.5	112.6	66.6
4.	68.4	27.1	135.7	55.3
5.	101.0	32.7	163.5	45.9
6.	140.4	39.4	197.0	38.1
7.	187.9	47.5	237.3	31.6
8.	245.1	57.2	285.9	26.2
9.	314.0	68.9	344.5	21.8
10.	397.0	83.0	415.0	18.1
11.	497.0	100.0	500.0	15.0

Owing to long wavelengths that we intend to operate, it may not be possible to physically steer the antenna to track the Sun. Thus, we have to 'tune' the directivity of the antenna such that the celestial object of interest is in the field of view (FOV) for at least 5-6 hours. So, we selected a moderate gain ≈ 6 dBi. From the Carrel's design curve, we chose τ and σ values as 0.83 and 0.05, respectively. This led to a total number of dipole elements of the antenna to be 11. Table 2.1 contains the design parameters of the antenna.

Figure 2.3: The 15 - 85 MHz LPDA (foreground) in the field. This longest dipole arm of this antenna is 500 cm. The height of the antenna is 5.2 m.

2.2.1.2 Measurements of Antenna parameters

After the fabrication of LPDA, its Voltage standing wave ratio (VSWR[4]; a measure of impedance) is measured using RF analyzer. The VSWR (Figure 2.4) values are ≤ 3 throughout the bandwidth expect at 35 MHz, which indicates that the total power transfer from the antenna to the load is $\approx 69\%$. **The VSWR is ≥ 2 at few frequencies because of the supporting structures used to avoid the sagging of the dipole arms of the antenna.** The beam width of this antenna in the two primary planes, i.e. E-plane and H-plane were 80° and 120°, respectively. This gives rise to a total collecting area $0.3\lambda^2$ for the antenna. The various parameters of this antenna are mentioned in Table 2.2. Antenna shown in Figure 2.3 is the front-end of the observing set-up..

Table 2.2: Design characteristics of 15 - 85 MHz LPDA

Frequency Range	15-85 MHz
No. of dipoles	11
Design Constant (τ)	0.83
Spacing Constant (σ)	0.05
VSWR	$\leq$3
$HPBW_E$	$\approx 80°$
$HPBW_H$	$\approx 120°$
Collecting Area (A_e)	$\approx 0.3\lambda^2$
Gain (G)	$\approx$ 6 dBi
Front-to-back ratio	$\approx$ 30 dB
Front-to-side ratio	$\approx$ 28 dB

Since our aim is to record the polarization state of the radio signal received from

[4]VSWR is a function of the reflection coefficient, quantity that describes the power reflected from a radio-frequency (RF) device under test.

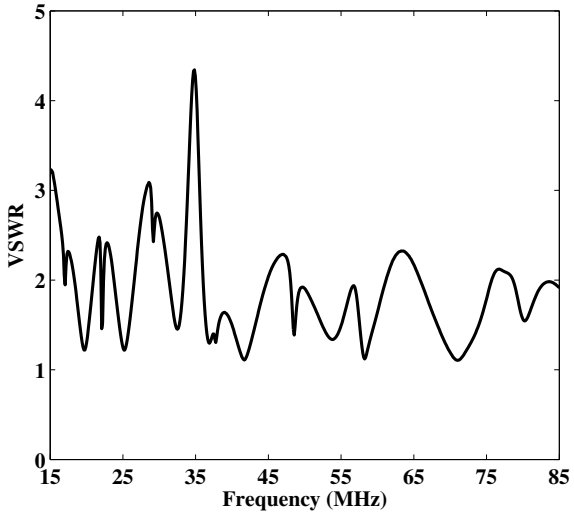

Figure 2.4: VSWR of the antenna in the 15 - 85 MHz band. The values are ≤ 3, except at 35 MHz.

the Sun, two identical antennas were fabricated and installed orthogonal to each other. The technical reason for the latter is discussed in section 2.3.3.2. The signal received by the antennas are filtered to remove unwanted frequency components and then are amplified to increase the signal strength for further processing.

2.2.2 Characteristics of Filters and Amplifiers

The transmission / reception characteristic of any RF device is described using the scattering parameters (S-parameters) as it is convenient at high frequencies (Pozar, 2009). For a two port network, S11 and S22 are input and output reflection coefficient, respectively, and S21 and S12 are forward transmission (or gain (in case of active devices) or loss (in case of passive devices)) and reverse transmission (isolation, in case of active devices), respectively.

2.2.2.1 Filters

The signals from field were brought to the lab through a chain of analog components and RF cables. Though the antenna was designed to operate in the 15 - 85 MHz band, the low frequency radio noise were also easily picked up due to their higher power level as compared to that of the band of interest. Therefore, signal below 15 MHz were rejected using a high-pass filter (HPF) with cut-off 15 MHz (Figure 2.5a). To reject the FM band, a low-pass filter with cut-off 85 MHz (Figure 2.5b) was used. These filters were custom made at the observatory and were of five stage constant k LC circuit[5]. **The insertion loss of the filter was ~ 0.2 dB.**

[5] http://www.ti.com/lit/an/slaa701a/slaa701a.pdf

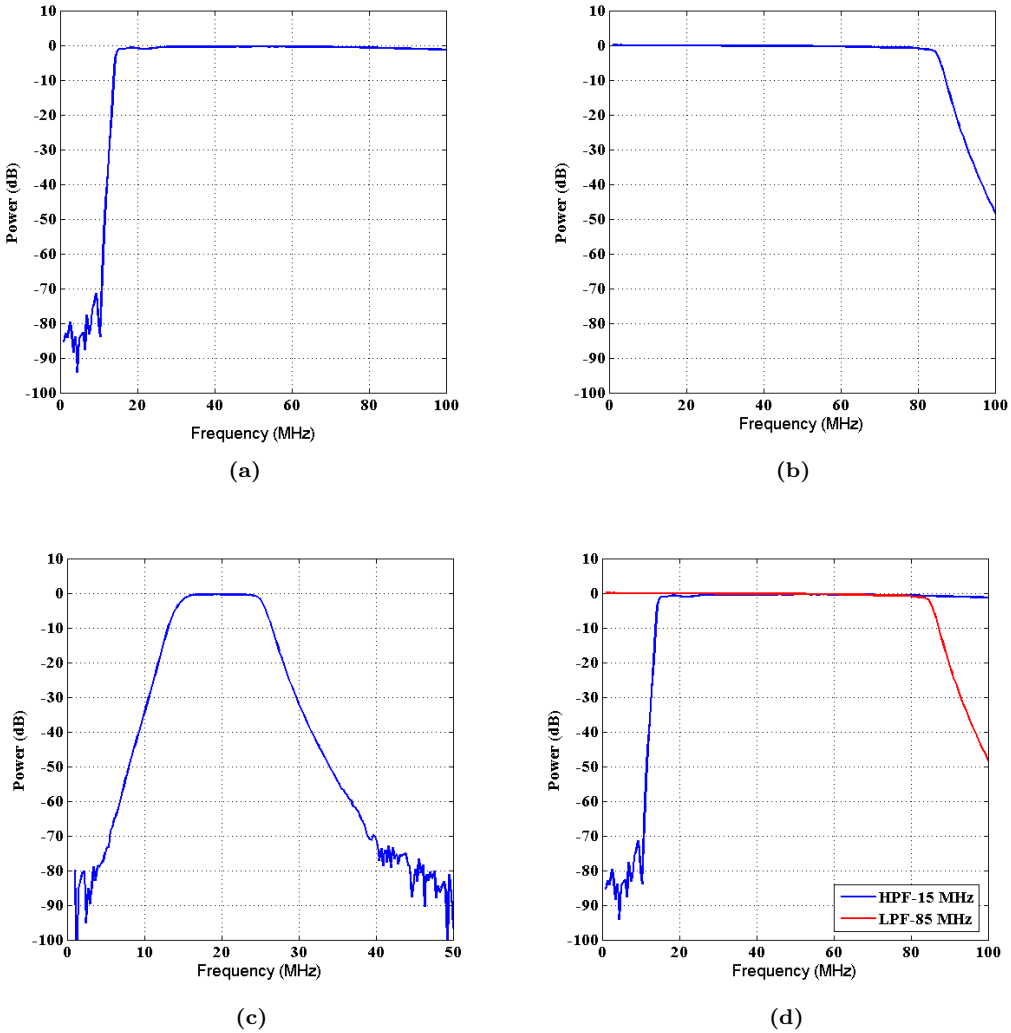

Figure 2.5: The filter passband characteristics: (a) HPF (f_c = 15 MHz); (b) LPF (f_c = 85 MHz); (c) BPF (f_{c1} = 15 MHz f_{c2} = 25 MHz); (d) BPF (f_{c1} = 25 MHz f_{c2} = 85 MHz).

The power spectrum of the radio signal from the background sky decreases rapidly from 15 to 85 MHz (Figure 2.7). The signal strength reaches almost to the noise floor of the spectrograph after $\sim$ 45 MHz in both LPDA oriented East-West (EW) and North-South (NS) directions. This is mainly because the sky brightness temperature decreases almost exponentially with frequency[6]. Hence, the observational band was divided into two subbands using two band-pass filters (BPF): (1) 15 - 25 MHz and (2) 25 - 85 MHz. The transmission characteristics (S21) of different filters designed are shown in Figure 2.5.

[6] https://www.cv.nrao.edu/~demerson/radiosky/rsky_p3.htm

2.2.2.2 Amplifiers

Amplifiers are used to enhance the signal received by the antenna. In radio astronomy, as the received signal has very low power content, a low noise amplifier (LNA) is used as a first stage amplifier. A LNA amplifies the signal without significantly degrading its signal-to-noise ratio (SNR). SNR is a measure of signal strength relative to background noise. SNR is one of the most significant measures of performance of any system. We used a $\approx$ 32 dB[7] gain amplifier to enhance the power of RF signals. Figure 2.6 shows the gain plot (S12) for Minicircuits MAN-1LN amplifier[8] as a function the frequency.

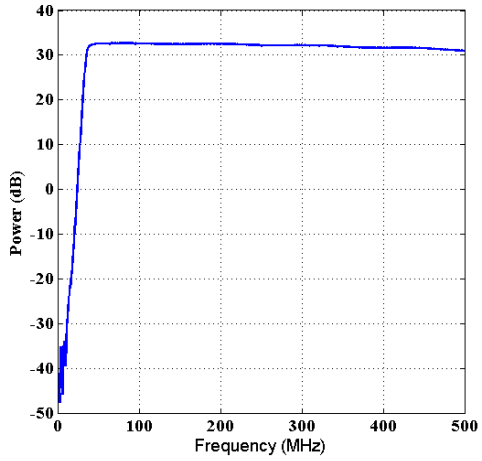

Figure 2.6: Frequency response of MAN-1LN amplifier. It has a gain of $\approx$ 32 dB.

2.2.3 Spectro-polarimeter Signal Chain

The signals received with the two antennas oriented in EW and NS directions in the field are passed through 15 MHz HPF and 85 MHz LPF, to filter out the 15 - 85 MHz band. Then the signal is amplified using a $\approx$ 32 dB (ref Section 2.2.2.2) LNA and brought to the lab using a low loss coaxial cables. The signal received by the two antennas are shown in Figure 2.7. They are then split into two subbands i.e 15 - 25 MHz and 25 - 85 MHz using aforementioned filters and fed to a digital receiver. The power spectrum of the two subbands are shown in Figure 2.8. Figure 2.9 shows analog frontend modules of the system.

[7] The decibel (dB) is a logarithmic unit used to measure power level. It is normally the ratio input to output RF power or voltage levels.

[8] https://ww3.minicircuits.com/pdfs/MAN-1LN.pdf

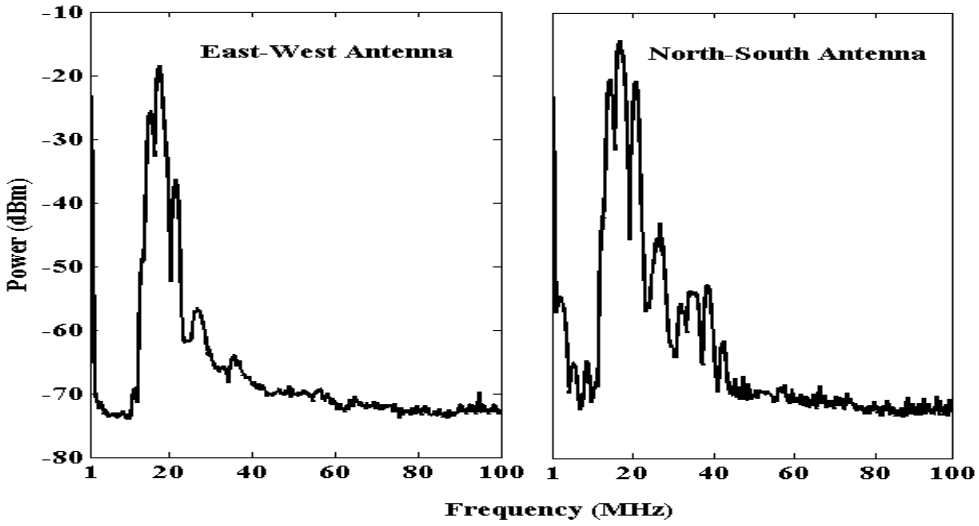

Figure 2.7: The power spectrum of the signal received with the LPDA before dividing the signal into two subbands. The power level at frequencies greater than 40 MHz are almost close to the noise floor.

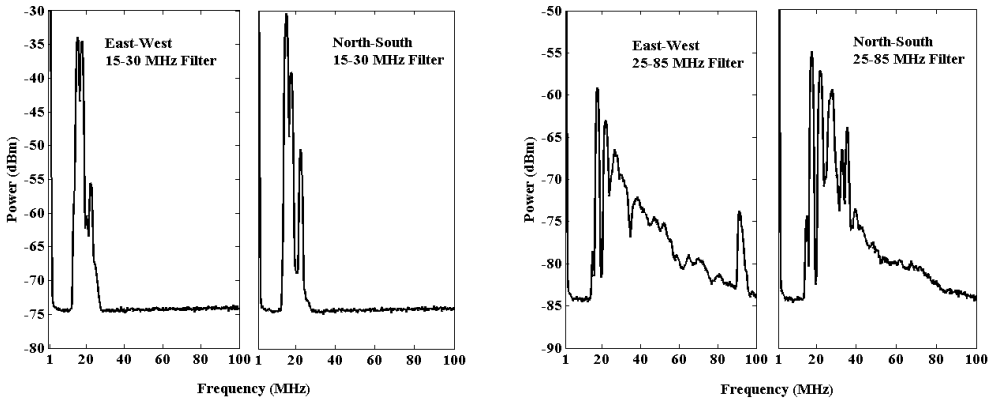

(a) (b)

Figure 2.8: The power level of the signal received with the LPDA after dividing into two subbands using two filters: (a) lower band (15 – 25 MHz). (b) upper band (25 – 85 MHz).

2.3 Digital Backend Design

The main components of Digital Spectrometer are the high speed Analog to Digital Converter (ADC) and a Field Programmable gate Array (FPGA). The FPGA of the spectro-polarimeter is developed using the Reconfigurable Open-Architecture Computer Hardware (ROACH-I) board from the CASPER[9] community. The function of the digital receiver is to digitize the band-limited analog signal and estimate

[9] https://casper.ssl.berkeley.edu/wiki/Main_Page

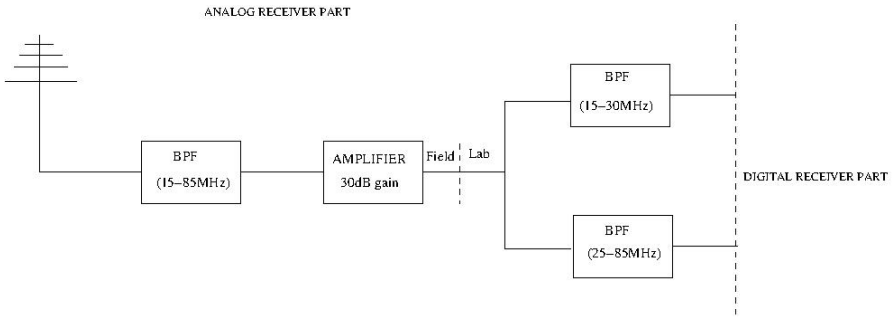

Figure 2.9: The schematic of analog receiver modules of the EW / NS antenna system of the 15 - 85 MHz spectro-polarimeter.

the Stokes parameters from them, and transfer the processed spectra to a data acquisition server. Figure 2.10 shows the steps involved in digitizing and recording the spectra.

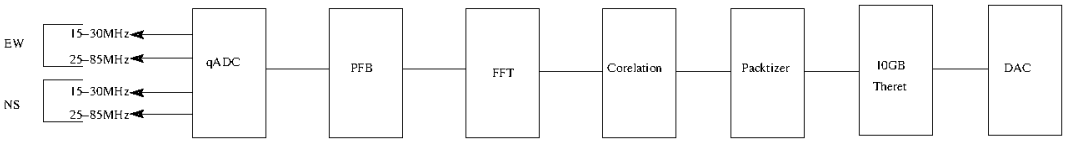

Figure 2.10: The block diagram of signal processing using the ROACH board.

2.3.1 ROACH Board

The centre of ROACH is a Xilinx Virtex 5 FPGA (SX95T designed for DSP-slice-intensive applications). A separate PowerPC runs Linux and is used to control the board for programming the FPGA and for allowing interface between the FPGA and external devices using Ethernet. There are two SRAMs dedicated for high-speed, medium-capacity memory and two DDR2 DIMMs dedicated for slower-speed, high-capacity memory. Z-DOK connectors are used to interface ADC, DAC and other modules with the FPGA. Four CX4 connectors provide a total of 40Gbits/sec bandwidth for connecting ROACH boards together, or connecting them to other XAUI/10GbE-capable devices. Figure 2.11 shows the ROACH board with various modules marked. Figure 2.12 shows the architecture of ROACH board.

2.3.2 ADC Characterization

Before putting any module into use, it is advisable to characterize it to understand its functional behavior thoroughly. The next subsection deals with the characterization of the Analog to Digital Converter (ADC).

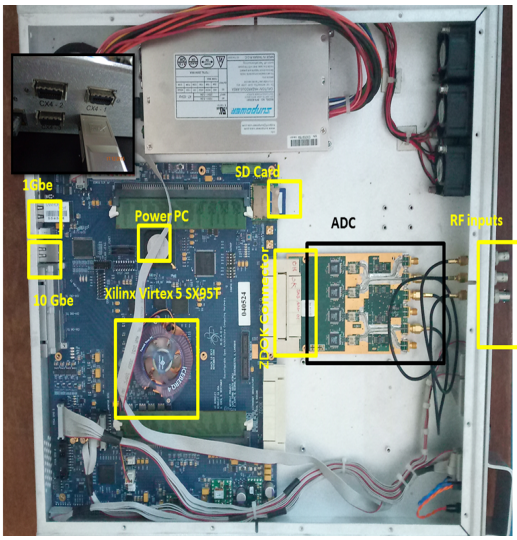

Figure 2.11: Photograph of the ROACH board with various modules marked.

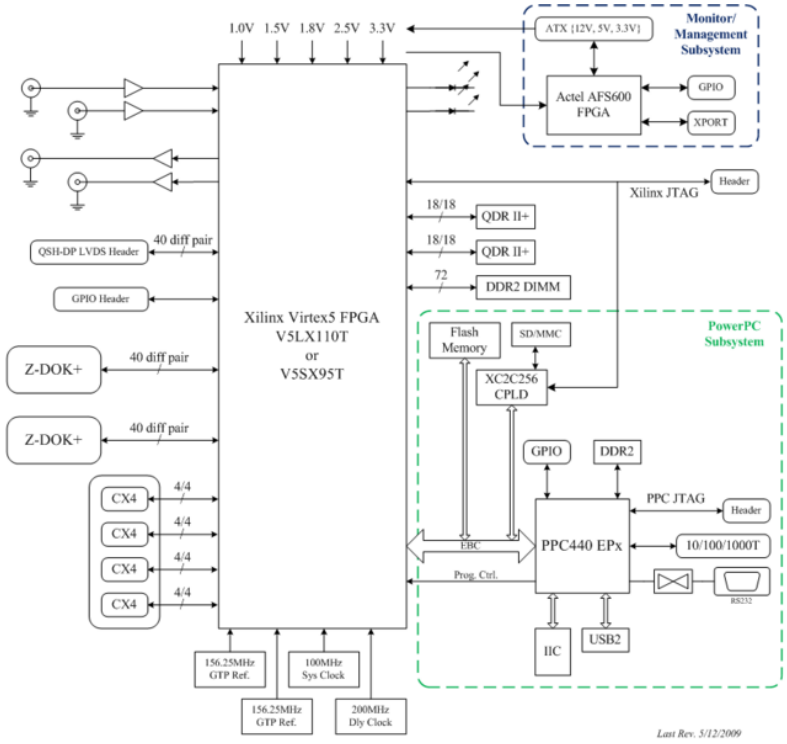

Figure 2.12: Block diagram of the ROACH board (courtesy: Henry Chen).

2.3.2.1 Linear Range of the ADC

The digital receiver digitizes the RF signal and helps to determine the Stokes parameters. The first stage of the digital receiver is a quad Analog to Digital converter (qADC)[10]. The qADC has four AD9480 ADCs[11] from analog devices.

[10] https://casper.ssl.berkeley.edu/wiki/ADC4x250-8
[11] https://www.analog.com/media/en/technical-documentation/data-sheets/AD9480.pdf

The AD9480 is an 8-bit, monolithic ADC that has a low power consumption and high speed. AD9480 works at 250 MSPS with a reference voltage of 3.3 V. The full-scale voltage of this ADC is 1.0 V. The linear range of operation of the ADC was determined using lab test. For that, the level of input power was varied from 0 dBm to -65 dBm as a function of frequency and the linearity of the ADC was tested. Figure 2.13 shows the test result obtained at 50 MHz. Table 2.3 has the linear range details of the ADC at **a few** other test frequencies. The reference count for output counts were taken as 1 mV (refer table 2.3.

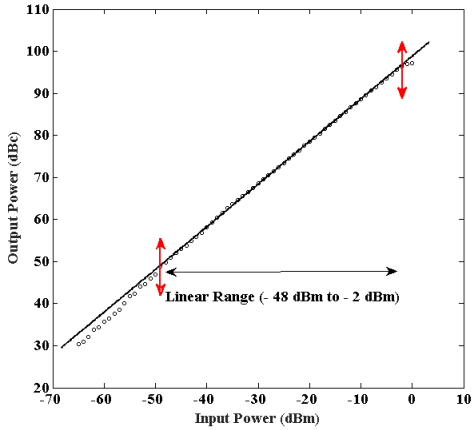

Figure 2.13: Result of the linear range test of the ADC at 50 MHz. Red arrows show the linear range of operation.

Table 2.3: Linearity test results of the ADC at 50 MHz

Frequency (MHz)	Input (dBm)			Output counts (dB)			Linearity (dBm)	
							max	min
30	0	-32	-65	96	67	30	-3	-49
50	0	-32	-65	92	64	29	-2	-48
70	0	-32	-65	90	63	28	-2	-48

2.3.2.2 Signal to Noise Ratio (SNR) of the ADC

Signal to noise ratio, S/N or SNR is an important parameter to define the performance of any analog or digital system. It describes the strength of the signal to the noise present in the system. It is normally expressed in terms of dB. SNR is given as,

$$\frac{S}{N} = 20 \times log_{10}\frac{V_s}{V_n} = 10 \times log_{10}\frac{P_s}{P_{rms}} \tag{2.4}$$

The dynamic range of any ADC is the range between the minimum detectable signal to the maximum signal (just below saturation limit). The higher dynamic

range allows us to detect the weak bursts in the presence of strong bursts. For characterizing the dynamic performance of this ADC, spurious free dynamic range (SFDR) was calculated. To estimate the SNR and SFDR of this ADC, the input power levels were varied from -2 dBm to -48 dBm (linear range of the ADC) at 50 MHz, and the output counts were Fourier transformed offline. Figure 2.14 shows decrease in SNR when the input power at 50 MHz was decreased. Since the maximum signal decreases, the decrease in SNR is expected. Table 2.4 lists the above three parameters with respect to different input powers at 50 MHz.

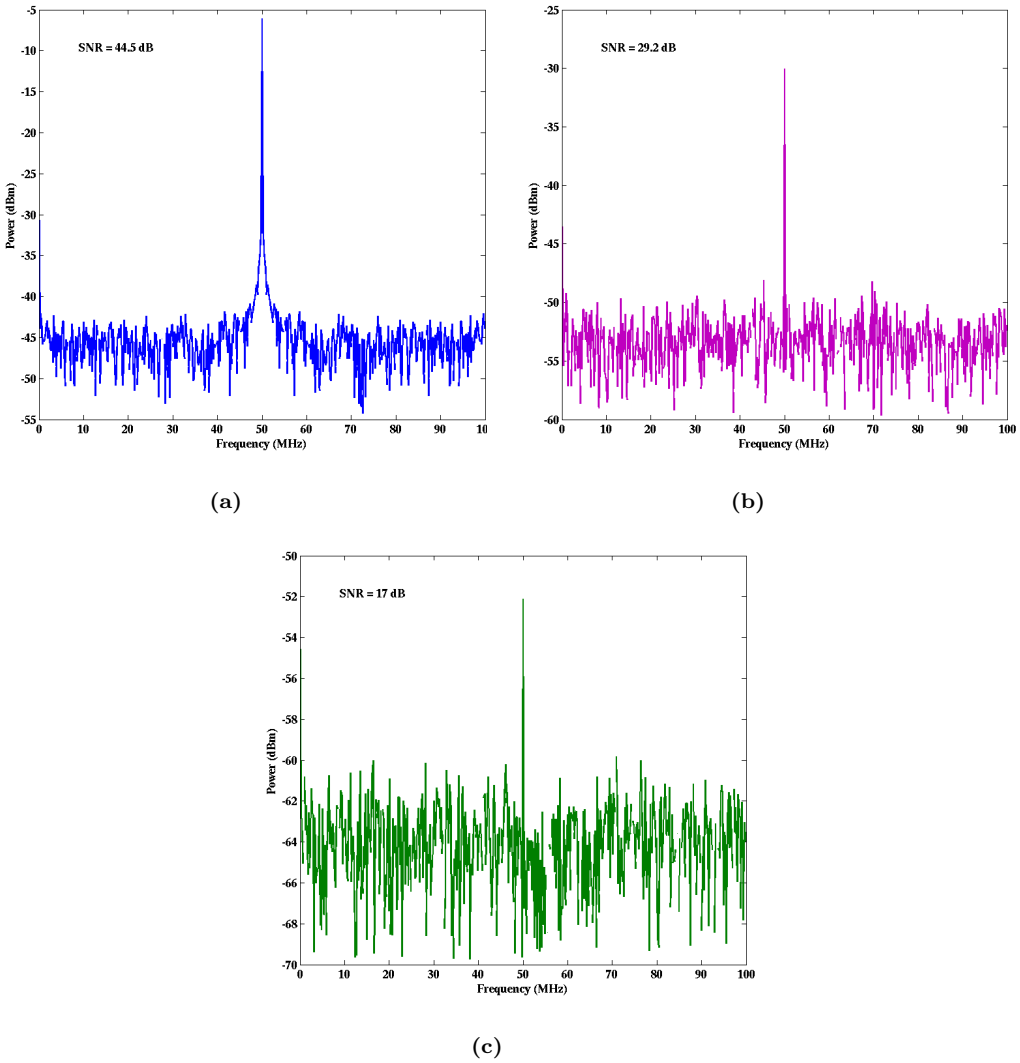

Figure 2.14: The Fourier transform of the input stream at 50 MHz with different power levels, i.e -2, -26, -48 dBm. Table 2.4 contains the DR, SNR and SFDR for these plots.

Table 2.4: SNR, DR and SFDR values of the ADC vs input power

Input Power (dBm)	SNR (dB)	DR (dB)	SFDR (dB)
-2	44.5	42	38.5
-26	29.2	24	21
-48	17	13	10

2.3.3 The Spectro-polarimeter implementation on ROACH

2.3.3.1 The Fourier Transform

The qADC used in the setup works at a common maximum sampling rate of 250 MHz. This means that the maximum bandwidth that can be sampled is 125 MHz (Nyquist Sampling). Since our bandwidth of interest is 15 - 85 MHz, a sampling frequency of 200 MHz is used to sample a baseband of 100 MHz. Figure 2.8 suggests that the power received from the Sun during quiet phase is within $\approx$ 25 dB in our frequency band of interest. And during the active phase the signal strength (i.e. power) is expected to increase by an order or two. Hence a DR of 45 dB (as per the test results mentioned in Table 2.4) is sufficient to accommodate the enhanced signal strength during any activity (Nelson, Sheridan, and Suzuki, 1985; Mugundhan *et al.*, 2018). The ADC is connected to the ROACH with ZDOk connector. The clock signal (sync) is also simultaneously transmitted from one stage to another to have a synchronized operation. CASPER's MATLAB-Simulink System Generator Embedded Development Kit (MSSGE) is used for developing the firmware for the spectro-polarimeter. The ADC signal is digitized to 8.7 bit precision (signed). The digitized fixed number is passed through a 4-tap polyphase filter bank (PFB), (Vaidyanathan, 1990; Klein *et al.*, 2006; Price, 2016).

In PFB, the input signal is decomposed into number of signals (in this case, four parts)[12]. PFB is combination of finite impulse response (FIR) filters, and can be understood as input sequence that has been decomposed into a set of different phased outputs. PFB is used to reduce the spectral leakage from the desired frequency channel into adjacent channels as shown in Figure 2.15. Normally, the Fast Fourier Transform (FFT) has a spectral isolation of $\approx$ 13 dB (Price, 2016). By using a PFB, this isolation is increased up to $\approx$ 60 dB (Price, 2016). A 1024 point FFT is taken, for which there are 512 number of bins. This provides a spectral resolution of $\approx$ 100 kHz. The high frequency resolution helps to record narrow band or fine structures in the radio emission from the Sun. For FFT, fft-biplex-real block from CASPER-Simulink is used to only calculate the real frequency bins. The real and imaginary components of the FFT are separated and re-quantized to signed 8.7 bits, in order to avoid the polarization leakage. Polarization leakage is a measure of received power corresponding to one sense of polarization (for ex.

[12] https://casper.ssl.berkeley.edu/wiki/The_Polyphase_Filter_Bank_Technique

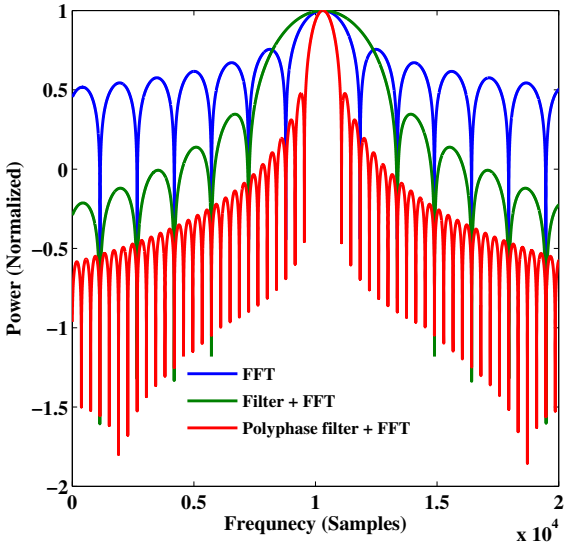

Figure 2.15: Fourier responses of a signal with FFT, windowed-FFT and FFT with a PFB. The PFB reduces the spectral leakage in adjacent channels as seen with the red color profile.

vertical) by an antenna when it is exposed to radiation of orthogonal polarization (i.e. horizontal). In order to achieve the best performance, the leakage of an antenna should be reduced to the lowest possible value. Ideally, it is expected to have no signal in the real cross-correlation channel. Any deflection in this channel is the leakage from the imaginary cross-correlation component that is Stokes-V. Estimation of the leakage helps to estimate the correct value of degree of circular polarization.

2.3.3.2 Estimation of Stokes Parameters

From the above discussions, it is clear that spectro-polarimeter is an FX (Fourier transform - Multiplication) type system. It is well known that the Stokes parameters are used to represent the behaviour of the polarized light, and in matrix form, they can be written as (Collett, 1992):

$$\begin{bmatrix} I \\ Q \\ U \\ V \end{bmatrix} = \begin{bmatrix} < E_x^2 > + < E_y^2 > \\ < E_x^2 > - < E_y^2 > \\ < E_x E_y^* > + < E_x^* E_y > \\ i(< E_x E_y* > - < E_x^* E_y >) \end{bmatrix} \tag{2.5}$$

Here, E_x and E_y are the RF power received from two different antennas (one in EW direction and the another in NS direction as mentioned earlier). From the above matrix expression, the signals received by the two orthogonal antennas can be used to extract Stoke-I and Stokes-V components of the EM signal. The sum of the auto-correlation of both signal gives Stokes-I intensity and the imaginary part

of difference in cross-correlation of the two signals gives Stokes-V intensity (Collett, 1992):

$$I =< E_x E_x^* > + < E_y E_y^* > \tag{2.6}$$

$$V = i(< E_x E_y^* > - < E_y E_x^* >) \tag{2.7}$$

At meter wavelengths, the Faraday rotation is high that it wipes out any linearly polarized component. Therefore, the observer can only receive the circular polarized emission from the Sun (Ramesh, Kathiravan, and Narayanan, 2011). Hence this system is designed to detect only the circular polarized emission.

2.3.4 Data Acquisition system

2.3.4.1 Accumulator

A vector accumulator is used to store the correlations as a function of frequency. There are two accumulators for storing the auto-correlation values of individual antenna signals, and two accumulators for storing the real and imaginary components of the cross-correlation values of the signals. The vector length is 1024 for the accumulators, with the data being 32 bit wide. The vector length is the size of the FFT bins. The data is accumulated for every 100 ms (the temporal resolution of the system).

2.3.4.2 Packetizer

The 10 Gbe is used to transfer the spectral output from ROACH to data acquisition system (DAS). The maximum capacity of a 10 Gbe is only nine kB. Since the width of each spectra is 32 kb, we need to packetize the sepctra before transmission. This is done by using two first-in-first-out (FIFO) to record the accumulated spectra from each vector accumulator. The length of the FIFO is 1024. The data from the FIFOs are read sequentially out. The output of the two vector accumulators is concatenated into 64 bit width and written at the same time into the two FIFOs in the packetizer while the write enable is on. Once done, the spectra from first FIFO are read using 10 Gbe, and after certain clock delay, the spectra is read from the second FIFO. Proper delays are provided to avoid overflow during transmission.

2.3.4.3 10 Gb Ethernet

The 10 Gbe is a group of computer networking technologies for transmitting Ethernet frames at a rate of 10 gigabits per second[13]. The packetized data (frames) are sent using User Data Protocol (UDP). The 10 Gbe uses 64 bit wide data with 1024 size. The data stream is wrapped in a UDP frame for transmission. Since

[13] https://casper.ssl.berkeley.edu/wiki/Tutorial˙10GbE

each frame consists of 2048 bytes, two packets are sent for every clock cycle. Each packet is written into the buffer inside the 10 Gbe block and when the transmission signal is high, a frame is transmitted to the DAS. The data is acquired using python - a shell script written to compile and run the code for acquiring data.

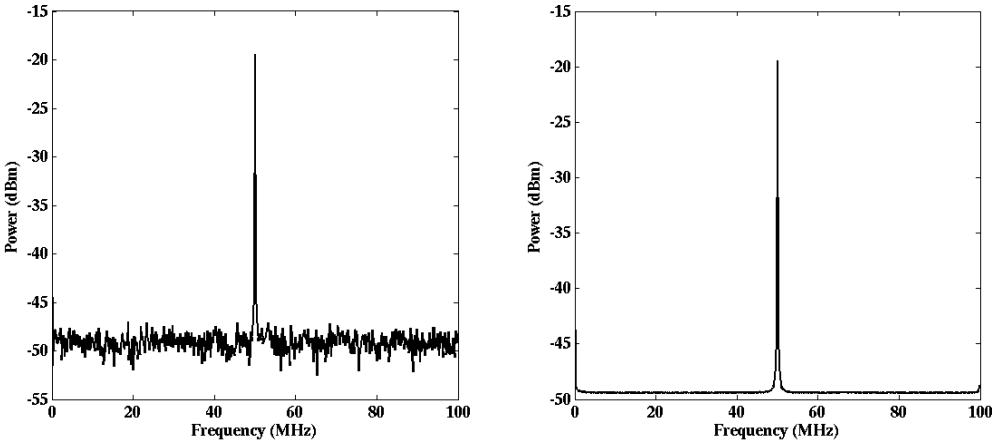

(a) (b)

Figure 2.16: Left panel: The spectra at 50 MHz with no spectra averaged on board; Right panel: The same but averaged for 20480 samples. This has improved the SNR by $\sqrt{20480}$ times.

2.3.5 SNR of the Digital System

After the digital system was designed, the SNR of it was calculated. The sampling clock of the ADC used is 200 MHz, which means that the system works at 5 ns rate. On-board, 20480 spectra are averaged to get a temporal resolution of 100 ms. Ideally the SNR should increase by $\sqrt{N}$ times, where N is the number of spectra averaged on board. The estimated SNR is 3.5 dB (expected 4.9 dB). Figure 2.16 shows one spectrum (left panel) whose rms noise fluctuation is higher ($\approx 10^{-5}$ order) as compared to that of the averaged spectrum (right panel) whose rms noise fluctuation is of the order of order $\approx 10^{-6}$. Both spectra correspond to 50 MHz input signal. The SNR in the left and right panel are $\approx$ 27.5 dB and $\approx$ 31 dB, respectively. In linear scale, the improvement in SNR is expected to be $\approx$ 143 times. The test results showed the rms noise in single spectrum and averaged spectrum are $\approx 5.47 \times 10^{-5}$ and $\approx 1.73 \times 10^{-6}$, respectively. This implies an improved SNR $\approx$ 31 times. In dB scale, the improved SNR is $\approx$ **14.5 dB.**

2.4 System Calibration & Observations

2.4.1 Galactic background observations

To check the system's performance, the Galactic background was observed between $15-85$ MHz. The centre of our Galaxy is Sagittarius A (Sgr A), which is a complex

radio source, consisting of the supernova remnant Sagittarius A East, the spiral structure Sagittarius A West, and a bright compact radio source at the center of the spiral structure, called Sagittarius A*. The Sgr A has a right ascension (RA) of 17:45:00 and declination of -29^o. The local transit time of Sgr A is 17:46:13 LST. Since radio emission from the Galactic background is unpolarized, the deflection in Stokes-V channel would attribute to the leakage or instrumental polarization. Figure 2.17 shows the light curve (in Stokes-I and V channels) of the galactic background at 50 MHz obtained with the new instrument during its meridian transit. In Stokes-I channel the maximum emission is seen at 18:00 LST which indicates that Galactic background transited over the antenna at that point of time. The deflection in Stokes-I and Stokes-V channels are $\approx 1.35 \times 10^{-5}$ mW and $\approx 1.56 \times 10^{-6}$ mW, respectively implies that instrumental polarization of $\leq 4\%$.

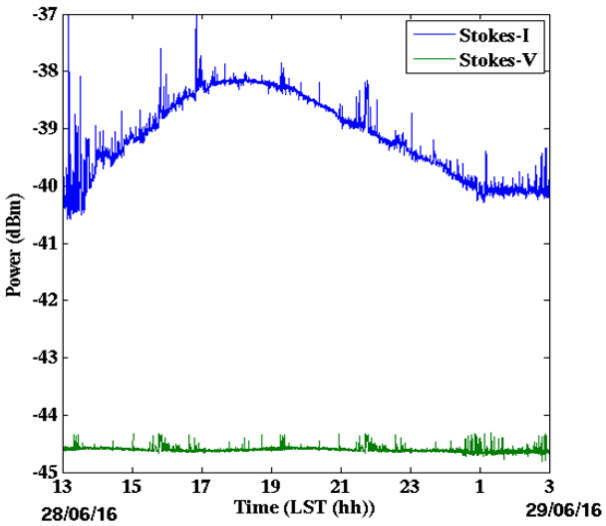

Figure 2.17: The first light observations made at 50 MHz with the newly designed spectrograph when the Galactic background transited over the antenna at Gauribidanur observatory. The 'blue' and 'green' color represent Stokes-I and Stokes-V profiles, respectively.

2.4.2 Observations of Type III radio bursts obtained with the new spectrograph

On July 23, 2016 the instrument observed a type III burst at $\approx$ 05:27 UT. Figure 2.18 shows the comparison of the dynamic spectra obtained and the one obtained with the new ROACH based system and the one obtained with the existing spectrum analyzer based instrument. Since the resolution (10 and 3 times lesser in frequency and time, respectively) is lower in the old / existing set-up, the fine structures can not be seen with that.

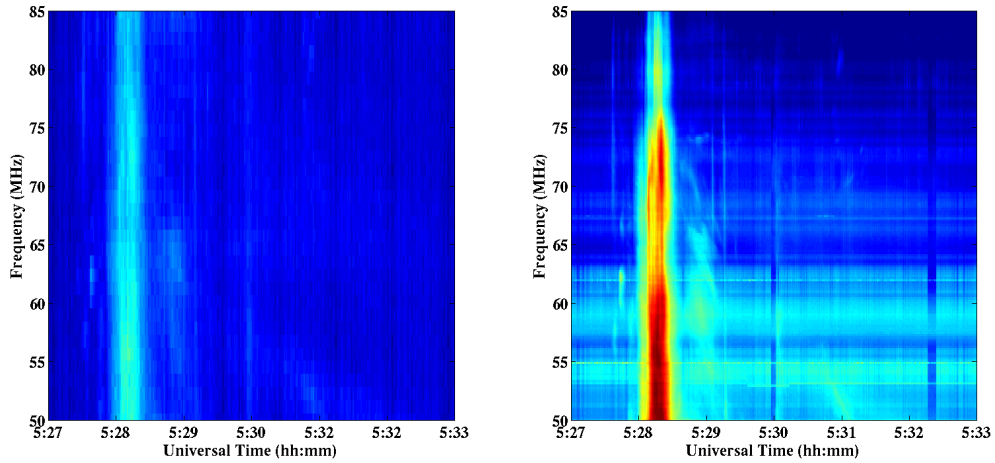

(a) (b)

Figure 2.18: Left panel: A type III burst observed with Spectrum analyzer based backend at 05:27 UT; Right Panel: The same type III burst observed with ROACH based backend.

2.4.3 Comparison of the new system with the existing one

2.4.3.1 SNR improvement

Since one of the aims of building a new instrument is to improve the SNR of the existing instruments and thereby recording the radio bursts with better contrast, we compared the SNR of the new instrument with the existing one. Figure 2.19 shows the power profile of the type III burst at 80 MHz. The unit of power is in mW. The noise fluctuations in the new instrument is about an order less than the old one, hence the SNR was improved by ≈ 10 times as compared to the expected theoretical improvement of ≈ 11.2. Table 2.5 lists the peak and noise level of the signal for the two systems.

Table 2.5: SNR comparison of the system

	SA	ROACH
Signal Peak (mW)	0.047	0.040
rms Noise (in mW)	3.1e-4	2.9e-5

2.4.3.2 Detection of weak radio bursts

The second aim of this new instrument is to detect weak bursts in the presence of strong bursts. Statistically the solar bursts have magnitude of an order or two higher than the quiet Sun emission, which implies that high dynamic range is required for the system to detect weak and strong bursts together. To compare both instruments, the spectral and temporal resolutions were made similar, i.e, the data from both systems are averaged for 1 MHz and are integrated for 1 sec. The

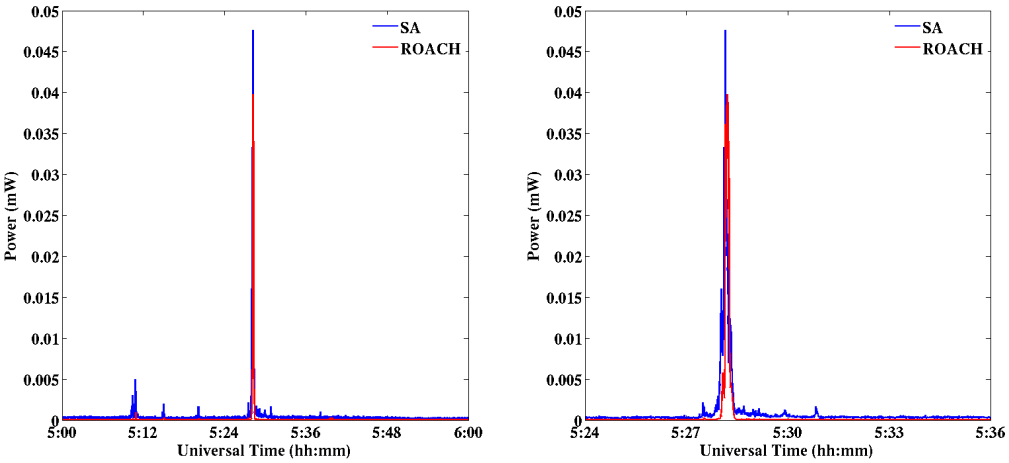

(a) (b)

Figure 2.19: Left panel: Light curve of the type III burst at 80 MHz; Right Panel: same type III zoomed in to show the fine structures. 'Blue' and 'red' color represent the old and new system, respectively. The significant improvement in SNR is due to the reduced noise fluctuations in latter.

temporal profile at 60 MHz is shown in Figure 2.20. The weak feature at 5:10 UT is not present in SA data. The signal strength is much higher than the noise fluctuations.

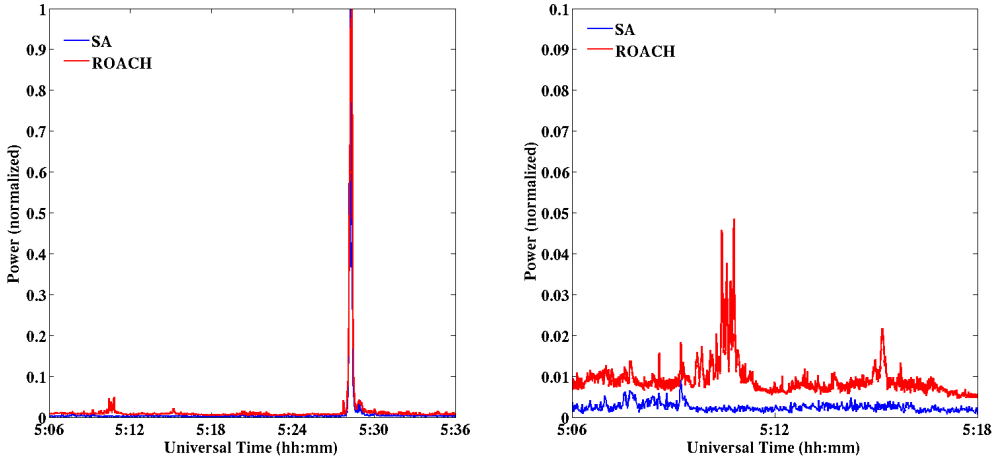

(a) (b)

Figure 2.20: Left panel: The time (1 sec) and frequency (1 MHz) averaged profile of type III burst at 60 MHz; Right Panel: A weak burst detected at 5:10 UT by ROACH based system whereas it is not detected by SA based system.

2.5 Spectro-polarimeter: Conclusions

I have designed a new spectro-polarimeter with a spectral and temporal resolution of 100 kHz and 100 ms, respectively. **I have characterized** the antenna frontend, analog chain and digital backend. Trial observations of the galactic background as well as the Sun are carried out. The new system is compared with the existing analog spectrum analyzer based one, and the SNR of the former is better by 10 times. Also, the new system is able to detect **a few** weak bursts whereas the old system is not able to (Kumari *et al.*, 2019b; Barve *et al.*, 2019). The following section exemplifies the Science that can be done using the Type-II burst data obtained with the new spectro-polarimeter.

2.6 Type II burst Observed with new ROACH based Spectro-polarimeter

2.6.1 Introduction

The various techniques that are currently employed to determine the coronal magnetic field are based on band-splitting in type II bursts, second harmonic plasma emission in type II, type III, and type IV bursts, gyrosynchrotron emission in type IV bursts, Alfv́en speed in type II bursts, quasi-periodicity in type III bursts, etc. Note that while the mechanism is either fundamental and/or second harmonic plasma emission in the case of type II and type III bursts, it is either second harmonic plasma or gyrosynchrotron emission in the case of type IV bursts. We would like to point out here that the characteristics of the polarization of fundamental plasma emission from solar radio bursts are yet to be established. So, estimates of B are currently possible only using second harmonic plasma emission from the bursts. The estimates are from observations of either the total intensity, i.e. Stokes-I alone (Smerd, Sheridan, and Stewart, 1975; Gopalswamy and Kundu, 1990; Bastian *et al.*, 2001; Vršnak *et al.*, 2002; Mancuso *et al.*, 2003; Ramesh *et al.*, 2003; 2004; 2013; Cho *et al.*, 2007; Kishore *et al.*, 2016) or from both the total and circularly polarized intensities, i.e. Stokes-I and Stokes-V (Dulk and Suzuki, 1980; Gary *et al.*, 1985; Ramesh *et al.*, 2010a; Ramesh, Kathiravan, and Narayanan, 2011; Tun and Vourlidas, 2013; Sasikumar Raja and Ramesh, 2013; 2014; Hariharan *et al.*, 2014; 2016; Kumari *et al.*, 2017b). Note that we have mentioned only Stokes-I and Stokes-V emission here since Faraday rotation of the plane of polarization in the solar corona and Earth's ionosphere makes it impossible to observe the linear polarization (represented by Stokes-Q and Stokes-U) within the typical observing bandwidths of $\approx$100 kHz (refer for example Grognard and McLean, 1973.) It has been shown that thermal radio emission observed from the solar corona at low frequencies can also be used to estimate B (Ramesh, Kathiravan, and Sastry,

2003; Sastry, 2009; Ramesh, Kathiravan, and Sastry, 2010).

Gopalswamy *et al.* (2012) reported a new technique, based on the geometrical properties of the flux rope structure of a white-light CME and the associated shock speed, to estimate B. Similarly, Kwon *et al.* (2013b; 2013a) reported estimates of B from measurements of the propagation speed of a fast magnetosonic wave associated with a CME. Reports of a comparison between the B values obtained independently in radio and optical wavelengths for the same event using simultaneous observations that do not assume any model for $N(r)$ are rare, however comparison is important to validate the different techniques for estimating B. Considering this, the simultaneous observations of a white-light CME near the Sun with flux rope structure and band-splitting exhibited by the associated type II burst are used to estimate the magnetic field strength in the middle corona. The following subsections describe observations, analysis and results.

2.6.2 Observations

2.6.2.1 Radio Observations

The radio data was obtained with the new spectro-polarimeter (called as Gauribidanur RAdio SpectroPolarimeter; abbreviated as GRASP) described in the previous section. Figure 2.21 shows the dynamic spectrum of the transient emission from the Sun observed with the GRASP on 23 July 2016. The fast-drifting feature (from high to low frequencies) seen at ≈05:30 UT is a type V burst. The slow-drifting feature seen between ≈05:30 – 05:32 UT is a type II burst. While the type II burst is confined to a narrow range of frequencies (start frequency ≈28 MHz; end frequency ≈24 MHz), the type V burst extends beyond this. We verified these frequency limits with observations of the *Gauribidanur LOw-frequency Solar Spectrograph* (GLOSS; Ebenezer *et al.*, 2001; 2007; Kishore *et al.*, 2015) and the e-CALLISTO (Monstein, Ramesh, and Kathiravan, 2007; Benz *et al.*, 2009) in the frequency range ≈40 – 450 MHz. Note that observations of type II bursts over a limited spectral range as in the present work are not uncommon (refer for example Hariharan, Ramesh, and Kathiravan, 2015). We will discuss the above type II burst in the rest of this chapter.

Type II solar radio bursts are considered to originate from plasma waves excited by magnetohydrodynamic (MHD) shocks and converted into radio waves at the local plasma frequency and/or its harmonics. They are the direct diagnostic of MHD shocks in the solar atmosphere. These shocks accelerate electrons to suprathermal velocities. The energetic electrons excite Langmuir (plasma) waves that are converted into radio waves escaping the corona (refer Roberts, 1959; Wild, Smerd, and Weiss, 1963; Nelson, Sheridan, and Suzuki, 1985; Mann, Classen, and Aurass, 1995; Aurass, 1997; Gopalswamy, 2006a for details). The burst is recognized in radio spectral observations, where the intensity is plotted in the time-frequency

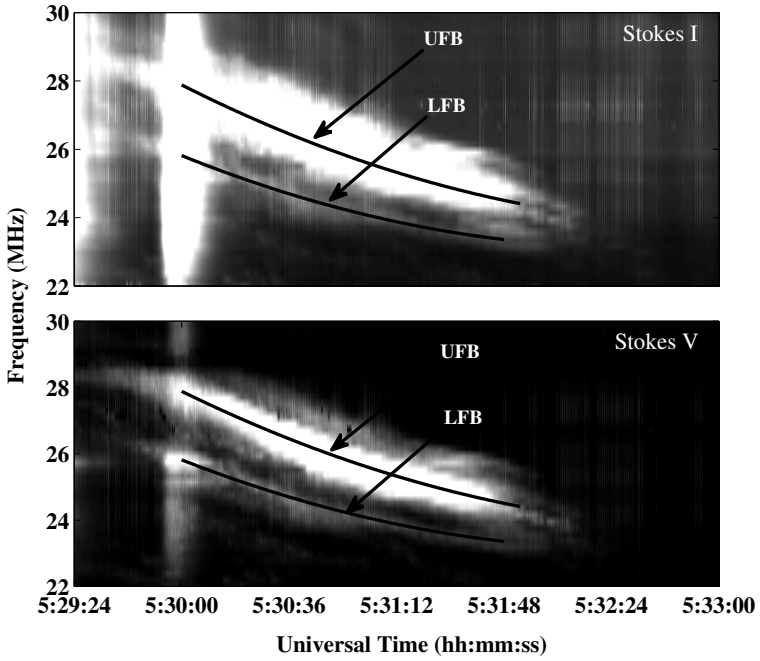

Figure 2.21: Type V burst (≈05:30 UT) and type II radio burst (≈05:30 – 05:32 UT) observed with the GRASP on 23 July 2016. The band-splitting of the type II burst is clearly visible in both the Stokes-I and Stokes-V spectra. The *black* lines indicate the upper and lower frequency bands of the split-band emission. The thin, closely spaced vertical lines seen in the spectra are artifacts.

plane, as a drift toward lower frequencies. This drift results from the decrease of the electron density with distance from the surface of the Sun. Both flares and coronal mass ejections (CMEs) are potential drivers of MHD shocks in the solar atmosphere (Nindos *et al.*, 2008).

A closer inspection of the type II burst in Figure 2.21 indicates that it is split, and appears as two bands (upper frequency band [UFB] and lower frequency band [LFB]). The frequency ranges are ≈28.0 – 24.2 MHz (UFB) and ≈26.0 – 23.5 MHz (LFB). The LFB and UFB bands relate to emission from the coronal regions ahead of and behind the associated MHD shock, respectively (Vršnak, 2001).

2.6.2.2 STEREO-A/COR1 and SOHO/LASCO-C2 Observations

The optical data were obtained with the *Large Angle and Spectrometric Coronagraph C2* (LASCO-C2; Brueckner *et al.*, 1995) on board the *Solar and Heliospheric Observatory* (SOHO), and the COR1 coronagraph of the *Sun-Earth Connection Coronal and Heliospheric Investigation* (SEECHI; Howard *et al.*, 2008) on board the *Solar Terrestrial Relationship Observatory* (STEREO). The type II burst in Figure 2.21 was associated with a white-light CME observed by the SOHO/LASCO-C2 and STEREO-A/COR1 coronagraphs. The CME was noted in

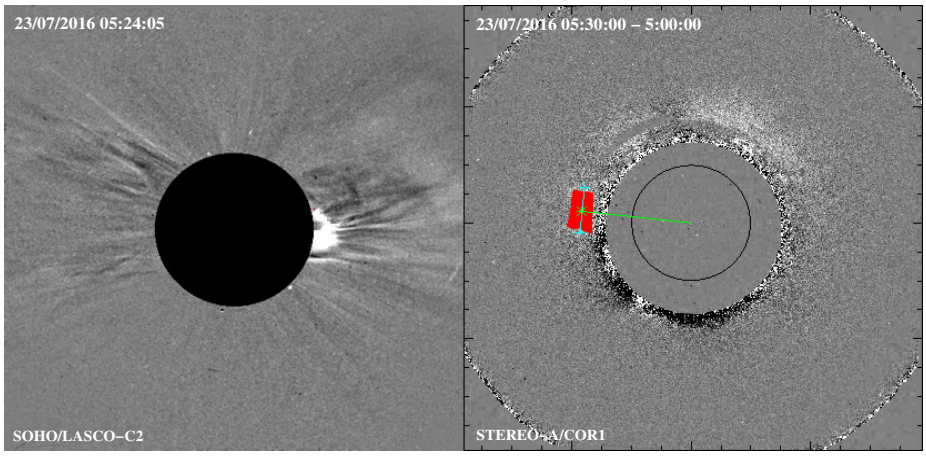

Figure 2.22: Left panel: SOHO/LASCO-C2 coronagraph difference image of the CME that occurred on 23 July 2016 around ≈05:24 UT. The *black* circle (radius ≈2.2 $R_\odot$) represents the occulting disk of the coronagraph. Solar north is straight up and east is to the left in the image. Right panel: STEREO-A/COR1 pB difference image of the same CME as in the left panel. The *black* and the *gray* circles indicate the solar limb (radius = 1 $R_\odot$) and the coronagraph occulter (radius ≈ 1.4 $R_\odot$), respectively. The CME is fainter than in SOHO/LASCO-C2 observations since its angle with respect to the plane of sky (POS) is relatively larger for STEREO-A (refer Section 2.6.2 for details). The electron density of the CME mentioned in Section 3.1 was estimated from the coronal region covered by the *red* rectangular box. The vertical line across the above box represents the width of the CME (≈ 0.79 $R_\odot$).

the SOHO/LASCO-C2 field of view (FOV) around ≈05:24 UT (refer left panel in Figure 2.22). Its central position angle (PA, measured counterclockwise from the solar north) during the above epoch is ≈267°, and the angular width is ≈65°. The projected heliocentric distance of the CME is ≈ 2.79 $R_\odot$[14]. A 3B class Hα flare from AR12565 was located on the solar disk at heliographic coordinates N02W75. The flare was observed during the interval ≈05:09 – 06:33 UT. The peak was at ≈05:31 UT[15]. The X-Ray Sensor (XRS) on board the *Geostationary Operational Environmental Satellite* (GOES-15) observed an M5.5 class soft X-ray flare from this active region, during the interval ≈05:27 – 05:33 UT. The peak time was the same as that of the Hα flare, i.e. ≈05:31 UT. This indicates that the onset of the type II burst (≈05:30 UT) in Figure 2.21 was close to the peak time of the flare.

The right panel in Figure 2.22 shows the STEREO-A/COR1 difference image of the solar corona obtained on 23 July 2016 at ≈05:30 UT. The boxed region at PA ≈84° indicates the same CME as recorded in the SOHO/LASCO-C2 observations in the left panel of Figure 2.22 at ≈5:24 UT. Its projected heliocentric distance in the STEREO-A/COR1 FOV is ≈ 1.86 $R_\odot$. The subtracted reference image for STEREO-A/COR1 in Figure 2.22 was observed at ≈05:00 UT. We found that

[14] http://spaceweather.gmu.edu/seeds/monthly.php?a=2016&b=07.
[15] ftp://ftp.ngdc.noaa.gov/STP/swpc_products/daily_reports/solar_event_reports/2016/07.

STEREO-A was at ≈E153° during these observations[16]. For the STEREO-A view, the flaring region is therefore located on the far side of the Sun at ≈42° behind the east limb. For the SOHO/LASCO-C2 view, this region is located on the solar disk at ≈15° from the west limb. The CME observations have projection effects that are due to disk locations. We calculated the de-projected heliocentric distances of the CME from the SOHO/LASCO-C2 and STEREO-A/COR1 images assuming that the projection effects vary as $1/\cos(\phi)$, where ϕ is the angle from the plane of sky (POS).

2.6.3 Analysis and Results

2.6.3.1 Estimates of N(r)

The electron density in the corona depends upon the brightness and the polarization in the corona (van de Hulst, 1950). We used polarized brightness (pB) measurements with the STEREO-A/COR1 and SOHO/LASCO-C2 coronagraphs (refer Figure 2.22) to find a suitable model for $N(r)$ to estimate the $B(r)$ values. In the case of STEREO-A/COR1, the $N(r)$ of the background corona and the CME were calculated using the images obtained at ≈05:00 UT (i.e. before the onset of the CME) and ≈05:30 UT (during the type II burst), respectively. These calculations were made using the spherically symmetric inversion technique (Wang and Davila, 2014). The $N(r)$ of the background corona was calculated in the distance range $r \approx$ 1.5-3.7 $R_\odot$ and over PA ≈84° ±5° (refer right panel in Figure 2.22). In case of the CME, the background-subtracted pB radiation from the boxed region in the right panel of Figure 2.22 was used. The deprojected heliocentric distance of the latter is ≈ 2.63 $R_\odot$. We assumed that the line-of-sight (LOS) depth of the CME is equal to its width, and the CME is at an angle of ≈42° relative to the POS (refer Section 2.6.2) for the above calculations. The $N(r)$ of the background corona and CME is $\approx 0.37 \times 10^6$ cm^{-3} and $\approx (1.8 \pm 3.3) \times 10^6$ cm^{-3}, respectively at $r \approx$ 2.63 $R_\odot$.

In the case of SOHO/LASCO-C2, the $N(r)$ of the background corona was calculated over the range PA ≈256° ± 5° using the image obtained at ≈02:54 UT (refer left panel in Figure 2.22). The distance range was $r \approx 2.3-5.5$ $R_\odot$. At the de-projected heliocentric distance ≈2.63 $R_\odot$, the background density is $\approx 0.43 \times 10^6$ cm^{-3}. Considering this along with the previously mentioned similar measurements with STEREO-A/COR1, the average $N(r)$ value in the background corona at the location of the CME ($r \approx$ 2.63 $R_\odot$) is $\approx 0.4 \times 10^6$ cm^{-3} (refer right panel in Figure 2.22). This implies that the total $N(r)$ at the CME location is $\approx 2.2 \times 10^6$ cm^{-3} (CME *plus* background corona).

Figure 2.23 shows the background density estimates for STEREO-A/COR1 and SOHO/LASCO-C2 for the distance range $r \approx 1.5-3.7$ $R_\odot$ and $r \approx 2.3-6.4$

[16] https://stereo-ssc.nascom.nasa.gov/cgi-bin/make_where_gif.

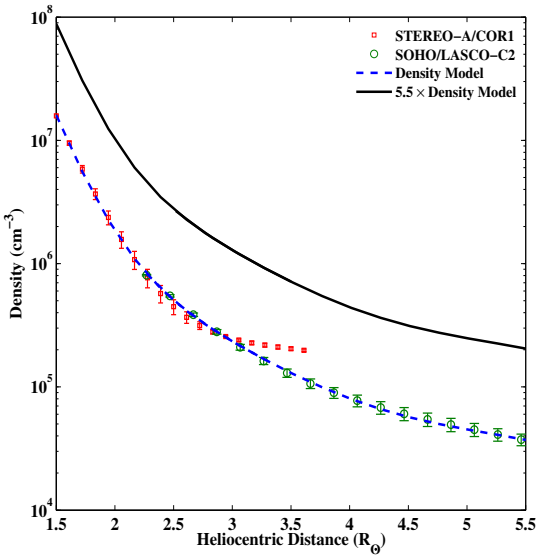

Figure 2.23: Estimates of $N(r)$ in the background corona using pB measurements with the STEREO-A/COR1 ($r \approx 1.5-3.7$ R$_\odot$) and the SOHO/LASCO-C2 ($r \approx 2.3-5.5$ R$_\odot$) coronagraphs. The *blue dashed* line ($r \approx 1.5-$ 5.5 R$_\odot$) is 5th order polynomial fit to the measurements of $N(r)$ with these two instruments. The *solid* line in the same distance range represents 5.5× the density values corresponding to the above fit. Note that this fit has excluded the COR1 data in the distance range $r \approx 3.0-$ 3.7 R$_\odot$ due to large uncertainty caused by instrumental noises (Wang *et al.*, 2017).

R$_\odot$, respectively. We found that the best fit to the background density in this height range and in the present case is a polynomial fit of 5th order, which can be expressed as $N_{\rm cor}(r) = 1.43 \times 10^9 r^{-5} - 1.91 \times 10^9 r^{-4} + 1.07 \times 10^9 r^{-3} - 2.87 \times 10^8 r^{-2} + 3.76 \times 10^7 r^{-1} - 1.91 \times 10^6$.

The plasma frequency ($f_{\rm p}$) corresponding to the estimates of the total density ($\approx 2.2 \times 10^6$ cm^{-3}) is $\approx$ 13.3 MHz. This implies that the type II burst in Figure 2.21 is most likely due to second harmonic ($2f_{\rm p}$) emission since its mean frequency at $\approx$ 05:30 UT is $\approx$ 27 MHz. The estimated maximum degree of circular polarization (dcp) is $\approx$18 % and the average dcp is $\approx$14 % of the type II burst, which is also consistent with that expected for harmonic plasma emission (Dulk and Suzuki, 1980). We would like to point out here that reports of third harmonic emission ($3f_{\rm p}$) of type II bursts have also been published, but such observations are rare (Roberts, 1959; Bakunin *et al.*, 1990: Kliem, Krueger, and Treumann, 1992; Zlotnik *et al.*, 1998). Interestingly, GLOSS observed the third harmonic emission of the above type II event in the frequency range $\approx 56-43$ MHz[17]. This was possible most likely because of the comparatively larger collecting area of GLOSS. Note that the GLOSS consists of eight antennas for radio frequency signal reception as compared to the typical solar radio spectrographs where only a single antenna is used (refer for example Benz *et al.*, 2009). Furthermore, the Sun was closer to the local zenith

[17] http://www.iiap.res.in/files/solarradioimages/gbd/GLOSS_20160723.jpg.

in Gauribidanur during the observations. The antenna gain is always maximum in that direction of the sky.

2.6.3.2 Speed of the CME

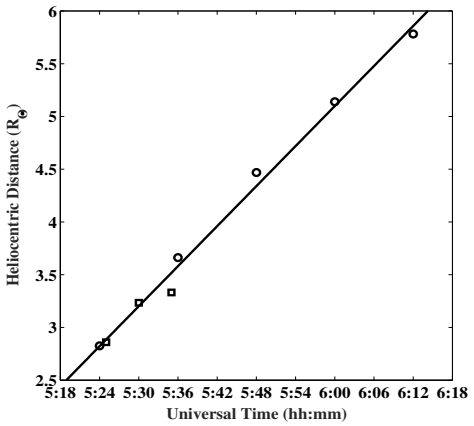

Figure 2.24: Height-time *(h-t)* plot showing the deprojected heliocentric distances of the CME Leading edge observed with the STEREO-A/COR1 coronagraph (indicated by *squares*) and SOHO/LASCO-C2 coronagraph (indicated by *circles*) on 23 July 2016 at different epochs. The *solid* line is the linear fit to the estimates.

The CME was recorded in the STEREO-A/COR1 FOV during ≈05:25 – 05:35 UT. In the case of SOHO/LASCO-C2, it was in the interval ≈05:24 – 06:12 UT. The deprojected height-time *(h-t)* plot of the CME LE obtained from the above observations is shown in Figure 2.24. The simultaneous measurements of the CME leading edge (LE) location with the two instruments during ≈05:24 – 05:36 UT are reasonably consistent. This confirms that the SOHO/LASCO-C2 and STEREO-A/COR1 observations described above correspond to the same CME. Its estimated speed ($v_{\rm CME}$) based on the linear fit to the *(h-t)* measurements in Figure 2.24 is ≈735 km/s.

2.6.3.3 Estimates of B(r)

Radio Observations : The pB measurements using STEREO-A/COR1 and SOHO/ LASCO-C2 coronagraphs described in Section 2.6.3 indicate that $N(r) \approx 2.2 \times 10^6$ cm^{-3} (CME *plus* background corona) at $r \approx 2.63$ R$_\odot$. This is $\approx 5.5 N_{\rm cor}(r)$ of the background corona at this location (refer Figure 2.23). We used the UFB and LFB bands of the type II burst (marked with black lines in Figure 2.21) to calculate $B(r)$ using the split-band technique (refer for example Vršnak *et al.*, 2002; Cho *et al.*, 2007). The drift rate of the burst is ≈0.35 MHz/s. We converted this drift rate of the burst into shock speed ($v_{\rm S}$) using the $5.5 N_{\rm cor}(r)$ model mentioned earlier (refer Section 2.6.3.1). The mean value of $v_{\rm S}$ for the four different spectra (i.e. LFB and UFB in Stokes-I and Stokes-V) is ≈ 800 km/s. This is nearly same

as the $v_{\rm CME}$ in Figure 2.24, implying that the type II burst is most likely due to the MHD shock driven by the CME LE (Ramesh *et al.*, 2010b; Ramesh *et al.*, 2012). The low start frequency of the type II burst also indicates the same (Gopalswamy, 2006a). We then calculated $B(r)$ using the following equation:

$$B(G) = 5.1 \times 10^{-5} v_{\rm A} f_{\rm p} \tag{2.8}$$

where $v_{\rm A}$ is the Alfv́en speed in units of km/s, and $f_{\rm p}$ is in MHz. It was obtained using parameters such as instantaneous bandwidth, density jump, Alfv́enic Mach number $M_{\rm A}$ related to the split-band type burst in Figure 2.23 (refer Vršnak *et al.*, 2002 for the relationship between the above parameters), and the relationship, $v_{\rm A} = v_{\rm S}/M_{\rm A}$.

The results indicate that $B(r) \approx (0.51-0.48) \pm 0.02$ G in the range $r \approx 2.65-2.82$ R$_\odot$. Note that this distance interval corresponds to $f_{\rm p} \approx 14-12$ MHz (the fundamental component of the split-band type II burst in the present case, refer Figure 2.21 and Section 2.2) since the $2f_{\rm p}$ emission occurring at the same time as the $f_{\rm p}$ emission should be generated at the same location as the $f_{\rm p}$ emission (Smerd, Wild, and Sheridan, 1962).

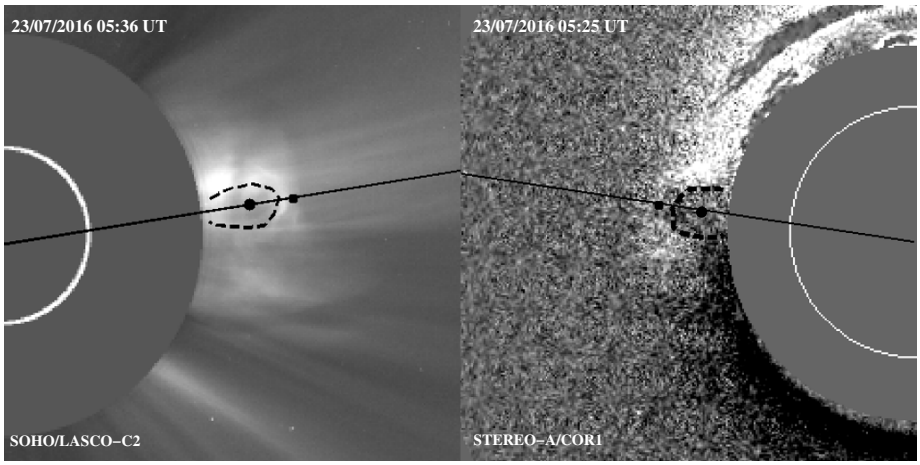

Figure 2.25: Left panel: Same as the observations shown in the left panel of Figure 2.22, but obtained at ≈05:36 UT. The *white* circle indicates the solar limb (radius = 1 R$_\odot$). The different features of the CME used for the estimates of B (referTable 2.6) are as follows: *black dashed* lines show the CME flux rope and *black dots* indicate the location of the CME shock and the center of the circle fitted to the flux rope. Right panel: Same as the observations in the right panel of Figure 2.22, but obtained at ≈05:25 UT. The *white* circle indicates the solar limb (radius = 1 R$_\odot$). The different features of the CME used for the estimates of B (refer Table 2.6) are as follows: the *black square* indicates the location of the CME shock, *black dashed* lines show the CME flux rope and the *black dot* represents center of the circle fitted to the flux rope (refer Gopalswamy et al., 2012 for details). The *black solid* line connects these CME features with the center of the Sun.

White-light Observations : We also estimated $B(r)$ using the white-light images obtained with STEREO-A/COR1 (right panel in Figure 2.25) and SOHO/LASCO-C2 (left panel in Figure 2.25), and the shock standoff distance technique described in Gopalswamy *et al.* (2012). The basic CME related parameters used in the above technique, i.e. the heliocentric distance of the CME flux rope $R_{\rm fl}$, the leading edge of the shock $R_{\rm sh}$ and the center of curvature of the flux rope $R_{\rm c}$ (*black dot* shown in Figure 2.25) were measured for these images as well as the next images that were observed with the respective coronagraphs. We assumed the adiabatic exponent γ to be 4/3 for the calculations. **This was the minimum value of γ for which the mach number was positive (Gopalswamy *et al.*, 2012).** The standoff distance ΔR, $M_{\rm A}$ and $v_{\rm s}$ were calculated using the parameters (refer Gopalswamy *et al.* (2012) for the relationship between the parameters), and $v_{\rm A}$ was estimated as earlier (Section 2.6.3.1). Adopting the same $5.5N_{\rm cor}(r)$ model as in the $B(r)$ estimate using the radio observations, we estimated the density for STEREO-A/COR1 and SOHO/LASCO-C2 at $r \approx 3.11$ $R_\odot$ and $r \approx 4.40$ $R_\odot$, respectively. The magnetic field strength in the corona was estimated using Equation 3, and the values are $B(r) \approx 0.32$ G at $r \approx$ 3.11 $R_\odot$ (STEREO-A/COR1) and $B(r) \approx 0.12$ G at $r \approx$ 4.40 $R_\odot$ (SOHO/LASCO-C2). The parameters related to these calculations are listed in Table 2.6.

Table 2.6: Parameters related to the estimates of $B(r)$ from white-light observations.

Time (UT)	$R_{\rm sh}$ ($R_\odot$)	$R_{\rm fl}$ ($R_\odot$)	$R_{\rm c}$ ($R_\odot$)	ΔR $[R_{\rm sh} - R_{\rm fl}]$ ($R_\odot$)	$N_{\rm e}$ $[5.5 \times N_{\rm cor}(r)]$ ($\times 10^5$ cm^{-3})	B (G)
STEREO-A/COR1						
05:25	2.75	2.30	0.26	0.45	-	-
05:30	3.11	2.50	0.37	0.61	11.2	0.32
SOHO/LASCO-C2						
05:36	3.54	3.37	0.36	0.17	-	-
05:48	4.40	4.02	0.61	0.38	3.33	0.12

2.6.3.4 Results

Figure 2.26 shows the combined plot of the different estimates of $B(r)$. We find that the radial dependence of the data points could be described by a single power-law relation of the form $B(r) = 6.7r^{-2.6}$ G. For comparison, the $B(r)$ models obtained by Dulk and McLean (1978), Vršnak *et al.* (2002), and the B values obtained by Kwon *et al.* (2013a; 2013b) are also over-plotted in Figure 2.26. We find that the $B(r)$ curve obtained in this study matches the result of Kwon *et al.* (2013a) **as it is within the error bar of our results. The power law index value computed by Dulk and McLean (1978) is 1.5 whereas the B field associated with the Type-II burst presented in this chapter seems to be steeper.**

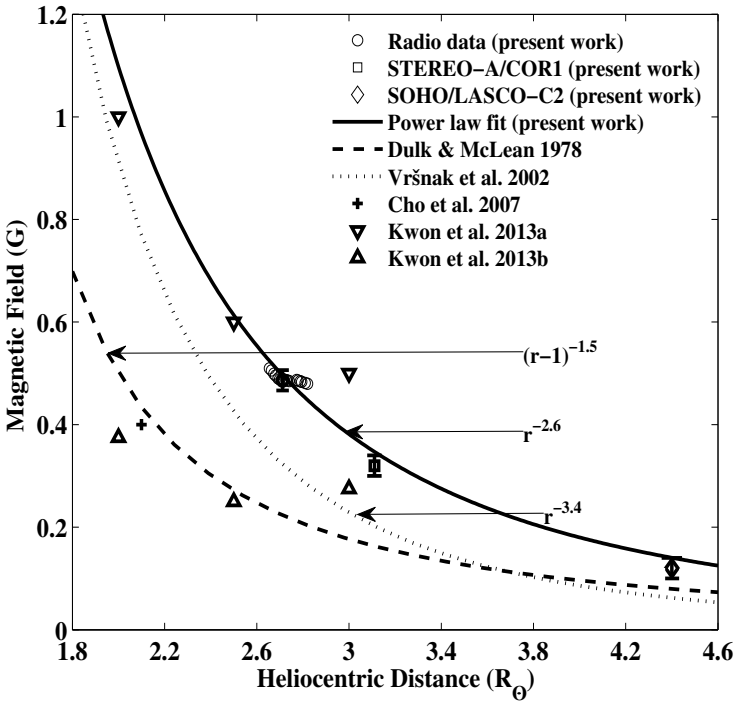

Figure 2.26: Estimates of $B(r)$ obtained using band-splitting of the type II radio burst in Figure 2.21, and the shock standoff technique applied to the associated white-light CME observed with the STEREO-A/COR1 and SOHO/LASCO-C2 coronagraphs.

Also, the power-law index (i.e.-2.6) is in good agreement with that mentioned in the literature by different authors for the variation of $B(r)$ in the outer corona: i) for example, using Faraday rotation observations of the linearly polarized carrier signals of the HELIOS spacecraft, Patzold *et al.* (1987) found that $B(r)$ varies as $r^{-2.7}$ in the range $r \approx 3-10$ R$_\odot$; ii) recently, Mancuso and Garzelli (2013b) reported $B(r) = 3.76r^{-2.29}$ G in the range $r \approx 5-14$ R$_\odot$ using observations of similar signals from extragalactic radio sources occulted by the solar corona. Considering $B(r)$ values at specific r in the outer corona (close to the range in the present work), we find that Spangler (2005) and Gopalswamy and Yashiro (2011) have estimated $B(r) \approx 39$ mG and ≈ 48 mG at $r \approx 6.2$ R$_\odot$ and ≈ 6.0 R$_\odot$, respectively. Compared to these, the power-law expression derived in this chapter predicts $B(r) \approx 58$ mG and ≈ 63 mG at the above distances, respectively. Therefore, unambiguous estimates of $B(r)$ in the middle corona can be obtained using radio and white-light observations upon identifying the appropriate $N(r)$.

Chapter 3
Wideband (50 - 500 MHz) Spectro-polarimeter

New Evidence for a Coronal Mass Ejection-driven High Frequency Type II Burst near the Sun
Anshu Kumari, R. Ramesh, C. Kathiravan and N. Gopalswamy, 2017, **The Astrophysical Journal**, 843, 10.

3.1 Introduction

Different forms of transient radio emissions such as type III and type II bursts, etc. were identified to be some of the probable precursors of space-weather events (Newkirk, 1961; McLean and Labrum, 1985a; Lin, Penn, and Tomczyk, 2000). Since many of these are polarized, one may improve the reliability of prediction by measuring their polarization with high time and polarization accuracy. Also, since the nature and degree of polarization depend upon the associated magnetic field strength and topology (Allen, 1947), one may quantify the latter and use as an additional parameter for prediction. Since these transient events originate at different heights in the corona almost near simultaneously, a broad-band spectro-polarimeter would be helpful to probe different coronal parameters such as the density, temperature, magnetic field strength and direction, etc. associated with these events (Allen, 1947).

Since the solar coronal mass ejections (CMEs) play a direct and vital role in deciding the space weather, it becomes inevitable to study their dynamical properties in the lower corona (i.e., over the radial distance range: 1.05 - 3.0 $R_{\odot}$; both prior to and after their time of eruption). In the previous chapter, a spectro-polarimeter that has a spectral coverage of 15 - 85 MHz was described. This chapter is going to discuss about a new wide-band spectro-polarimeter for probing the inner corona ($\leq$ 1.2 $R_{\odot}$). This second spectro-polarimeter was constructed using a wide-band (50 - 500 MHz) cross-polarized log-periodic dipole antenna (to receive orthogonal polarization), analog frontend and the old SA based digital backend receiver due to the

non-availability of ROACH board during initial stage of thesis work. This chapter describes the design, development and characterization of the antenna, configuration of analog and digital receiver components, and trial observations made with the system.

The cross-polarized Log-periodic structure (CLPD) that was chosen for the design falls under frequency independent antenna category (Rumsey, 1966; DuHamel and Isbell, 1966). The CLPDA is made up of two orthogonally oriented uni-axial log-periodic dipole antennas (LPDAs) (Sasikumar Raja *et al.*, 2013) .

3.2 Design and development of CLPDA

As explained in Chapter 3, LPDA is a coplanar array of unequal length and unequally spaced parallel linear dipoles fed at their center by a parallel transmission line of a specific characteristic impedance (Isbell, 1960). The structural and electrical characteristics of a LPDA vary periodically with the logarithm of frequency (Isbell, 1960; DuHamel and Isbell, 1966).

3.2.1 Design and fabrication of LPDA

The design aspects of a LPDA is explained in Section 2.2.1. Again, we used Carrel's equations for designing this antenna too. For the latter, we chose G = 6.5 dBi, so that the source would be within the beam of antenna for $\approx$ 5 hours. For G = 6.5 dBi, a number of τ and σ values can be selected from the Carrel's design curve. We chose $\tau = 0.86$ and $\sigma = 0.07$ for G = 6.5 dBi (which gives $\alpha = 27^o$), because of which the height of the antenna is limited to less than 3 m or so for easy handling, mounting, avoiding other mechanical requirements, etc.

The total number of dipole elements is 15 for the antenna. As a conservative design few more elements are usually added at the shorter arms side in order to improve the high frequency performance of the antenna and hence we ended up with 19 dipoles for our antenna. The design values, the dipole lengths, inter element spacing are listed in Table 3.1. After the fabrication of LPDA, its VSWR (Voltage standing wave ratio; a measure of impedance) was measured using RF analyzer. In practice, the VSWR of ≤ 2 is considered to be good as $\approx$ 89 % of total power is transferred to/from the load from/to the antenna. As one can see from Figure 3.1, the VSWR is found to be < 2 except at few frequencies (100 MHz, 140 MHz, 180 MHz and 450 MHz). This is due to impedance mismatch between the antenna and the transmission line at those frequencies. In order to correct the later, the VSWR response of dipole was studied as a function of its length and diameter over the desired frequency range. The following subsection describes that.

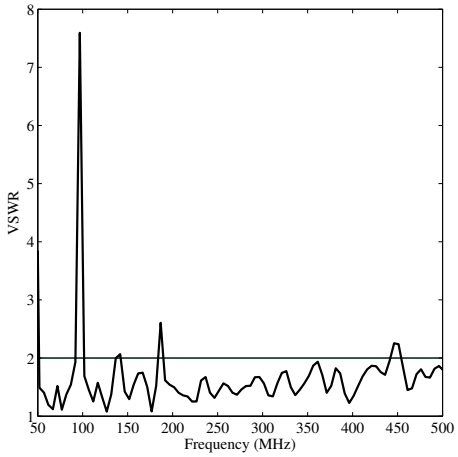

Figure 3.1: The VSWR pattern of the new wide-band LPDA. The VSWR is well below 2 for most of the frequencies except at 100, 140, 180 and 450 MHz.

Table 3.1: Design parameter values for LPDA (50 – 500 MHz)*

S. No.	Distance from top (cm)	Inter-element spacing (cm)	Length of dipole (cm)	Frequency (MHz)
1.	0.0	0	9.5	792.4
2.	3.1	3.1	11.0	682.3
3.	6.7	3.6	13.0	575.5
4.	10.9	4.2	15.1	497.7
5.	15.8	4.9	17.1	425.7
6.	21.5	5.7	20.2	371.9
7.	28.2	6.7	23.7	316.0
8.	35.9	7.8	27.8	269.7
9.	45.0	9.0	32.4	231.5
10.	55.5	10.5	38.0	197.4
11.	67.8	12.3	44.1	170.0
12.	82.2	14.3	51.2	146.4
13.	98.9	16.7	59.9	125.2
14.	118.4	19.5	69.0	107.8
15.	141.1	22.7	81.3	92.2
16.	167.6	26.5	95.1	78.9
17.	198.5	30.9	110.4	68.0
18.	234.5	36.0	129.2	58.0
19.	276.5	42	150.6	49.8

*These values were modified later to bring down the resonant peaks seen in the VSWR.

3.2.2 The length factor

As mentioned earlier, the LPDA is an array of dipoles connected to a common transmission line. For broadband operation of a LPDA, choosing the right set of resonant elements is important since the active centres of the reception/transmission change with frequencies. The frequency at which a dipole element resonate depends on its electrical length which is related to its physical dimensions through the velocity factor. In order to select the right set of dipoles to cover the 50 - 500 MHz frequency range, we carried out the tests with different length and diameter combinations. The result is shown in Figure 3.2; The velocity factor (v/c) as a function of length to diameter ratio is the wave propagation speed in the medium 'v', relative to the speed of light 'c'. In this method, by using a RF network analyzer, the resonant frequency for different lengths (starting from 500 cm to few cm) of half wave dipole antennas were measured over a frequency range $50 - 500$ MHz for Aluminum rods of different diameter (i.e 13, 8 and 6 mm). The resonant frequencies of dipoles were measured for a length interval of 1 cm until the resonance at 500 MHz was observed.

$$LF = \frac{L_{\mathrm{p}}}{L_{\mathrm{e}}} = \frac{c}{2 \times f_r} / \frac{c}{2 \times f_{\mathrm{obs}}} = \frac{f_{\mathrm{obs}}}{f_{\mathrm{r}}} \tag{3.1}$$

Here, f_{r} and f_{obs} is the calculated and observed resonant frequency respectively.

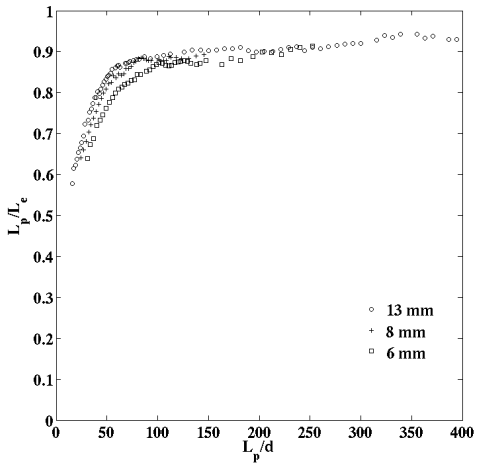

Figure 3.2: Length factor (LF) with respect to observed resonant frequency (f_{obs}) for Aluminum rods of 13 mm (indicated in 'circle'), 8 mm (indicated in 'plus') and 6 mm ('indicated in 'square') diameter.

Figure 3.2 shows the variation of LF with respect to observed resonant frequency, f_{obs}. From this experiment, one can infer that the LF for Aluminum rods of diameter 13 mm remains almost constant (i.e 0.89) from frequency $30 - 160$ MHz. Similarly, for rods of diameter 8 mm and 6 mm the constant frequency ranges are $160 - 320$ MHz and 320-500 MHz, respectively (refer Table 3.2).

Therefore, Aluminum rods of diameters 13 mm and 8 mm are finalized to use

Table 3.2: Mean length factor of Aluminum rods that can be used over 50 – 500 MHz

S. No.	Frequency (MHz)	Length L (cm)	Diameter d (mm)	LF
1.	50-161MHz	300-80	13	0.89
2.	161-320MHz	80-40	8	0.86
3.	320-480MHz	40-20	6	0.80

between frequency 50 – 320 MHz. As the LF for Aluminum rod of diameter 6 mm was lower than 0.86, the approximate diameter of Aluminum rod that can work in the 320 – 500 MHz was determined by extrapolation and its value is 4 mm. We applied this length factor constraint while designing the antenna, i.e. Aluminum rods of three different diameters were used to cover the entire bandwidth and two 15 mm × 6 mm (width and thickness) Aluminum flats were used as transmission lines with a spacing of 7 mm between them. The length of the transmission line is 3 m. The measured VSWR is shown in Figure 3.3. As mentioned earlier, the CLPDA is fabricated by fixing the transmission lines of two LPDAs orthogonal to each other with using an insulator (spacer) between them. The spacer is made in such a way that the inter-boom spacing (7 mm) is less than 1/100th of the wavelength of operation (Pivnenko, 2006) to have low polarization cross-talk. The revised VSWR over $50 - 500$ MHz was < 2 and the mean VSWR was ≈ 1.6. The picture of CLPDA is shown in Figure 3.4.

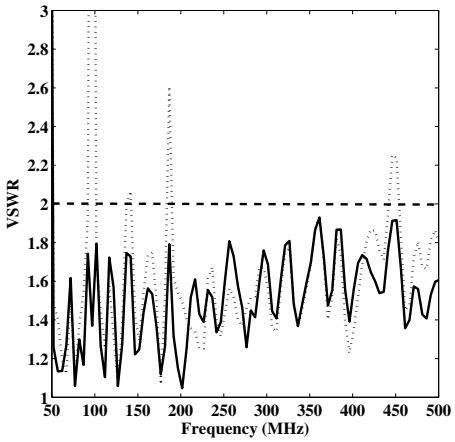

Figure 3.3: VSWR of the antenna before ('dashed' line) and after ('solid' line) applying correction factor (LF) and tuning.

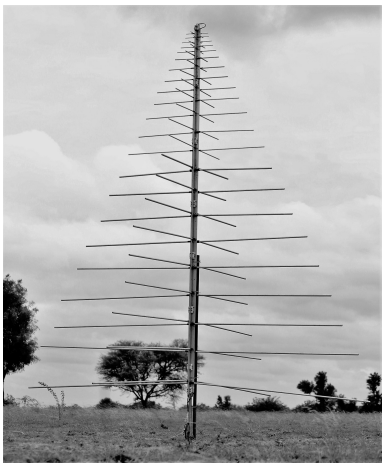

Figure 3.4: The newly developed CLPDA.

Table 3.3: Modified design parameter values of LPDA (50 – 500 MHz)

S. No.	from top distance (cm)	Inter-element spacing (cm)	Length (cm)	Frequency (MHz)
1.	0	0	9.5	792.4
2.	3	3	11.0	682.3
3.	7	4	13.0	575.5
4.	11	4	15.1	497.7
5.	15	4	17.1	438.4
6.	21	6	20.2	371.9
7.	29	8	24.2	309.4
8.	38	9	28.8	260.2
9.	47	9	33.4	224.5
10.	56	9	38.0	197.4
11.	68	12	44.1	170
12.	82	14	51.2	146.4
13.	97	15	58.9	127.4
14.	113	16	67.0	111.9
15.	131	18	76.2	98.4
16.	150	19	85.9	87.3
17.	171	21	96.6	77.6
18.	192	21	107.3	69.9
19.	214	22	118.5	63.3
20.	237	23	130.2	57.6
21.	259	22	141.4	53
22.	284	25	154.2	48.6

3.3 Characterization of the CLPDA

3.3.1 Antenna pattern measurements

3.3.1.1 Radiation pattern measurements

The far field radiation pattern was measured by keeping the transmitting and receiving antenna 25 m apart because the theoretical far field distance ($R > \frac{2D^2}{\lambda}$) is about 6 m. The designed antenna was used as a receiver and a LPDA whose transmission characteristics were already known, was used as the transmitter. For the measurement of E-plane radiation pattern, both the transmitting and receiving antennas were oriented horizontally and the receiver antenna was rotated by 360^o in the azimuthal plane from the reference position (azimuthal angle = 0^o) at an interval of 15^o. The same procedure was repeated for measuring the H-plane pattern with both the antennas oriented vertically. The measured half power beam width (HPBW) for E-plane and H-plane are 60^o and 110^o, respectively. Other antenna parameters e.g gain, effective area etc. were also calculated from the above and are listed in Table 3.4. These parameters were found to be almost constant throughout the 50 – 500 MHz band. Figure 3.5 shows the radiation pattern observed at 50 MHz, 300 MHz and 500 MHz for E-plane and H-plane respectively.

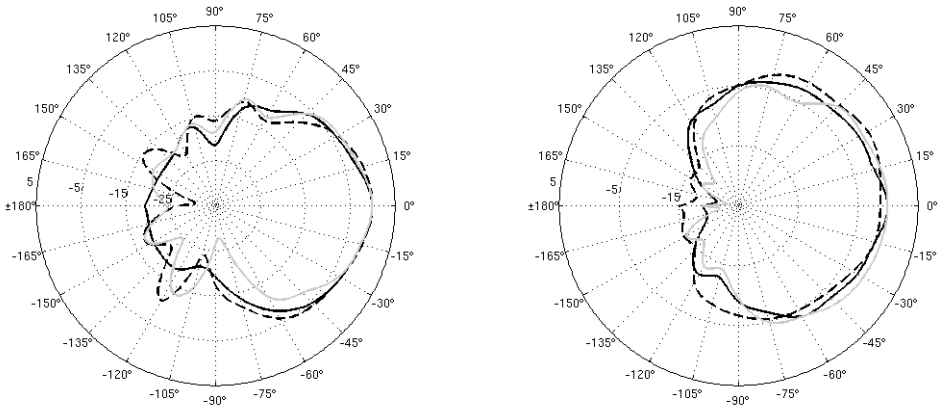

Figure 3.5: Measured E-plane (left panel) and H-plane (right panel) radiation pattern at 50 MHz ('gray'), 300 MHz ('black') and 500 MHz ('dashed')

3.3.1.2 Effective collecting area measurements

The effective collecting area (A_e) of the log periodic dipole antenna was calculated using the expression,

$$A_e = \frac{\lambda^2}{4\pi} \times G \tag{3.2}$$

where, A_e, λ and G are the total effective collecting area, observational wavelength and gain, respectively. The gain of the antenna can be measured by an absolute gain measurement method using the Friis transmission equation or by using the HPBW along the two principal planes. The latter method was used here to calculate the gain. The directional gain was calculated using the relation,

$$G = \frac{4\pi \frac{180}{\pi}^2}{HPBW_E \times HPBW_H} dBi \tag{3.3}$$

where, $HPBW_E$ and $HPBW_H$ are the HPBW in E and H planes, respectively. The $HPBW_E$ and $HPBW_H$ obtained in the previous section were used to calculate the directional gain of the antenna. The mean gain and effective collecting area of the antenna are ≈ 5.5 dBi and $\approx 0.45\lambda^2$.

Table 3.4: Deduced parameters from radiation pattern measurement

S. No.	Parameter	Value
1.	HPBW (E)	$\approx 60^o$
2.	HPBW (H)	$\approx 110^o$
3.	Gain	6.9 dBi
4.	Effective Area	0.45 λ^2
5.	Front to back ratio	34 dB
6.	Side lobe ratio	-33 dB

3.3.1.3 Estimation of polarization cross talk

Polarization of an antenna depends upon its geometry Stutzman and Thiele (1981). For e.g a helical antenna is circularly polarized whereas a dipole antenna is linearly polarized. Since our primary objective is to detect circular polarization using a CLPDA (refer Section 3.1), restricting the E & H-fields within a narrow region about their respective mean position of vibration is very important to reduce the spill over of one polarization component into the other. The latter decides the accuracy with which polarization measurements are made. Polarization cross talk is a measure of received power corresponding to one sense of polarization by an antenna when it is exposed to polarization of the other sense (Wakabayashi *et al.*, 1999; Pivnenko, 2006). So, as mentioned above, optimization of this parameter is important to estimate the degree of circular polarization (DCP) of radiation received from an astronomical source and hence in the determination of magnetic field strength subsequently. In order to determine the cross talk, we transmitted horizontally polarized radiation at every 25 MHz interval and measured both hor-

izontal and vertical polarization using the designed antenna. The estimated cross talk is about ≈ -30 dB (refer Figure 3.6).

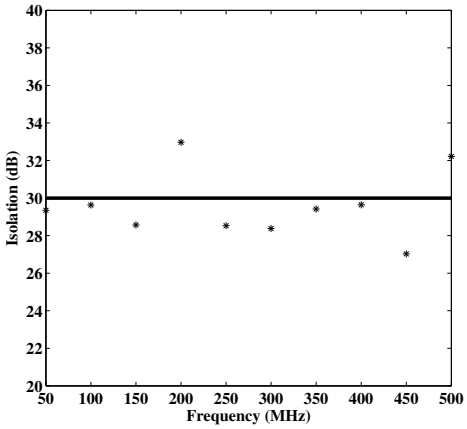

Figure 3.6: Measured isolation of CLPDA. Here 'star' shows the measured isolation value with a 'solid black' line as mean isolation value

Table 3.5: Antenna Parameters of CLPDA

1.	Frequency Range	50-500 MHz
2.	No. of dipoles	22
3.	Design Constant (τ)	0.86
4.	Spacing Constant (σ)	0.07
5.	VSWR	$\leq$2
6.	$HPBW_E$	60°
7.	$HPBW_H$	110°
8.	Collecting Area (A_e)	$0.4\lambda^2$
9.	Gain (G)	6.9 dBi
10.	Front-to-back ratio	34 dB
9.	Isolation	-30 dB

3.3.2 Back-end Description

The signal received by the two arms of the CLPDA are fed to an analog front-end receiver. The first component is a pre-amplifier with gain ≈ 30 dB that amplifies the signal. Then it is passed through a high-pass filter with a cut-off frequency $f_c = 50$ MHz to avoid low radio frequency interference (RFI). A FM rejection filter is also used to remove FM band (88 – 108 MHz). The two signals are brought to the laboratory via optical fibre cables. A second stage amplifier with gain ≈ 30 dB is connected to ensure the required power level at the input of RF-to-optical converter. In the lab, the signals are converted back into RF and then given to the inputs of quadrature hybrid (QH) (Pozar, 2009). The output of the QH is given to

two conventional spectrum analysers (SAs). For data acquisition, a code written in VEE pro is used. Both SAs are initialized through GPIB communication which sets the observational parameters, e.g. start and end frequency, sweep rate, BW resolution, number of spectra to be averaged onboard, etc. An initial trigger is given to start the frequency sweep using a software. These averaged spectra are written in the data acquisition computer using GPIB communication. The block diagram of the wide-band spectro-polarimeter set-up is shown in Figure 3.7.

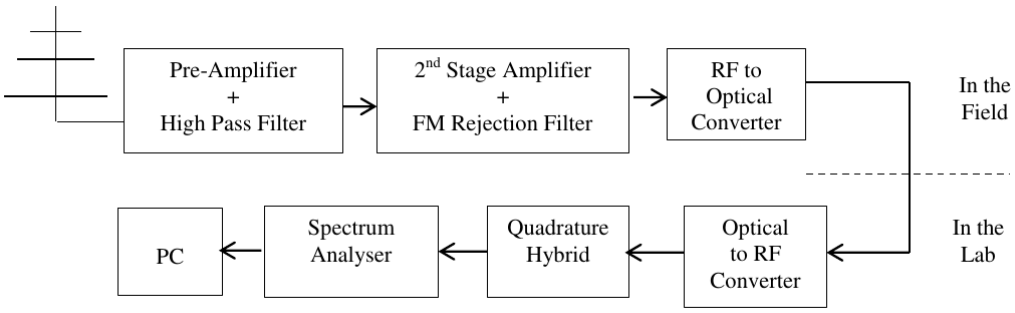

Figure 3.7: Block diagram of the spectro-polarimetric setup

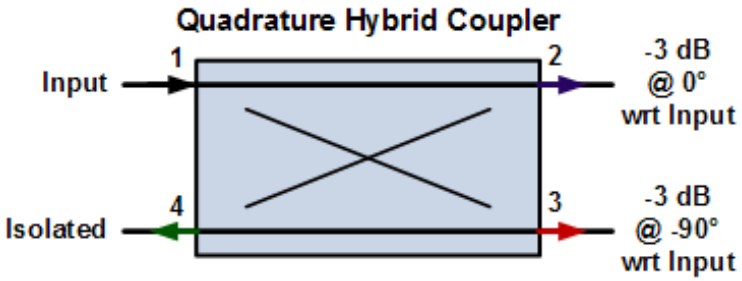

Figure 3.8: Block diagram of a quadrature hybrid.

A QH is a device that has two transmission lines pass close enough to each other for coupling the signal travelling on one line with the other line. This splits the input signal into two parts whose amplitude are nearly equal but with 90^o phase difference. These are symmetrical in terms of their input and output ports. The block diagram of a QH is shown in Figure 3.8. For a CLPDA, as the orientations of the two arms are orthogonal, the signal received by one arm will have a phase difference of 90^o with respect to the other. If the signal transmitted by the transmitting antenna is assumed to be 2A, the components of this signal that fall on the two orthogonal arms can be written as,

$$A_{\mathrm{x}}(t) = A_{\mathrm{ox}} e^{i\delta_x} e^{i\omega t} \tag{3.4}$$

$$A_{\mathrm{y}}(t) = A_{\mathrm{oy}} e^{i\delta_y} e^{i\omega t} \tag{3.5}$$

Table 3.6: Output of the quadrature hybrid for different polarized inputs

S. No.	Tx Signal	$A_{QH}^{0^o}(t)$	$A_{QH}^{90^o}(t)$
1.	LP (horizontal)	$\frac{A_o}{\sqrt{2}}$	$\frac{A_o}{\sqrt{2}}$
2.	LP (vertical)	$\frac{A_o}{\sqrt{2}}$	$\frac{A_o}{\sqrt{2}}$
3.	CP (Right)	$\frac{A_o}{\sqrt{2}}$	0
4.	CP (Left)	0	$\frac{A_o}{\sqrt{2}}$

Here, A_{ox}, A_{oy}, δ_x, δ_y and ω are instantaneous amplitude, phase and angular frequency, respectively. The two outputs of the QH $A_{QH}^{0^o}(t)$ and $A_{QH}^{90^o}(t)$ are written as,

$$A_{QH}^{0^o}(t) = \frac{A_{ox}}{\sqrt{2}} e^{i\delta_x} e^{i\omega t} + \frac{A_{oy}}{\sqrt{2}} e^{i\delta_y} e^{i\omega t} e^{i\phi} \tag{3.6}$$

$$A_{QH}^{90^o}(t) = \frac{A_{ox}}{\sqrt{2}} e^{i\delta_x} e^{i\omega t} e^{i\phi} + \frac{A_{oy}}{\sqrt{2}} e^{i\delta_y} e^{i\omega t} \tag{3.7}$$

In case of QH, the phase shift angle $\phi = 90^o$. Table IV shows the expected values at the output of QH when linearly polarized (LP) and circularly polarized (CP) signal are received by the CLPDA.

The RF signal is fed to a sweep based SA. The data is acquired by computer using Peripheral Component Interconnect/General Purpose Interface Bus (PCI/GPIB) interface and VEE-Pro software. The SA works on superheterodyne principle that uses a mixer and a local oscillator signal (LO) to translate the observing frequency into intermediate frequency (IF). These signals are then fed to the IF filter, whose output is detected. The LO is swept with an increment of 1 MHz to obtain 401 frequency samples in the RF band of 50 - 500 MHz. The instrument takes 4 ms to sweep 450 MHz and 250 ms to transfer the spectrum data to the data acquisition computer.

3.3.3 Error in DCP estimation

In 1852, G. Stokes (Collett, 1992) proved that the polarization behaviour of an EM wave could be represented by four parameters, viz. I, Q, U, V ; the latter are called the Stokes parameters. For any state of polarized light, Stokes parameters always satisfy the relation given in equation 3.8.

$$I^2 \geq Q^2 + U^2 + V^2 \tag{3.8}$$

Here I is the total intensity, Q is the amount of linear polarization in horizontal

or vertical orientation, U is the amount of linear polarization in $\pm 45^o$ and V is the amount of circular polarization present in the signal. The degree of circular polarization (DCP) is defined as,

$$DCP = \frac{|V|}{|I|} \tag{3.9}$$

The values of DCP range between 0 and 1, where 0 represents unpolarized signal and 1 represents completely circularly polarized signal. To estimate the Stokes parameters and the DCP accurately, the contributions of the antenna and the back-end electronics to the circular polarization have to be determined accurately. To carry out the measurements, we designed helical antennas (both Left Circularly Polarized and Right CP) that can be operated over frequency range 200 – 400 MHz. The percentage of CP was measured by transmitting a circularly polarized radiation using the above helical antennas (LCP and RCP) and measured the output levels 0^o and 90^o arms of the CLPDA. The measured DCP values when transmitted with LCP helical antenna are $\approx$ 98%, 99%, 98% and 97% at 325 MHz, 350 MHz, 375 MHz and 400 MHz, respectively. The corresponding values for the test with RCP helical antenna are 99%, 98%, 97% and 98% , respectively.

For calibration, we used median subtraction technique, i.e. the data obtained immediately after the start of an observation was subtracted from the data throughout the observation from each signal path. This was done to compensate for the losses and the frequency characteristics of the electronics and cables. Also, two different transmitting antennas to transmit horizontal and vertical polarization were used for the above experiment. The calibration method described earlier was applied to the signals and DCP was calculated. The plots obtained for 320 MHz are shown in the Figures 3.9 and 3.10. Depending upon the signal strength in these channels, the handedness of the CP signal are determined. The positive and negative DCP values corresponds to LCP and RCP respectively. The estimated error in DCP for the observing system is $\approx$ 2%.

3.4 Observations

The observational set-up described in Section 3.3.2 is being operated at Gauribidanur observatory, since October, 2015. One of the events observed is a solar type V burst on 02^{nd} May, 2016[1]. Type V bursts are the signatures of propagating non thermal electron beams along curved paths in the solar atmosphere. They are due to synchrotron radiation when the electrons moves spirally in the solar magnetic fields with near relativistic speed (Stewart *et al.*, 1965). The Stokes-I and Stokes-V spectra are shown in Figure 3.11. They were obtained from the recorded signal by using the following set of equations:

[1] ftp://ftp.swpc.noaa.gov/pub/indices/events/20160502events.txt.

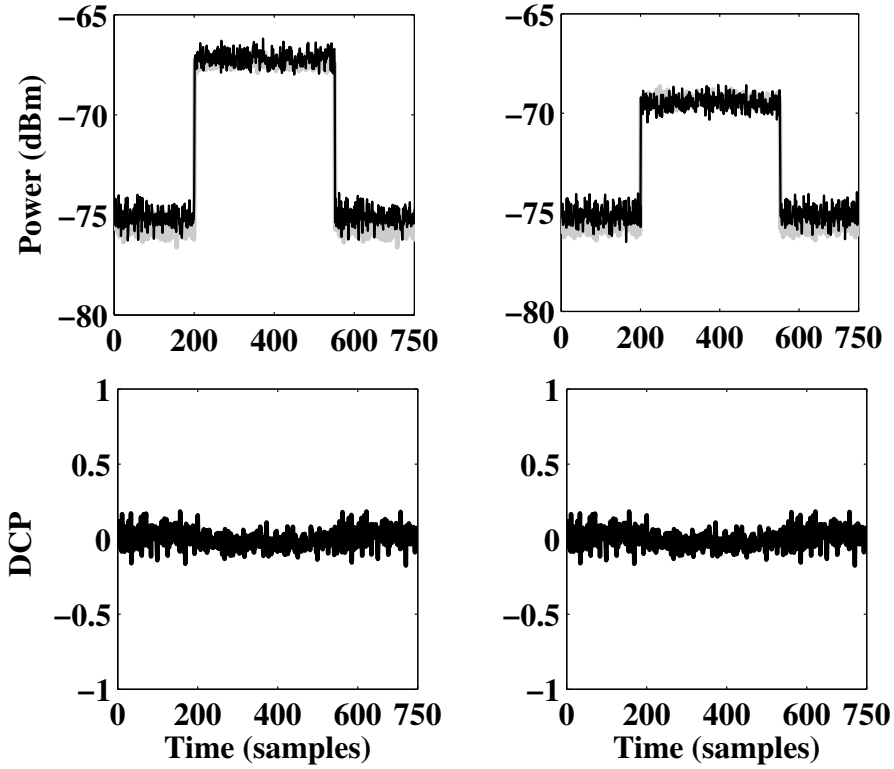

Figure 3.9: Upper panel: Measured Power at the two output ports of QH, $P^{0^o}_{\mathrm{QH}}(t)$ ('black') and $P^{90^o}_{\mathrm{QH}}(t)$ ('gray') when linear polarized signal is transmitted. The left and right panel shows horizontal and vertical polarized signal, respectively. Lower panel: Estimated DCP of the signals shown in upper panel..

$$P^{0^o}_{\mathrm{QH}}(t)(\mathrm{mW}) = 10^{\frac{\mathrm{P}^{0^o}_{\mathrm{QH}}(\mathrm{t})(\mathrm{dBm})}{10}} \tag{3.10}$$

$$P^{90^o}_{\mathrm{QH}}(t)(\mathrm{mW}) = 10^{\frac{\mathrm{P}^{90^o}_{\mathrm{QH}}(\mathrm{t})(\mathrm{dBm})}{10}} \tag{3.11}$$

$$I(\mathrm{mW}) = \left|\frac{\mathrm{P}^{0^o}_{\mathrm{QH}}(\mathrm{t})(\mathrm{mW}) + \mathrm{P}^{90^o}_{\mathrm{QH}}(\mathrm{t})(\mathrm{mW})}{2}\right| \tag{3.12}$$

$$V(\mathrm{mW}) = \left|\frac{\mathrm{P}^{0^o}_{\mathrm{QH}}(\mathrm{t})(\mathrm{linear}) - \mathrm{P}^{90^o}_{\mathrm{QH}}(\mathrm{t})(\mathrm{linear})}{2}\right| \tag{3.13}$$

$$I(\mathrm{dBm}) = 10\log(\mathrm{I(mW)}) \tag{3.14}$$

$$V(\mathrm{dBm}) = 10\log(\mathrm{V(mW)}) \tag{3.15}$$

Using equation 3.9 (refer Section 3.3.3), the DCP of the type V burst was calculated at discrete frequencies and plotted against the heliocentric distance using Newkirk's density model (Newkirk, 1961) with an enhancement factor of 2 (refer Figure 3.12). The DCP varies between 1 % to 6 % over heliocentric distance (r) range $\approx 1.1 - 1.9\ \mathrm{R}_{\odot}$.

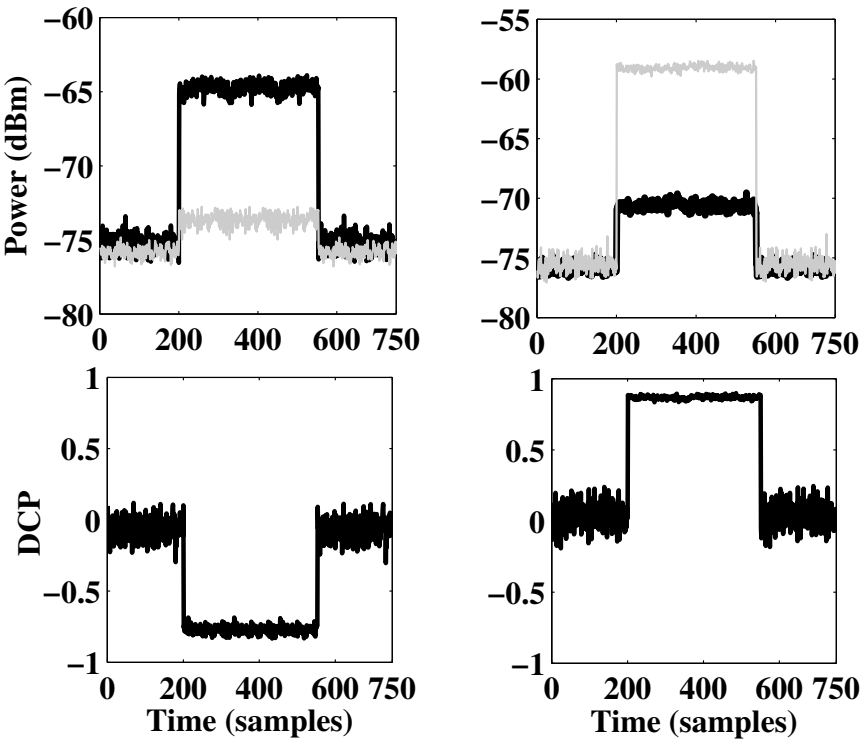

Figure 3.10: Upper panel: Same as Figure 3.9 but when circularly polarized signal is transmitted. The left and right panel shows left and right polarized signal, respectively. Lower panel: Estimated DCP of the signals shown in the upper panel.

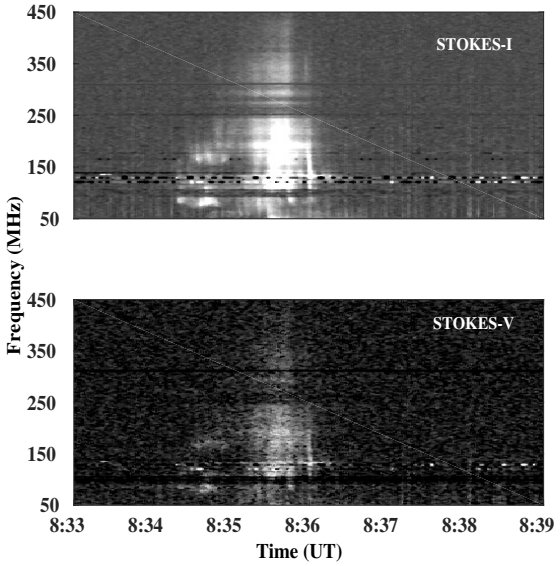

Figure 3.11: Stokes-I and Stokes-V spectra of a type V burst observed on 2^{nd} May, 2016

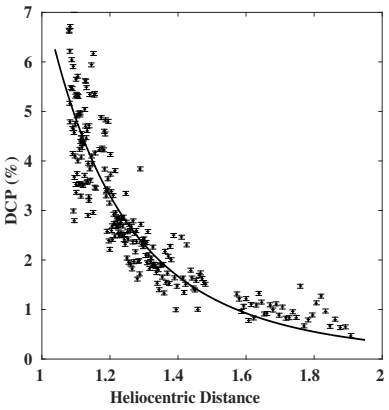

Figure 3.12: DCP (error bar of 2%) of type-V burst as function of heliocentric distance.

The magnetic field associated with the event was estimated using second harmonic plasma emission approximation (McLean and Labrum, 1985a),

$$B = \frac{f_{\rm p} \times DCP}{2.8 \times a(\theta)} \tag{3.16}$$

where, B is magnetic field, f_p is plasma frequency and θ is viewing angle. Figure 3.13 shows the distribution of magnetic field strength as a function of heliocentric distance. The power-law fit to the data points gives $B(r) = 6.3r^{-3.9}$. This distribution is very similar to previously obtained results. Lin, Kuhn, and Coulter (2004) estimated $B(r)$ field 4 G at 1.1 $R_{\odot}$. Patzold *et al.* (1987) found the $B(r)$ field variation in the middle corona as $r^{-2.7}$.

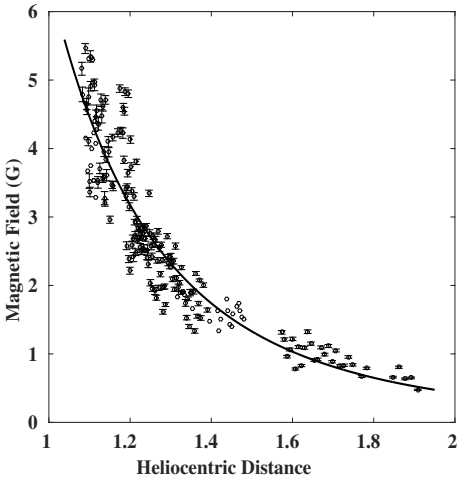

Figure 3.13: Radial variation of magnetic fields associated with type-V.

3.5 Wideband Digital backend for CLPDA

When ROACH board became available during the late stage of thesis work, a new wideband (50 - 500 MHz) digital back-end system for spectro-polarimetric monitoring of the solar corona was designed. The first component of this system is the same CLPDA as described in the previous section. The signals received with the two arms of the CLPDA are transmitted from the field to the lab through the same sets of analog components. Finally, the signals are fed to a spectro-polarimetric correlator that is implemented on ROACH board provided by CASPER community. This spectro-polarimetric correlator also computes the total intensity (Stokes-I) and circular polarized intensity (Stokes-V) of the received signal.

3.5.1 Digital Spectro-polarimeter Design

The RF signals are directly digitized using iADC[2] at Nyquist rate. The heart of the iADC is an Atmel/e2V AT84AD001B sampler, which can sample two analog channels simultaneously at a maximum rate of 1 GHz or a single analog channel at 2 GHz rate. The ADC is operated in the former mode. This ADC is chosen because the maximum **sampling** rate it provides is 1000 MCPS (as our band of interest is 50 - 500 MHz), and it had a dynamic range of $\approx$ 48 dB to record strong and weak solar transient events in the presence of strong RFI. **In order to operate the ADC/FPGA in the safer range, we have reduced the sampling rate from 1000 MHz/s (maximum limit) to 800 MHz/s.** The output of the ADC is transmitted as Low Voltage Differential Signal (LVDS) data which is subsequently captured on the FPGA. The data is cast as a signed fixed point number (8 bits of data, and the decimal point is at the 7th bit, 8.7) on which further signal processing operations are performed. The digitized time series data are filtered using 4 tap polyphase filterbank (PFB). The polyphase filter reduces leakage between neighbouring spectral channels compared to a normal FFT operation as described in the previous chapter. This is crucial as at low frequencies RFIs may sweep weak signal in the neighbouring channels. A 8192 point real-sampled Fast Fourier Transform using the standard Hermitian conjugation trick to use a complex core to transform a single real stream using half the normal resources is calculated. For 8192 point FFT, the FFT block outputs 2048 cosine values (odd) and 2048 sine values (even) making 4096 values in total.

For obtaining the dynamic spectra of the Sun, correlations are computed. The sum of auto-correlation of the two orthogonal signals corresponds to Stokes-I, and the sum of imaginary components of the cross-correlations of the same corresponds to Stokes-V as described in the previous chapter. The polarization leakage is taken care by computing the real part of the cross-correlations, which is expected to be negligible in the present case. If this real part of the cross correlation is present in

[2] https://casper.ssl.berkeley.edu/wiki/ADC2x1000-8

the signal, it is subtracted from the imaginary component of the cross correlation signal in order to remove the polarization leakage.

The spectral and temporal resolution of this instrument is 100 kHz and 100 ms. There are two vector accumulators (RAMs) used to accumulate the spectra, one for the odd and another for the even frequency channels. In order to prevent the multiplication and accumulation blocks from saturation, the signals are re-quantized to 8.7 fixed point. This signal is accumulated in block RAMs of 4096 point lengths for a programmable integration time. The vector length is set to 2048 on each accumulators. The data in each frequency channel is 64 bit wide. The data is then transferred to the storage devise using 10 Gbe. A packetizer is made to pack the input spectra channels into 4 frames (packets) of size 1024 64-bit words each. The final spectrum from the odd and even channels are packetized using FIFO buffers which help to improve the throughput by a factor 2, and thereby the spectral resolution. Although, theoretically larger N FFTs can be performed, we restricted to an 8192 point FFT to make sure a single set of odd/even spectral points is accommodated in a single Ethernet packet. This way, the spectra are reconstructed even if some packets get dropped randomly during capture by the interface. The packetizer module is used to generate appropriate control signals like Enable, Start of Frame, End of Frame etc. for the 10 Gb Ethernet. The data is captured onboard with an acquisition PC using TCPDUMP[3], open source network packet capture software. This is required for data transmission using 10 Gb Ethernet because the buffer capacity is 1024 64-bit words. Preliminary observations of Galactic Centre (GC) and the Sun were carried out and few results obtained from them are discussed in the following sections.

3.5.2 Observations: Calibration & Comparison

3.5.2.1 Galactic centre observations

Once the system was built, it was kept for the observation of Galactic centre (GC) which transits at ≈ 17:46:13 LST. This observation helped us to determine the beam size of the antenna, which is ≈ 70^o. Figure 3.14 shows the power recorded with ROACH at 150 MHz during the meridian transit of GC at Gauribidanur. **The three peaks at time samples ∼ 7500, 12500 and 37500 are due to the Global Positioning System (GPS) satellites[4]. The narrow band spikes in the data are due to local RFIs. The step at ∼ 26000 time sample is because of the occasional gain compression of the ADC.**

[3] https://www.tcpdump.org/tcpdump_man.html.
[4] https://www.spaceacademy.net.au/spacelink/radiospace.htm

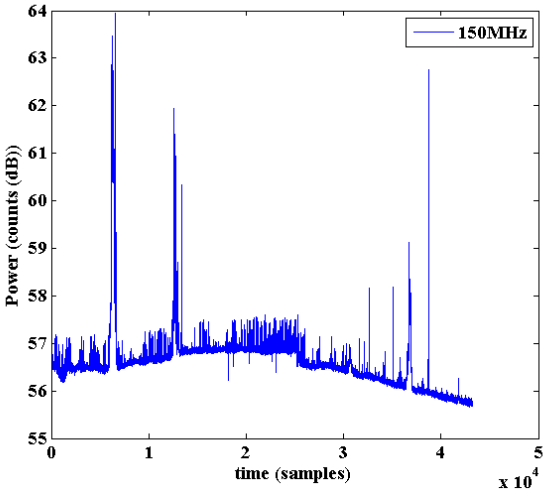

Figure 3.14: Observed radio emission from the Galactic background at 150 MHz using the new wide-band spectro-polarimeter.

3.5.2.2 Solar Observations

Both ROACH and SA based system were kept simultaneously to observe the Sun for comparing their performance. On Apr 21, 2019, a type II burst was observed during ≈ 04:45:00 - 04:54:00 UT. Figure 3.15b shows the dynamic spectra obtained with Learmonth spectrograph[5]. This burst was accompanied with B1.1 class X-ray flare as seen by GOES13 (refer Figure 3.15a). There was a CME during the same time seen with SOHO/LASCO-c2, which has a speed ≈ 450 km/s.

The dynamic spectra shown in Figure 3.16 contains the ROACH and SA spectra. The brightness enhancements seen around ≈ 04:42 and 05:00 UT are type III bursts. The slowly drifting feature between ≈ 04:45 - 04:54 UT is the type II burst which has been analyzed here to compare the two instruments. Also, the Learmonth spectra shown in Figure 3.15b (the spectral and temporal resolution is ≈ 1 MHz and ≈ 3 sec, respectively) the burst appears to be faint. When we see the same in ROACH spectra, because of higher SNR (≈ 18 dB more than SA based system), the spectra is seen with better contrast (refer Figure 3.16). Also, another important thing here to notice is that the type II burst almost fades away above ≈ 80 MHz in SA spectra, while it can be seen in ROACH spectra till 150 MHz. This is mainly because of better sensitivity of ROACH as compared to SA.

Figure 3.17a shows the band averaged temporal profile of the radio bursts from 50 - 80 MHz. Along with the two type III bursts at ≈ 04:42 UT and ≈ 05:00 UT, and type II burst ≈ 04:45 - 04:50 UT, there are few minor enhancements at ≈ 04:50-04:54 UT. This is not visible in the SA spectrum even after band averaging. The right panel of the same figure (refer Figure 3.17b), SA data is averaged for

[5] ftp://ftp-out.sws.bom.gov.au/wdc/wdc_spec/data/learmonth/images/19/20190421spectrograph.gif

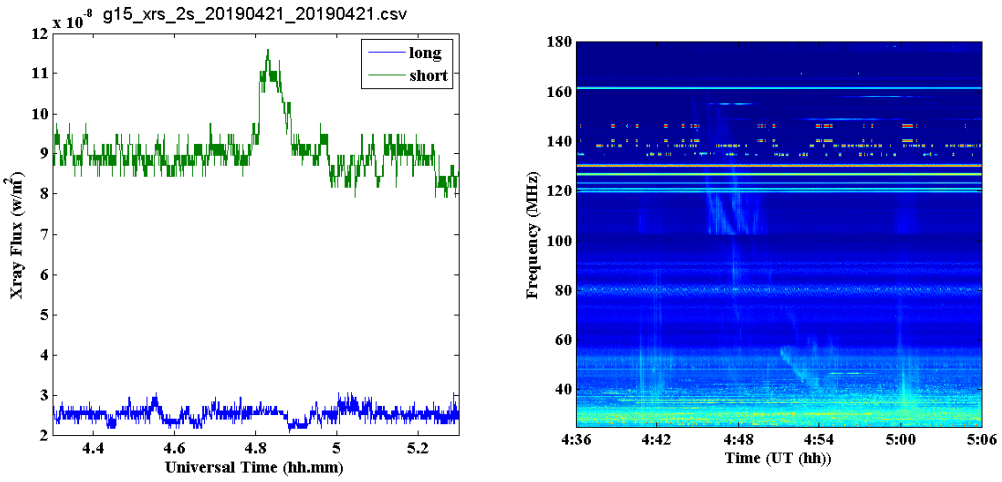

(a) (b)

Figure 3.15: The X-ray light curve for B1.1 class flare observed with GOES13 (left) and The solar dynamic spectrum obtained with Learmonth Spectrograph (right). The radio bursts appear to be weak in the spectrum.

1 sec (4 data points), and the enhancements at ≈ 04:50 - 04:54 UT are visible. However, this can not be used in a real time data because if the burst duration is ≤ 1 sec, the feature would disappear. Here, the data were normalized to compare the dynamic range of the system.

Figure 3.18 shows the light curve of the same burst at 50 MHz without any smoothing in time or spectral channel. The noise fluctuations in SA and ROACH are of order 10^{-5} and 10^{-7}, respectively, which imply that the noise has been reduced in the new digital system by an order of two. Table 3.7 shows the comparison of SNR of these two systems.

Table 3.7: Comparison of SA and ROACH backends.

Frequency (MHz)	Peak Signal (mW) SA/ROACH	Noise (rms) SA/ROACH	SNR SA/ROACH	Improvement linear scale/ decibel scale
50	2.5e-3	4.6e-5	54	75/18
	2.8e-3	6.8e-7	4105	
60	1.4e-3	3.6e-5	38	75/18
	1.7e-3	5.9e-7	2878	
70	8.1e-4	3.6e-5	23	45/16
	8.2e-4	8.2e-7	995	
80	2.7e-4	2.3e-5	11	71/18
	2.4e-4	2.9e-7	828	

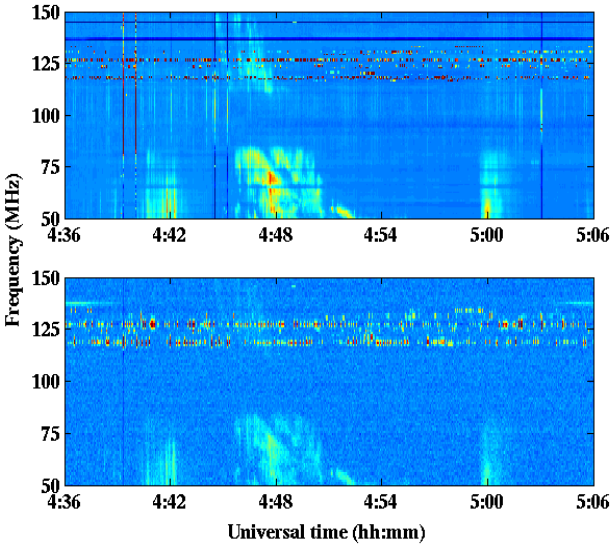

Figure 3.16: The dynamic spectra of type II burst observed on 21 Apr, 2019. The top and bottom panel corresponds to ROACH and SA spectrum, respectively. Due to high dynamic range and better SNR of the ROACH system, the weak burst (in Stokes-I) at ≈ 4:48 UT is seen with better contrast in the top panel.

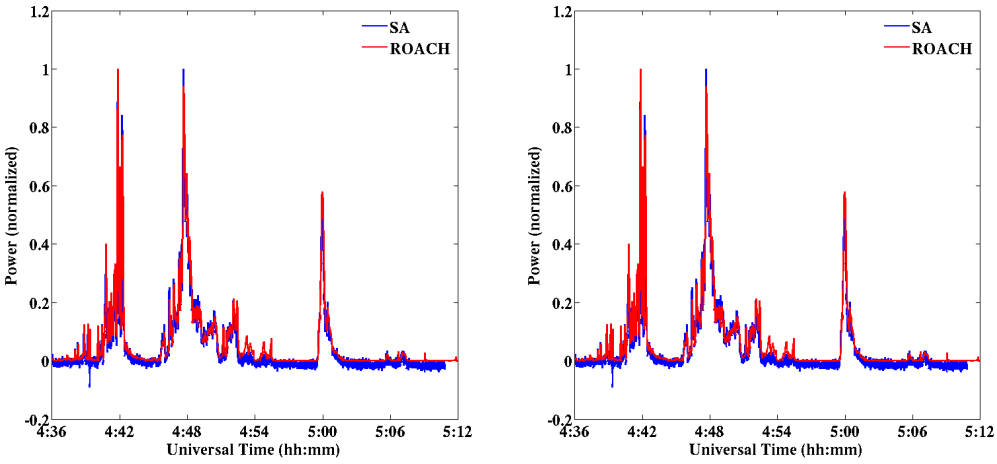

(a) **(b)**

Figure 3.17: Left panel: The band averaged (50 - 84 MHz) power recorded as a function of time of the type II burst using ROACH ('red') & SA ('blue') systems. The noisy ('blue') profile indicates that its SNR is lesser than 'red' color profile. Also, the small peaks are seen with better contrast with ROACH receiver than with SA. For example, the weak features seen during ≈ 04:51-04:54 UT. Right Panel: Same as left panel; but SA data is averaged for 1 sec (4 points) due to which the features in SA data begin to appear.

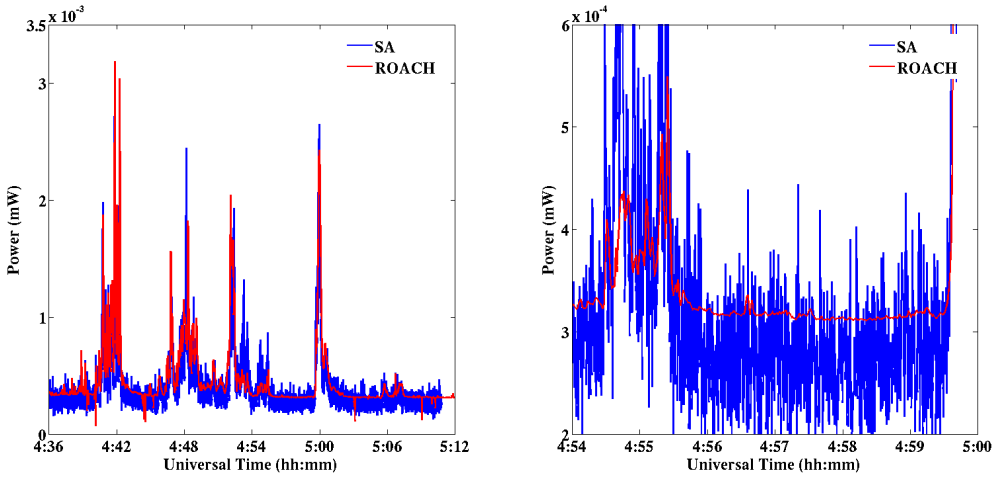

(a) (b)

Figure 3.18: Left panel: The light curve of the type II burst observed at 50 MHz using SA and ROACH systems; Right Panel: The noise fluctuations in both systems.

3.6 A type II burst observed with Wideband spectro-polarimeter

3.6.1 Introduction

It is widely accepted now that the low frequency ($\leq$ 14 MHz) type II bursts observed in the outer corona ($r > 3R$, **where r is in terms of distance from the Sun and the solar radius being R**) and the interplanetary medium are due to MHD shocks piston-driven by the associated CMEs (Gopalswamy, 2006b). One of the main reasons for this is that simultaneous observations of CMEs in whitelight are available for almost all the bursts in the corresponding distance where the bursts are observed. Even in the case of coronal type II bursts with start frequencies $<$ 150 MHz, spatio-temporal association with CMEs has been extensively reported (Cliver, Webb, and Howard, 1999; Claßen and Aurass, 2002; Cliver, Kahler, and Reames, 2004; Mancuso and Raymond, 2004).

The high frequency coronal type II bursts (start frequencies $>$ 150 MHz) however seem to be an exception. The bursts are attributed to MHD shocks driven by flare blast waves (Vrsnak *et al.*, 1995; Shanmugaraju, Moon, and Vrsnak, 2009; Zucca *et al.*, 2014b). But EUV observations show CME/shock formation associated with type II radio bursts with start frequency $\approx$ 150 MHz (Magdalenić *et al.*, 2012). Therefore, it is likely that the above discrepancy could be due to the fact that the high frequency type II bursts originate close to the Sun (i.e., over r $>$ 1.5 $R_\odot$), where whitelight observations of CMEs and their kinematics are limited at present. In this situation, we report for the first time the shock speed profile of a CME-associated high frequency coronal type II burst and its correlation with the

light curve of the associated soft X-ray flare. This study shows that high frequency type II bursts and the associated X-ray flare observations with high temporal resolution help us to under-stand the kinematics of the associated CMEs close to the Sun.

3.6.2 Observations

The radio imaging and spectral observations were carried out with the Gauribidanur RAdioheliograPH (GRAPH; Ramesh *et al.* (1998)) at 80 MHz, and with the wideband Gauribidanur RAdio SpectroPolarimeter (GRASP; Kishore *et al.* (2014), refer section 3.2 for details) in the frequency range $500-50$ MHz, respectively. The angular resolution of the GRAPH is $\approx 5' \times 7'$ (RA $\times$ Dec) at the above frequency. The integration time is $\approx$ 250 ms. The antenna and the receiver systems were calibrated by carrying out observations in the direction of the Galactic center as described in Kishore *et al.* (2014). We used images obtained in whitelight with the Large Angle and Spectrometric Coronagraph (LASCO; Brueckner *et al.* (1995)) on board the Solar and Heliospheric Observatory (SOHO) for information on the CMEs, and in 171 Å/211 Å with the Atmospheric Imaging Assembly (AIA; Lemen *et al.* (2012)) on board the Solar Dynamics Observatory (SDO) to identify the source region of the CMEs and their counterparts closer to the Sun.

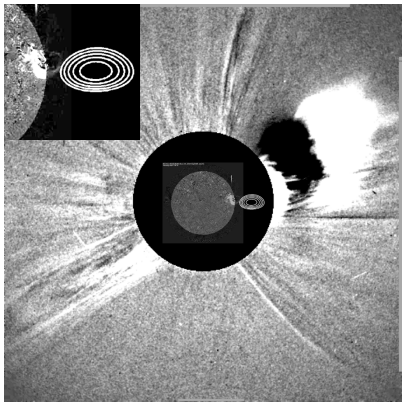

Figure 3.19: Composite of the 80 MHz radioheliogram of the type II burst observed on 2015 November 4 at 03:31 UT with GRAPH, the associated SOHO/LASCO-C2 difference image obtained at $\approx$ 04:00 UT, and the SDO/AIA 211 Å image obtained at $\approx$ 03:26 UT. Solar north is straight up and east is to the left. The "black" circle indicates the occulting disk of the coronagraph. Its radius is ≈ 2.2 $R_\odot$ The bright emission emerging above the coronagraph occulter on its west corresponds to the CME mentioned in the text. The other dark and bright features located farther above is nearly the same P.A. range correspond to an earlier CME that was first observed in the SOHO/LASCO-C2 FOV at $\approx$ 02:12 UT. The intense discrete radio source (shown in white contours) at r ≈ 1.5 $R_\odot$ is the type II burst mentioned in the text. Its peak brightness temperature (T_b) is $\approx 2.2 \times 10^8$ K. The contours shown (inner to outermost) are at $97.5\%, 95\%, 92.5\%, 90\%$ and 87.5% of the peak T_b . The contour interval is $\approx 5.5 \times 10^6$ K. The inset is a close-up view of the activity in AR1 2445 observed with SDO/AIA 211 Å and the location of the radio burst. The CME can be noticed as a faint loop-like structure above the limb. Its LE is located at ≈ 1.1 $R_\odot$.

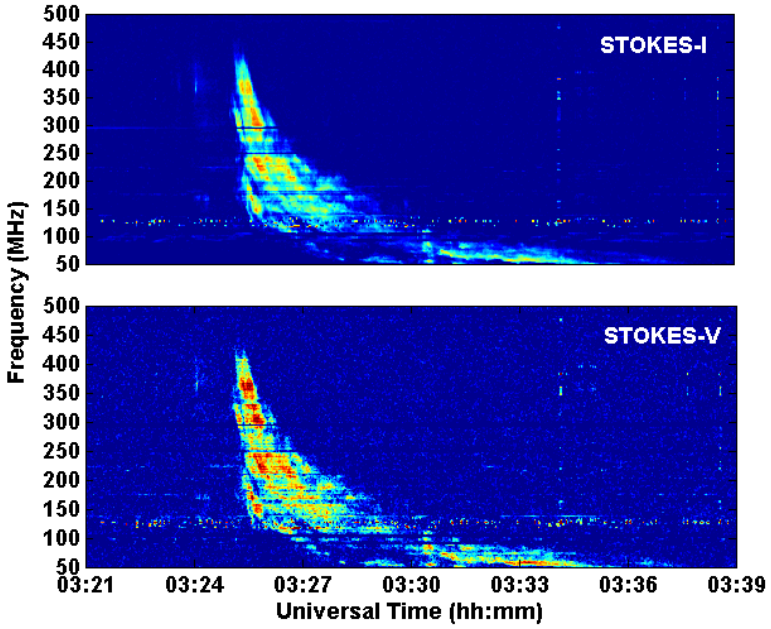

Figure 3.20: GRASP observations of the Stokes-I (upper panel) and Stokes-V (lower panel) dynamic spectra of the type II burst of 2015 November 4 in Figure 3.19 . The horizontal features in the spectra close to 300 and 100 MHz are due to local radio frequency interference (RFI).

Figure 3.19 shows the composite of the type II burst observed with GRAPH on 2015 November 4 at 03:31 UT, the SOHO/ LASCO-C2 running difference image of the associated CME around ≈ 04:00 UT, the epoch at which it was first noticed in the FOV of the coronagraph, and the SDO/AIA 211 Å image obtained at ≈ 03:26 UT. The central position angle (P.A., measured counterclockwise from the solar north) of the CME is ≈ 278^o, and its angular width is ≈ 64^o. Its leading edge (LE) is located around ≈ 2.8± 0.4 $R_\odot$[6]. The position of the centroid of the type II burst is ≈ 1.5± 0.2 $R_\odot$. The possible error in the position of the burst is due to propagation effects such as scattering by density inhomogeneities in the solar corona and/or refraction in the Earth's ionosphere (Stewart and McLean, 1982; Ramesh, Subramanian, and Sastry, 1999; Ramesh *et al.*, 2006; Mercier *et al.*, 2006; Kathiravan *et al.*, 2011; Mugundhan, Hariharan, and Ramesh, 2017). The fact that the Sun is presently going through a period of extended minimum (during which the observations reported in this work were carried out) also indicates that scattering will be less (Sasikumar Raja *et al.*, 2016).

The GRAPH observations at 80 MHz were made ≈ 29 minutes before the CME appeared in the SOHO/LASCO-C2 FOV. Figure 3.20 shows the GRASP observations of the dynamic spectrum of the aforementioned type II burst in both Stokes-I

[6] https://cdaw.gsfc.nasa.gov

and Stokes-V. The onset frequency is ≈ 430 MHz at ≈ 03:25:05 UT. The fundamental and harmonic emission bands can be clearly noticed. Their spectral widths are consistent with those of similar high frequency type II bursts reported in the literature (refer, for example, Zimovets *et al.* (2012); Cho *et al.* (2013)). The burst was also present in the Gauribidanur LOw-frequency Solar Spectrometer (GLOSS; Ebenezer *et al.* (2007); Kishore *et al.* (2015)) observations carried out over the frequency range 35 - 85 MHz and the e-CALLISTO observations elsewhere during the same epoch (Monstein, Ramesh, and Kathiravan, 2007; Benz *et al.*, 2009). This helped to independently establish the spectral class of the burst. An inspection of the observations on 2015 November 4 with the Wind/WAVES instrument indicates that the above burst was limited to frequencies ≥ 14 MHz, i.e., it did not extend into the interplanetary medium[7]. The low frequency cutoff must have probably been between 35 and 14 MHz. An inspection of the GLOSS dynamic spectrum[8] indicates that the GRAPH observations in Figure 3.19 at 80 MHz corresponds to the harmonic component of the type II burst. These strengthen our above assumption regarding the source position since the effects of scattering on the position of the harmonic component of a solar radio burst is expected to be minimal compared to the fundamental component (Riddle, 1974; Robinson, 1985).

The X-Ray Sensor (XRS) on board the Geostationary Operational Environmental Satellite (GOES-15)[9] recorded an M1.9 class soft X-ray flare from AR 12445 located at N14W64 on the Sun [10] during the interval ≈ 03:20–03:29 UT. The flare maximum was at ≈ 03:25 UT. There was also a 1N class Hα flare during the interval ≈ 03:23 – 03:34 UT, with maximum at ≈ 03:25 UT [11]. We independently verified this using observations with the Hα telescope in the Kodaikanal Observatory (Ravindra *et al.*, 2016). A comparison of the above timings indicate that the type II burst occurred almost at the same time as the flare maximum. An inspection of the successive SDO/AIA images revealed that the above CME was accompanied by an extreme-ultraviolet (EUV) wave from the associated active region (Thompson *et al.*, 2000).

3.6.3 Analysis and Results

As mentioned earlier, the 80 MHz type II burst in Figure 3.19 corresponds to the harmonic component and is located at ≈ 1.5 $R_\odot$. The corresponding deprojected location is ≈ 1.7 $R_\odot$. This agrees reasonably with the location of the 40 MHz plasma layer (fundamental component of the burst) estimated using the relationship between the starting frequency (f) of the type II burst and r corresponding to the LE of the associated CME, i.e., $f(r) = 307.87 \times r^{-3.78} - 0.14$ derived by Gopalswamy

[7] http://solar-radio.gsfc.nasa.gov/index.html
[8] http://www.iiap.res.in/files/solarradioimages/gbd/GLOSS_20151104.jpg
[9] https://www.ospo.noaa.gov/Operations/GOES/15/index.html
[10] www.lmsal.com/solarsoft/latest_events
[11] ftp://ftp.swpc.noaa.gov/pub/warehouse

et al. (2013a). We converted the above power law to a "model" (hereinafter referred to as the Gopalswamy model) for the electron density distribution ($N_e(r)$) using the equality $f(r) = 9 \times 10^{-3}\sqrt{N_e(r)}$ (where $f(r)$ and $N_e(r)$ are in units of MHz and cm^{-3}, respectively) and estimated the speed of the MHD shock associated with the type II burst in Figure 3.20 . Note that we used the above relationship since it was obtained from a statistical study of type II bursts and the associated CMEs. The assumptions were very minimal, and the list included events with high starting frequencies as in the present case. The associated CMEs were "limb" events. So, the projection effects are expected to be less. Further, both the CME LE and the EUV wave diameter methods used by the authors (to infer the CME height at the time of type II burst onset) gave nearly identical results for the events where it was possible for them to use both methods. Finally, the $r^{-7.56}$density variation in the above model takes care of possible "clearing" of the corona by the preceding CME as in the present case (refer caption of Figure 3.19).

In this regard, we would like to point out that Ramesh and Sastry (2000) had estimated that the density varies as r^{-10} in the region of the corona where a CME-induced depletion was observed. Note that according to the conventional density models (derived mostly using whitelight observations carried out during total solar eclipses), the density varies uniformly as r^{-6} in the "middle" corona, i.e., 1.1 - 3.0 $R_\odot$. Figure 3.21 shows the height-time (h–t) details of the CME LE in SOHO/LASCO-C2 observations, EUV wavefront LE in the SDO/AIA 171 Å images, and the location of the type II burst in observations with GRAPH at 80 MHz and GRASP at select frequencies. The EUV and radio measurements are in the distance range $r \approx 1$ - 2 $R_\odot$. Initially, both the EUV wavefront and the type II burst exhibit acceleration, and there is also good consistency between their h–t measurements. But the EUV wavefront slows down after a while. The type II burst shows continued acceleration for some more time (refer Figure 3.22). Later, it also slows down, and its h-t measurements matches with the linear extrapolation (in the Sunward direction) of similar measurements of the CME LE (over the range $\approx 3 - 7$ $R_\odot$). This indicates a close association between the type II burst and the CME LE.

Since the duration of the burst is long in the present case (≈10 minutes in the frequency range ≈ 430–50 MHz), we estimated the speed of the associated shock at different time intervals. The start and end frequencies of the burst were different in each estimation. The results are shown in Figure 3.22 along with the X-ray light curve obtained with GOES-15/XRS in the 1.6–12.4 keV (1–8 Å) energy band and the time profile of the EUV 171 Å wavefront speed. We find that the onset of the type II burst at ≈ 03:25:05 UT is close to the time (≈ 03:24:35 UT) when the speed of the EUV wavefront was the maximum (≈ 1893 km/s). There is also a good agreement between the latter and the initial shock speed of the type II burst (≈ 1958 km/s). The above consistency in the speeds and the initial agreement

between their h–t measurements (refer Figure 3.21) indicate that the type II burst and the EUV wave are both driven by the same CME (Patsourakos and Vourlidas, 2012; Liu and Ofman, 2014). But the observational evidences that the onset of the EUV wave (≈ 03:24:10 UT) is about one minute earlier to the onset of the type II burst and the EUV wavefront starts decelerating earlier (≈ 03:24:35 UT) compared to the type II burst (≈ 03:25:30 UT) suggest otherwise (refer, for example, Kumar, Innes, and Cho (2016)). This needs to be verified statistically.

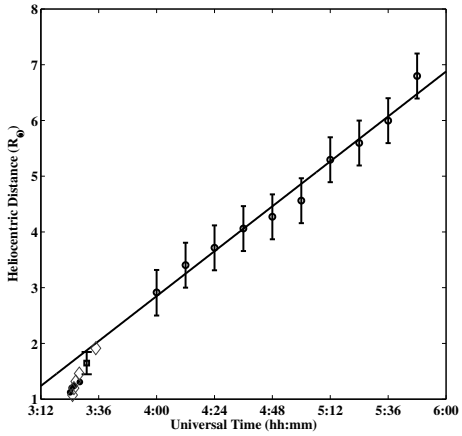

Figure 3.21: Height–time plot of the CME LE (indicated by the circles) observed with the SOHO/LASCO-C2 coronagraph, LE of the EUV wavefront (indicated by the dots) observed with SDO/AIA 171 Å, and the type II burst observed with GRAPH at 80 MHz (indicated by the square) and with GRASP at select frequencies (430, 310, 215, 150, 50 MHz—indicated by the diamonds). Note that all of the aforementioned frequencies correspond to the harmonic component of the type II burst.

Figure 3.22 indicates that the type II burst shock speed increased from ≈ 1958 km/s to ≈ 2441 km/s during the interval ≈ 03:25:05 - 03:25:30 UT. The corresponding acceleration is ≈ 17 km s^{-2}. Such a large acceleration, though unreported, is likely (Vršnak and Cliver, 2008). Cho *et al.* (2013) had reported a similar high frequency type II burst associated with a CME event, but from near the center of the solar disk, where the latter exhibited a strong acceleration (≈ 8 km s^{-2}) for a very short time interval of ≈ 1 minute as in the present case. Note that the drift rate of the burst, estimated close to ≈ 215 MHz (the start frequency of the fundamental component; refer Figure 3.20) is ≈ 2 MHz/s. The shock speed decreased to ≈ 1910 km/s at ≈ 03:27 UT. The deceleration during this interval is ≈ - 6 km/s^2. The deceleration beyond ≈ 03:27 UT is ≈- 2 km/s^2. The speed of the shock close to ≈ 03:33 UT is ≈ 1125 km/s. We estimated the probable location of the type II burst at 03:25:34 UT (i.e., when the shock speed was at maximum) based on its deprojected location of ≈ 1.7 ± 0.2 $R_\odot$ at 03:31 UT and the kinematics of the associated MHD shock during the interval between the above two epochs. The calculations indicate that the burst should have been located at ≤1.12 $R_\odot$. This is reasonably consistent with the location of the CME LE in the SDO/AIA 211 Å

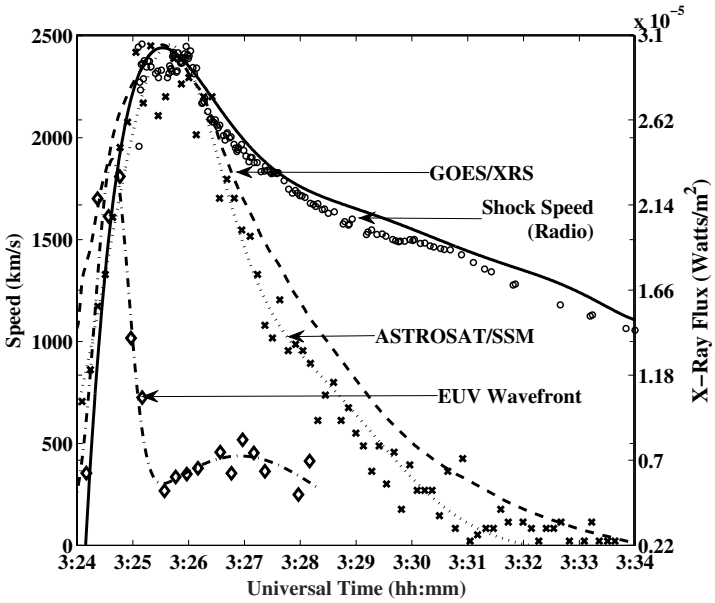

Figure 3.22: Time profile of the MHD shock speed (indicated by the circles) corresponding to the type II burst in Figure 3.20, time profile of the speed of the LE of the SDO/AIA 171 Å EUV wavefront (indicated by the diamonds), and the GOES-15/XRS light curve of the associated X-ray flare (indicated by the dashed line) obtained with a temporal resolution of ≈ 2 s. The thick line is the fit to the shock speed estimates, and the dotted line is the fit to the EUV measurements.

image at ≈ 03:26 UT (refer Figure 3.19). This implies that the peak acceleration of the CME in the present case was over by the time it reached $r \approx 1.1$ $R_\odot$. This agrees well with the reports that the CMEs reach their peak acceleration at $r \leq 1.1$ $R_\odot$ (Bein *et al.*, 2011), and the MHD shock associated with high frequency (≤ 200 MHz) type II bursts occurs at $r < 1.1$ $R_\odot$ (Gopalswamy *et al.*, 2013b). Note that the drift rate of the burst, estimated close to ≈ 215 MHz (the start frequency of the fundamental component; refer Figure 3.20), is ≈ 2 MHz/s . Unusually high drift rates like this, which are probably indicative of a fast shock, seem to be typical of high frequency type II bursts (refer, for example, Mann *et al.* (2003); Pohjolainen, Pomoell, and Vainio (2008); Zimovets *et al.* (2012)).

There is a good correspondence between the time profile of the type II burst shock speed and the X-ray light curve of the flare (refer Figure 3.22). The cross-correlation coefficient between the shock speed and the X-ray flux is ≈ 0.86 (refer Figure 3.23). Furthermore, the maximum in both cases occurred at almost the same time (≈ 03:25:30 UT). Variation of the CME speed in the low corona mimicking the X-ray light curve has been reported in the literature (Zhang *et al.*, 2001; Temmer *et al.*, 2008, 2010; Gopalswamy *et al.*, 2009a). In this work, we find an independent confirmation of this result using the speed variation of the CME-driven shock from radio observations alone for the first time. Considering that there is also good spatio-temporal correlation between the CME LE and the type II burst in the present case (refer Figure 3.21 and the previous paragraph), the time profile of the

shock speed of the latter can be considered to represent the near-Sun kinematics of the CME.

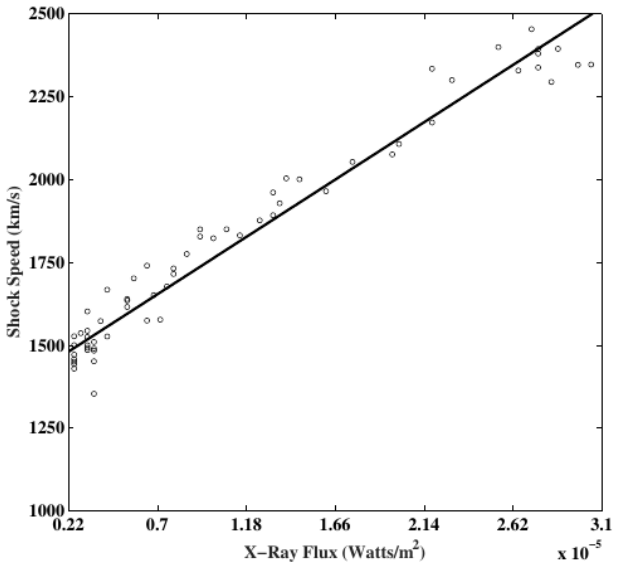

Figure 3.23: Cross-correlation between the type II burst shock speed and the X-ray flare flux in Figure 3.22 . The correlation coefficient is ≈ 0.86.

The fundamental component (f_p) of the start frequency of the type II burst in Figure 3.20 is ≈ 215 MHz as mentioned earlier. This is ≈ 2× higher than the average value of ≈ 100 MHz (fundamental component) for similar "limb" type II bursts (Gopalswamy *et al.*, 2005). Therefore, it is likely that the present CME occurred in a strong field region with fast magnetic reconnection (refer, for example, Lin, Mancuso, and Vourlidas (2006)). An estimate of the coronal magnetic field strength B using the empirical relation $B = \frac{f_p \times dcp}{2.8 \times a(\theta)}$ for harmonic plasma emission (Dulk and Suzuki, 1980) indicates that B ≈ 3 G at a typical frequency like 80 MHz (f_p = 40 MHz) in the present case. Note that $a(\theta)$ is a slowly varying function of the angle θ between the line of sight and direction of the magnetic field in the source region. Its value is ≥ 1 for source regions near the solar limb as in Figure 3.19 (Dulk and McLean, 1978; Ramesh *et al.*, 2010b). We assumed $a(\theta) = 1$ for our calculations. $dcp = \frac{V}{I}$ is the degree of circular polarization. Its estimated value from the Stokes-I and Stokes-V observations of the type II burst in Figure 3.20 is ≈ 0.22 at 80 MHz. Interestingly, the above value of B is equal to that obtained independently using the formula for Alfvén speed, i.e., $v_a = \frac{B}{\sqrt{4\pi M N_e}}$ where $M = 1.9 \times 10^{-24}$ g is the mass ascribed to each electron in the plasma (includes 10% He). We assumed $v_a \approx 1400$ km/s, i.e., the MHD shock speed at 03:31 UT (refer Figure 3.22) when the harmonic component of the type II burst was observed with GRAPH at 80 MHz (refer Figure 3.19). $N_e = 2 \times 10^7 cm^{-3}$ is the electron density corresponding to $f_p = 40$ MHz. The above estimates of B are about 2 × higher than those reported in the literature from type II burst observations

around r $\approx$ 1.5 $R_\odot$ (refer, for example, Gopalswamy *et al.* (2012); Kishore *et al.* (2016)), and 5 $\times$ higher than the active region field strength when there are no type II bursts (refer, for example, Ramesh, Kathiravan, and Narayanan (2011)). This is consistent with our above remark that the CME possibly occurred in a strong field region. The $\approx 2 \times$ higher start frequency of the type II burst compared to the average value reported in the literature is in support of the above argument since $B \propto f_p$. Earlier reports also indicate that B $\approx$ 3 G at r $\approx$ 1.5 $R_\odot$ during a CME or transient radio burst activity is not uncommon (Vršnak *et al.*, 2002; Ramesh *et al.*, 2003, 2013; Sasikumar Raja and Ramesh, 2013).

CMEs associated with solar energetic particle (SEP) events and ground-level enhancement are known to have speeds $\geq$ 2000 km/s, and acceleration $\geq$ 2 km/s^2. The shock formation heights in such events is typically 1.5 $R_\odot$ (Gopalswamy *et al.*, 2013a). Surprisingly, there is no SEP event above the background level in the GOES $\geq$ 10 MeV channel in the present case. The type II burst implies acceleration of $\approx$ 10 keV electrons by the shock. However, there seems to be not enough time for the shock to accelerate ions to sufficiently high energies because the shock had $>$ 2000 km s^{-1} speed only for a couple of minutes (see Figure 3.22). Furthermore, v_a in the source region is high, so the Mach number is low even though the shock speed is high.

Chapter 4
Multiwavelength studies of Type II Bursts

Direct Estimates of the Solar Coronal Magnetic Field Using Contemporaneous Extreme-ultraviolet, Radio, and White-light Observations
Anshu Kumari, R. Ramesh, C. Kathiravan, T. J. Wang and N. Gopalswamy, 2017, **The Astrophysical Journal**, 881, 24.

4.1 Introduction

The formation, evolution, and characteristics of coronal mass ejections, coronal streamers, coronal holes, and coronal loops in the solar atmosphere are primarily determined by the coronal magnetic field. But measurements of the solar coronal magnetic field are presently limited due to practical difficulties (see for e.g., Lin, Penn, and Tomczyk (2000); Tomczyk *et al.* (2008)). It is inferred by extrapolating the observed solar surface magnetic field distribution using the potential or force-free field approximations (see for e.g. Wiegelmann, Petrie, and Riley (2017) for a recent review on the subject). Estimates of the coronal magnetic field strengths, particularly in the 'middle' corona ($r \approx 1.1$ - 3.0 $R_\odot$) are largely obtained using observations of either the circularly polarized radio emission (i.e. the Stokes-V emission) from the transient low frequency ($\lesssim 150$ MHz) radio events like the type I, II, III, IV, and V bursts, or the split-band feature exhibited by some of the radio type II bursts (Smerd, Sheridan, and Stewart, 1975; Dulk and McLean, 1978; Dulk and Suzuki, 1980; Gopalswamy *et al.*, 1986; Bastian *et al.*, 2001; Vršnak *et al.*, 2002; Mancuso *et al.*, 2003; Mancuso and Garzelli, 2013b; Ramesh *et al.*, 2003; Ramesh, Kathiravan, and Satya Narayanan, 2004; Ramesh, Kathiravan, and Narayanan, 2011; Ramesh *et al.*, 2013; Cho *et al.*, 2007; Zimovets *et al.*, 2012; Sasikumar Raja and Ramesh, 2013; Sasikumar Raja *et al.*, 2014; Tun and Vourlidas, 2013; Hariharan *et al.*, 2014; Zucca *et al.*, 2014b; Kishore *et al.*, 2016, 2017). Weak circularly polarized component in the thermal radio emission from discrete sources at low frequencies (Sastry, 2009; Ramesh *et al.*, 2010b), and geometrical

properties of the propagating disturbances observed in EUV images of the solar atmosphere (Gopalswamy *et al.*, 2012) have also been used to estimate coronal magnetic field strength. Kwon *et al.* (2013a) carried out global coronal seismology from the propagation speed of a fast magtenosonic wave to determine $B(r)$ in the extended corona. Despite all these different measurements, a combined estimate of $B(r)$ using observations in the different regions of the electromagnetic spectrum and particularly close to the Sun are very limited (Dulk and McLean, 1978; Vršnak *et al.*, 2002; Mancuso *et al.*, 2003; Cho *et al.*, 2007; Zimovets *et al.*, 2012; Zucca *et al.*, 2014b; Kumari *et al.*, 2017a). Equally rare are reports where the same set of observations are used to independently derive the coronal electron density ($N_e(r)$) required to estimate $B(r)$. This is important since $B(r)$ will otherwise be sensitive to the density model used (see for e.g., Vršnak *et al.* (2002)).

In this chapter, the simultaneous imaging and spectro-polarimetric observations of a type II radio burst with the ground based facilities, and EUV, whitelight observations of the solar corona with instruments onboard space platforms are used to estimate $B(r)$ in the distance range $r \approx 1.1$ - 2.2 $R_\odot$.

4.2 Observations

4.2.1 Radio Observations

The radio observations reported in this chapter were carried out using the different facilities operated in the Gauribidanur observatory[1] (Ramesh, 2011). The *Gauribidanur RAdio Spectro-Polarimeter* (GRASP; Kishore *et al.* (2014); Hariharan, Ramesh, and Kathiravan (2015)) observed a split-band type II radio burst from the Sun on 2016 March 16 during the period $\approx$ 06:45 - 07:00 UT. The frequency range of the burst was $\approx 90 - 50$ MHz. Figure 4.1 shows the dynamic spectra of the burst observed with the GRASP in Stokes-I and Stokes-V. Radio frequency interference in the observations are minimal (Monstein, Ramesh, and Kathiravan, 2007). The estimated peak degree of circular polarization (*dcp*) is in the range $\approx$ 8 - 11%. The duration of the lower (L) and upper (U) bands of the split-band burst at a typical frequency like 88 MHz are $\approx$2.3 min and $\approx$2.5 min, respectively (see Figure 4.2). The half-power width of the response pattern of GRASP is $\approx 90^o \times 60^o$ (right ascension, R.A. $\times$ declination, decl.) and is nearly independent of frequency. The primary receiving element used in GRASP is a Crossed polarized Log-Periodic Dipole. The integration time is $\approx$250 msec, and the observing bandwidth is $\approx$1 MHz at each frequency. The antenna and the receiver systems were calibrated by carrying out observations of the Galactic center as described in the previous chapters. The burst was observed elsewhere also[2] including the *Gauribidanur Radio Interferometer Polarimeter* (GRIP; Ramesh *et al.* (2008)), the Gauribidanur

[1] https://www.iiap.res.in/?q=centers/radio
[2] ftp://ftp.swpc.noaa.gov/pub/warehouse/2016/

LOw-frequency Solar Spectrograph (GLOSS) and e-Callisto (Benz *et al.*, 2009) in Gauribidanur[3] and Ooty[4]. It was associated with a C2.2 class soft X-ray (SXR) flare observed with the Geostationary Operational Environmental Satellite (GOES-15) from the NOAA sunspot active region AR12522 located at the heliographic coordinates N12W83[5]. The above flare was present in the time interval ≈ 06:34 - 06:57 UT, with peak at ≈ 06:46 UT. The location of the split-band burst in the solar atmosphere was inferred from observations with the GRAPH at 80 and 53.3 MHz (see Figure 4.5). We would like to add here that both the type II bursts shown in Figure 4.1 correspond to the lower (L) band of the split-band type II burst in Figure 4.1.

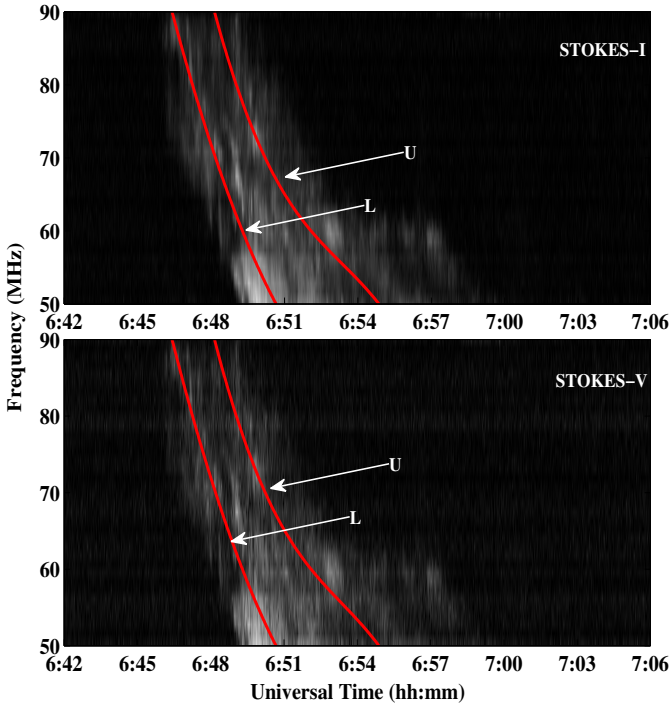

Figure 4.1: Dynamic spectra of the split-band type II radio burst observed with the GRASP on 2016 March 16 during the time interval ≈06:45 - 07:00 UT. The top and bottom panels correspond to Stokes-I and Stokes-V observations, respectively. The 'red' lines indicate the lower (L) and upper (U) bands of the burst.

4.2.2 Optical Observations

The optical data were obtained in EUV at 211 Å with the AIA onboard SDO, and in whitelight with the COR1 coronoagraph of the SECCHI onboard the STEREO[6] and the LASCO on board the SOHO. The STEREO-A/COR1 instrument observed

[3] http://soleil.i4ds.ch/solarradio/qkl/2016/03/16/GAURI_20160316_064459_59.fit.gz.png
[4] http://soleil.i4ds.ch/solarradio/qkl/2016/03/16/OOTY_20160316_064443_59.fit.gz.png
[5] https://www.solarmonitor.org/index.php?date=20160316
[6] https://cor1.gsfc.nasa.gov/

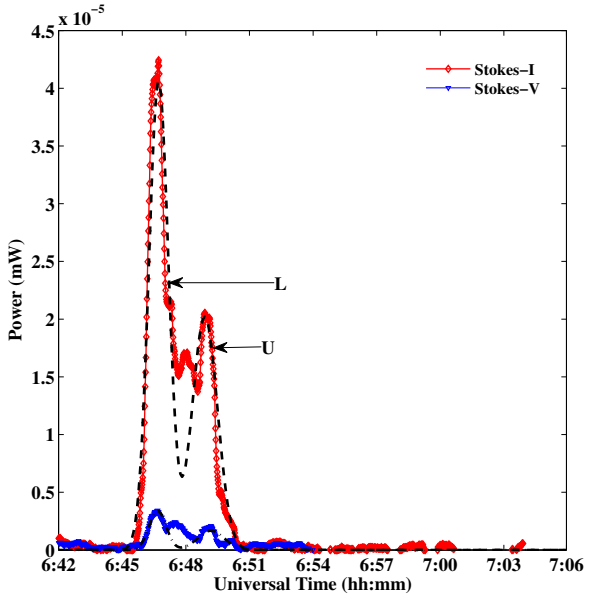

Figure 4.2: Temporal profile of the split-band type II burst in Figure 4.1 at 88 MHz, averaged over a bandwidth of ≈ 4 MHz. The 'dotted' lines represent Gaussian fits to the observed profiles.

a CME around the same time as the type II burst in Figure 4.1. The CME was first seen in the STEREO-A/COR1 FOV at ≈ 06:50 UT and was noticeable till ≈ 07:05 UT (see Figure 4.3). The projected heliocentric distance of the centroid of the CME (r_{CME}) during its first appearance was 1.66 $R_\odot$. The angular width of the CME is ≈36°. The source region for this CME is the active region AR12522 (N12W83) mentioned in Section 2.1. STEREO-A was at ≈E163° during the onset of the CME[7]. The location of the active region therefore corresponds to ≈24^o behind the limb for the STEREO-A view.

The de-projected heliocentric distances of the CME were calculated for STEREO-A/COR1 images by assuming that the projection effects vary as $1/\cos(\phi)$, where ϕ is the angle from the plane-of-sky (POS) and is equal to ≈ 24^o in the present case (see Table 4.1 for the de-projected r_{CME} at different epochs). Figure 4.4 shows SDO/AIA 211 Å observations of activity in the source region of the above CME. The evolution of a flux rope (marked with blue line) and a diffuse shock ahead of it (marked with yellow line), as described in Gopalswamy *et al.* (2012), can be clearly noticed. The leading edge (LE) of the flux rope (r_{fl}) and the shock (r_{sh}) are located at ≈ 1.06 $R_\odot$ and ≈ 1.13 $R_\odot$, respectively, at ≈06:36:36 UT. The values of r_{fl}, r_{sh}, and the radius of curvature (r_c) of the flux rope at different epochs are listed in Table 4.2. Figure 4.5 shows the SOHO/LASCO-C2 observations of the CME at ≈07:00 UT, along with the SDO/AIA 211 Å and GRAPH observations at epochs earlier to the appearance of the CME in the SOHO/LASCO-C2 FOV.

[7] https://stereo-ssc.nascom.nasa.gov/cgi-bin/make_where_gif

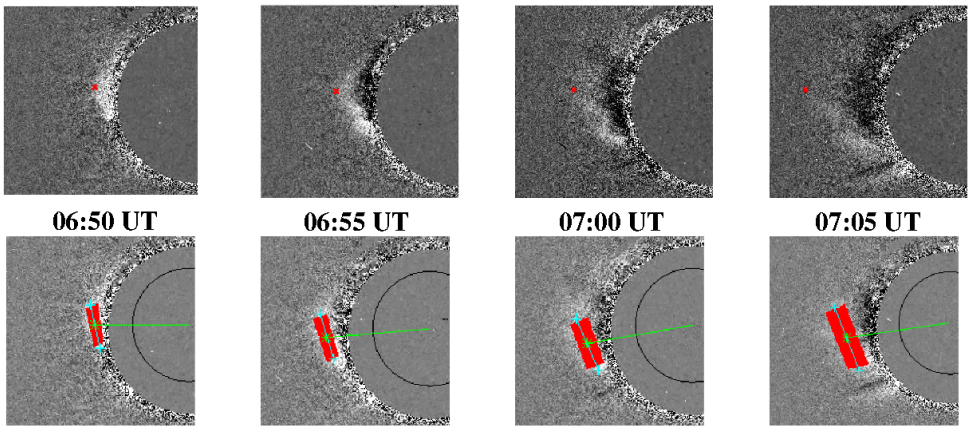

Figure 4.3: Upper panel: STEREO-A/COR1 pB difference images of the CME that was observed on 2016 March 16 between ≈06:50 and ≈ 07:05 UT. The 'red' cross marks indicate the LE of the CME at different epochs. The 'gray' circle represents the coronagraph occulter (radius ≈1.4 $R_\odot$). Lower panel: Same as above but with marking of the CME region (indicated by the red box) used for estimating the densities in Table 4.1. The 'green' asterisk indicates the centroid of the CME, and the 'green' line indicates its heliocentric distance. The 'black' circle indicates the solar limb (radius = 1 $R_\odot$).

It appears that the flux rope structure in EUV, the type II radio burst, and the whitelight CME are all closely associated. Note that the projection effects are very minimal in all the above three observations since AR12522 is almost at the limb of the Sun. We find that the shock is not noticeable in the STEREO-A/COR1 whitelight observations (see Figure 4.3). It is possible that the shock had become fainter by the time the CME reached the STEREO-A/COR1 FOV.

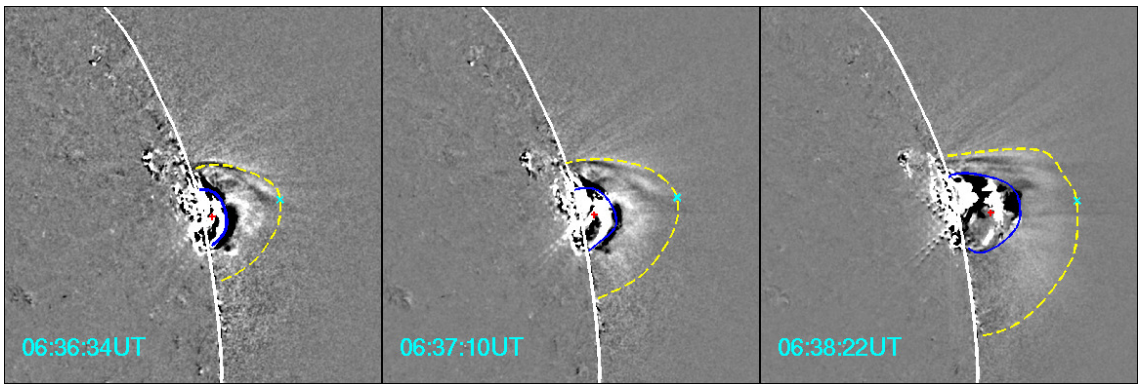

Figure 4.4: Evolution of the flux rope and shock in SDO/AIA 211 Å FOV near the source region of the CME in Figure 4.3. The 'white' line indicates the solar limb (radius = 1 $R_\odot$). The 'blue' and 'yellow' markings indicate the flux rope structure and shock ahead of it, respectively. The 'red' plus marks correspond to the centre of the hemispherical structure (assumed) for the flux rope. The 'cyan' crosses represent the LE of the shock.

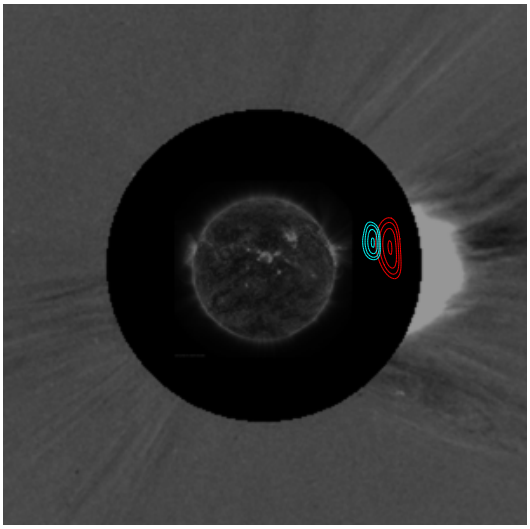

Figure 4.5: Locations of the type II bursts observed with the GRAPH on 2016 March 16 at 80 MHz (≈06:47:15 UT) and 53.3 MHz (≈06:49:48 UT) superposed on the SDO/AIA 211 Å image (≈06:39:36 UT), and SOHO/LASCO-C2 difference image (≈07:00 UT) obtained on the same day. Solar north is straight up and east is to the left. The 'red' and 'cyan' color contours represent the GRAPH observations at 53.3 MHz and 80 MHz, respectively. The peak brightness temperatures (T_b) of the burst are $\approx 2.66 \times 10^8$ K (80 MHz) and $\approx 4.46 \times 10^8$ K (53.3 MHz). The radio contours shown are at 50%, 65%,80% and 99% of the peak T_b. The 'black' circle indicates the occulting disk of the coronagraph. Its radius is ≈ 2.2 $R_\odot$. The bright patch of emission above the coronagraph occulter on its west corresponds to the CME mentioned in the text.

4.3 Analysis and Results

4.3.1 Estimates of coronal electron density (N_e)

4.3.1.1 Radio imaging observations with GRAPH

An inspection of Figure 4.5 indicates that the centroid of the type II burst (r_{radio}) observed with the GRAPH at 80 MHz and 53.3 MHz are located at $\approx 1.6 \pm 0.2$ $R_\odot$ and $\approx 1.9 \pm 0.2$ $R_\odot$, respectively. Any possible error in the position of the burst due to propagation effects such as scattering by density inhomogeneities in the solar corona and/or refraction in the Earth's ionosphere is expected to be within the above error limit as mentioned in the previous chapter. The fact that the Sun is presently in the phase of minimum activity, (during which the observations reported in the present work were carried out) also indicates that the scattering will be less. We calculated N_e at the above two heliocentric distances using the relation $N_e = \left(\frac{f_p}{9\times10^{-3}}\right)^2$, where f_p is the fundamental plasma frequency in units of MHz, and N_e is in units of cm^{-3}. We would like to note here that the type II burst in the present case is mostly due to harmonic plasma emission ($2f_p$) since the locations of the bursts as observed with the GRAPH at 80 MHz and 53.3 MHz

Table 4.1: Density estimates using STEREO-A/COR1 data

Time (UT)	de-projected r_{CME} ($R_\odot$)	Background density ($\times 10^6$ cm^{-3})	CME density ($\times 10^6$ cm^{-3})
06:50	1.82	7.34±1.53	2.71±2.46
06:55	2.00	4.32±0.86	2.35±1.56
07:00	2.06	3.49±0.90	1.66±1.17
07:05	2.24	2.21±0.73	0.95±0.91
1	**2**	**3**	**4**

are above the limb (see Figure 4.5). The consistency of the estimated peak *dcp* of the bursts from the GRASP observations (≈ 8 - 11%, see Section 2.1) with those reported in the literature for harmonic plasma emission also indicate the same (see for example Dulk and Suzuki (1980)). An inspection of the dynamic spectra of the type II burst as observed with the GLOSS indicates the presence of a faint fundamental component of the type II burst at frequencies $\lesssim$ 50 MHz[8]. These confirm that the type II bursts observed with GRASP (Figure 4.1) and GRAPH (Figure 4.5) are due to harmonic emission. So we substituted 40 MHz and 26.7 MHz for f_p in the above relation, and obtained the values of N_e as 1.98×10^7 cm^{-3} at ≈ 1.6 $R_\odot$ (f_p = 40 MHz) and 8.77×10^6 cm^{-3} at ≈ 1.9 $R_\odot$ (f_p = 26.7 MHz).

4.3.1.2 Whitelight observations with STEREO-A/COR1

The pB measurements with the STEREO-A/COR1 were used to estimate the densities before the occurrence of the CME (i.e. the 'background' corona at the location of the CME) and during the CME, at different heliocentric distances. The difference images used for this purpose were obtained using the observations of the CME at ≈ 06:50 UT, 06:55 UT, 07:00 UT and 07:05 UT, and that of the 'undisturbed' background corona at ≈ 06:45 UT (see Figure 4.3). Table 4.1 provides the CME related details obtained from the aforesaid difference images. The de-projected r_{CME} at the above epochs are listed in column 2 of Table 4.1. Note that we had multiplied the measured projected values of r_{CME} by $1/\cos(24^o)$ to remove the projection effects (see Section 2.2). The N_e values of the 'undisturbed' background corona and the CME at the corresponding heliocentric distances are listed in columns 3 and 4 of Table 4.1. The densities were calculated using the spherically symmetrical inversion technique (Wang and Davila, 2014). Note the aforesaid densities correspond to the average density inside the region enclosed by the 'red' box in lower panel of Figure 4.3.

Figure 4.6 shows the plot of the N_e values obtained using GRAPH and STEREO-A/COR1 observations as mentioned above. The error in the density estimates from

[8] https://www.iiap.res.in/gauribidanur/GLOSS-dailyimages/Mar-2016/GBD_DSPEC_20160316.jpeg

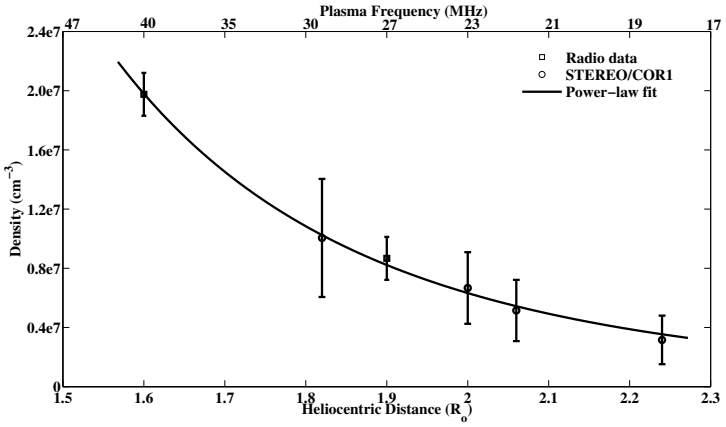

Figure 4.6: Density estimates from radio (GRAPH) and white-light (STEREO-A/COR1) observations. The solid line is a power-law fit ($N_e(r) = 2.3 \times 10^8\, r^{-5.3}$) to the data.

STEREO-A/COR1 is mainly due to the errors associated with the instrumental background subtraction, and the spherically symmetric approximation (Wang and Davila, 2014; Wang *et al.*, 2017). The error in the density estimates from GRAPH is due to variation in N_e over the bandwidth of observations ($\approx$ 2 MHz). The power-law fit to the data indicate that $N_e(r) = 2.3 \times 10^8\, r^{-5.3}$ in the range $r \approx$ 1.6 - 2.2 $R_\odot$. Note that $N_e(r)$ varies typically as r^{-6} in the range $1.1 \lesssim r \lesssim 2.3$ $R_\odot$ (Baumbach, 1937). Considering this, and since we are interested in understanding the characteristics of the CME close to the Sun also using the SDO/AIA 211 Å observations of the associated flux rope structure (see Figure 4.4), we assumed that the above empirical relationship should be valid over $r \approx$ 1.1 - 2.2 $R_\odot$. We find that $N_e(r)$ estimated using the above relation for the SDO/AIA 211 Å observations in Figure 4.4 are reasonably consistent with the $N_e(r)$ values reported by Zucca *et al.* (2014a) in the same distance range ($r \approx$ 1.1 - 1.3 $R_\odot$) utilizing the emission measures derived from SDO/AIA observations for a similar flare associated CME/type II burst event.

4.3.2 Tracing the path of the CME

Figure 4.7 shows the height-time (h-t) plot of the leading edge (LE) of the EUV flux rope structure as observed with SDO/AIA 211 Å, locations of the type II bursts observed with the GRAPH at 80 and 53.3 MHz and GRASP at two different frequencies in the range $\approx$90 - 50 MHz, the LE of the CME in the FOV of the STEREO-A/COR1 coronagraph (see Figure 4.3) and SOHO/LASCO-C2. For the GRASP data in the plot we used two representative frequencies, viz. 82 and 50 MHz (in the lower band L of the harmonic emission, see Figure 4.1). Their heliocentric distances are $r \approx$ 1.58 $R_\odot$ and 1.93 $R_\odot$, respectively. Note that in the case of the GRASP observations, the locations of the type II bursts were estimated using the relationship between f_p and N_e, and the model for $N_e(r)$ derived in Section

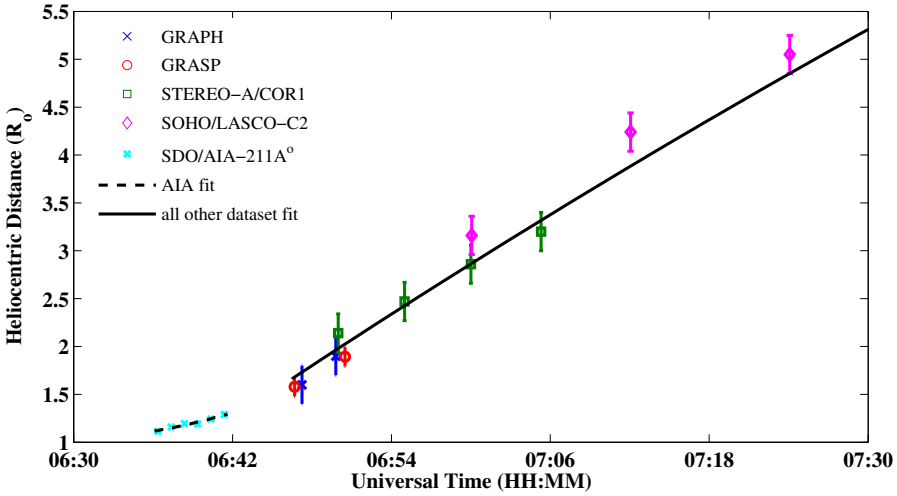

Figure 4.7: Height-time plot of the EUV shock (SDO/AIA 211 Å), type II radio bursts (GRAPH and GRASP), and the whitelight CME (STEREO-A/COR1 and SOHO/LASCO-C2). The 'dashed' black line is a quadratic fit to SDO/AIA 211 Å data, and the 'solid' black line is a quadratic fit to the GRAPH, GRASP, STEREO-A/COR1 and SOHO/LASCO-C2 data.

3.1. The SDO/AIA 211 Å values are limited to less than $r \approx 1.23$ $R_\odot$ and radio cum whitelight values are available only beyond $r \approx 1.58$ $R_\odot$. So we used two separate quadratic fits for the h-t data in Figure 4.7: one for the former with an acceleration of ≈ 1259 m/s^2, and the other for the latter with an acceleration of ≈ -46 m/s^2. The comparatively large acceleration in the SDO/AIA 211 Å FOV was during the onset-peak phase of the associated GOES/SXR flare (see Section 2.1). This is consistent with earlier reports of acceleration of the flux rope structure in the SDO/AIA observations during the impulsive phase of the flare (see for example Zhang, Cheng, and Ding (2012)). The decrease in acceleration in the present case is during the decay phase of the flare. We find that there is reasonable consistency between the two quadratic fits in Figure 4.7. This is expected since the early signature of a CME close to the Sun is usually an expanding flux rope structure (Pomoell, Vainio, and Pohjolainen, 2009; Ma *et al.*, 2011; Patsourakos and Vourlidas, 2012; Gopalswamy *et al.*, 2012, 2013a; Cho *et al.*, 2013), and CME driven magnetohydrodynamic (MHD) shocks generate type II bursts in the solar atmosphere (Mann, Classen, and Aurass, 1995; Aurass, 1997; Claßen and Aurass, 2002; Gopalswamy, 2006a; Cho *et al.*, 2008; Vršnak and Cliver, 2008; Gopalswamy *et al.*, 2009b; Ramesh *et al.*, 2010a, 2012; Kumari *et al.*, 2017b). An estimate of the linear speed of the CME LE from the whitelight data (STEREO-A/COR1 and SOHO/LASCO-C2) in the range $r \approx 2.0$-$5.0\,R_\odot$ (see Figure 4.7) indicates it is $\approx$ 1000 km/s. The estimated shock speed ($v_s = v_a \times M_a$, where v_a is the Alfv́en speed and M_a is the Mach number) for the type II burst is $\approx$ 825 km/s (see Table 4.3). This is in good agreement with the speed of the CME LE. Note that though a shock was observed in the SDO/AIA 211 Å FOV, no type II burst was observed

Table 4.2: Estimates of B and the related parameters from SDO/AIA 211 Å observations

Time (UT)	r_{sh} ($R_\odot$)	r_{fl} ($R_\odot$)	r_c ($R_\odot$)	Δr ($R_\odot$)	δ	M_a	v_a (km/s)	B (G)
06:36:34	1.12	1.04	0.025	0.083	3.35	1.12	–	–
06:37:10	1.15	1.06	0.035	0.090	2.59	1.15	401	1.93
06:37:46	1.17	1.08	0.040	0.101	2.50	1.16	400	1.83
06:38:22	1.19	1.10	0.046	0.095	2.06	1.19	390	1.74
1	**2**	**3**	**4**	**5**	**6**	**7**	**8**	**9**

at that time. One likely reason for the absence of the type II burst could be the smaller values of M_a associated with the above shock (see Table 4.2). According to Mann *et al.* (2003); Warmuth and Mann (2005), M_a should well exceed unity ($\gtrsim 1.4$) for the occurrence of type II burst.

4.3.3 Estimates of the coronal magnetic field strength (B)

Our aim is to directly estimate B using the observed data and with minimal assumptions. The target distance range is $r < 2.3$ $R_\odot$ (see Figure 4.6). We used the following theoretical relation for that:

$$B = \frac{v_a \times \sqrt{N_e}}{2.18 \times 10^6} \tag{4.1}$$

where B is in units of G. We used the empirical relationship in Section 3.1 to obtain $N_e(r)$. The estimated values are in the range $\approx 1.39 \times 10^8$ - $3.6 \times 10^6 \mathrm{cm}^{-3}$ over $r \approx 1.10$ - 2.20 $R_\odot$, the combined distance range of the SDO/AIA 211Å and radio observations in the present case. M_a was estimated independently for the aforementioned two observations since they correspond to different heliocentric distance ranges.

4.3.3.1 SDO/AIA 211 Å observations

Figure 4.4 shows the initial stages of the CME formation in the SDO/AIA 211 Å FOV in the present case. Figure 4.8 shows the location of the CME flux rope and shock at ≈06:36:36 UT. Note that some of the values from the leading edge method may be just the height of the flux rope because the shock is not distinctly seen in the images. Measuring the locations and characteristics of the corresponding structures, i.e. the flux rope and the shock ahead of it, at different epochs help to calculate M_a using the relation (see for example Gopalswamy *et al.* (2012); Veronig *et al.* (2010)),

$$M_a = \sqrt{1 + [1.24\delta - (\gamma - 1)/(\gamma + 1)]^{-1}} \tag{4.2}$$

where δ is the relative stand-off distance and γ is the adiabatic constant. The heliocentric distance of the shock (r_{sh}), LE of the CME flux rope (r_{fl}), thickness

of the shock $\Delta r = r_{sh} - r_{fl}$, and radius of curvature (r_c) of the CME flux rope are used to calculate δ ($=\frac{\Delta r}{r_c}$). γ was assumed to be 4/3 for the present calculations (see Kumari *et al.* (2017c) for details). The different values estimated using Figure 4.4 are listed in columns 2-6 of Table 4.2. We then calculated v_s for the adjacent time intervals in column 1 using the values of r_{sh} in column 2. Finally, v_a values in column 8 were obtained using the relation $v_a = v_s/M_a$. We find that the location of the active region in the present work and that of the event reported in Gopalswamy *et al.* (2012) are nearly the same ($\approx$ W84). Furthermore, the v_a values ($\approx 400 - 500$ km/s) and the angular width of the CME ($\approx 36^o$) are also reasonably close in the two cases. So, assuming 06:36:34 UT as the first appearance time (i.e. $t = 0$ of the flux rope and the shock in Figure 4.4), we independently calculated the corresponding r_{sh}, r_{fl}, and r_c values as a function of time using the empirical equations mentioned in Figures 3a and 3b of Gopalswamy *et al.* (2012). The constants in the aforementioned equations were replaced by the values of r_{sh}, r_{fl}, and r_c at 06:36:34 UT (see Table 4.2). Interestingly, the empirically calculated values agree well with the direct estimates.

4.3.3.2 Radio spectral observations with GRASP

For the radio observations, M_a was calculated using the following equation (Smerd, Sheridan, and Stewart, 1974; Mann, Classen, and Aurass, 1995; Vršnak *et al.*, 2002),

$$M_a = \sqrt{\frac{X(X+5)}{2(4-X)}} \tag{4.3}$$

where X is density jump across the shock during the type II burst. The density jump is calculated from the instantaneous bandwidth (BDW) of the burst, i.e. $\mathrm{BDW} = \frac{\mathrm{F_U} - \mathrm{F_L}}{\mathrm{F_L}}$ and $\mathrm{X} = (\mathrm{BDW}+1)^2$. $\mathrm{F_U}$ and $\mathrm{F_L}$ are the upper and lower frequency components of the type II burst in the dynamic spectra. To estimate the B values, $\mathrm{F_L}$ is used as it corresponds to the 'undisturbed' corona. Table 4.3 lists the different values estimated from the type II burst observations in Figure 4.1. The v_a values in column 8 were obtained in the same manner as the SDO/AIA 211 Å case described in Section 3.3.1, but equation (3) was used for the calculations of M_a.

4.3.3.3 The radial variation of the coronal magnetic field strength

Figure 4.8 shows the B values estimated using the SDO/AIA 211 Å and GRASP observations. The respective estimates are consistent with each other though they correspond to two different heliocentric distance ranges. A single power-law fit of the form $B(r) = 2.61 \times r^{-2.21}$ describes the distribution. The only available two-dimensional magnetic field map obtained using coronal Zeeman magnetometry and full-Stokes spectropolarimetric measurements indicate that $B \approx 3.6$ G at $r \approx 1.1$ $\mathrm{R_\odot}$ (Lin, Kuhn, and Coulter, 2004). Compared to this, the present results predict

Table 4.3: Estimates of B and the related parameters from GRASP observations

Time (UT)	F_U (MHz)	F_L (MHz)	BDW	X	M_a	R ($R_\odot$)	v_a (km/s)	B (G)
06:47:10	102.44	81.89	0.25	1.56	1.45	1.58	579	1.21
06:48:02	91.12	72.37	0.26	1.59	1.47	1.65	571	1.06
06:49:28	79.51	57.48	0.38	1.91	1.78	1.86	472	0.69
06:51:00	65.82	47.65	0.38	1.91	1.77	1.99	473	0.58
06:53:35	54.50	40.21	0.36	1.84	1.70	2.12	493	0.51
06:57:00	45.57	35.74	0.27	1.63	1.51	2.15	558	0.50
1	**2**	**3**	**4**	**5**	**6**	**7**	**8**	**9**

Table 4.4: Estimates of B from the *dcp* of the harmonic plasma emission

Observed frequency (MHz)	Plasma frequency (MHz)	dcp %	B (G)
51.0	25.5	9.4	0.61
61.0	30.5	10.3	0.80
71.0	35.5	9.8	0.89
81.0	40.5	9.3	0.98
1	**2**	**3**	**4**

$B \approx 2.1$ G at the same distance. The M_a values calculated using equations 4.2 and 4.3 vary over the range $\approx$1.17 - 1.22 and $\approx$1.45 - 1.78 in the distance interval $r \approx$1.13 - 1.23 $R_\odot$ (SDO/AIA 211 Å) and $r \approx$1.4 - 2.2 $R_\odot$ (radio), respectively (see column 7 in Table 4.2 and column 6 in Table 4.3). We used the empirical relationship in Section 3.1 to obtain $N_e(r)$ over $r \approx$1.10 - 2.20 $R_\odot$. The estimated values are in the range $\approx 1.73 \times 10^8$ - $1.38 \times 10^7 \mathrm{cm}^{-3}$.

In the case of harmonic type III radio bursts, the observed polarization is invariably in the ordinary mode (magneto-ionic 'o' mode). The associated Langmuir waves are nearly one-dimensional, i.e. confined to small range of angles ($\theta \leq 20°$) to the magnetic field (Melrose, Dulk, and Smerd, 1978; Melrose, Dulk, and Gary, 1980; Dulk and Suzuki, 1980). Note the Langmuir waves responsible for type II bursts are produced in situ ahead of a propagating coronal shock (by the electron beams accelerated at the shock) unlike the type III bursts which are due to electrons accelerated in the low corona. But there is evidence that the Langmuir waves in the two types of bursts are similar. Furthermore, the Langmuir waves are one-dimensional and field-aligned in harmonic type II bursts also (see for example Graham and Cairns (2015)). So, we independently calculated B from the GRASP observations using the relation between *dcp* and B for harmonic plasma emission polarized in the 'o' mode (Melrose, Dulk, and Smerd, 1978; Melrose, Dulk, and

Gary, 1980; Dulk and Suzuki, 1980), i.e.

$$B = \frac{dcp \times f_p}{2.8 \times a(\theta, \theta_o)} \tag{4.4}$$

to compare with the split-band technique estimates of B from the same GRASP

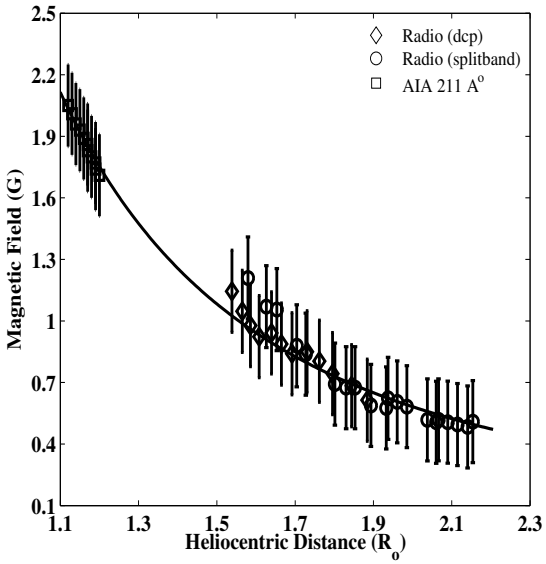

Figure 4.8: Estimates of B from SDO/AIA 211 Å and radio observations. The 'solid' black line is a power-law fit ($B = 2.61 \times r^{-2.21}$) to the data points.

observations. Here $a(\theta, \theta_o)$ is a slowly varying function of the viewing angle (θ) and the half-angle (θ_o) of the cone in which the Langmuir wave vectors are confined. f_p is the fundamental plasma frequency as mentioned in Section 3.1.1. In the present case, the heliographic longitude of the active region associated with the type II radio burst is W83. This implies that $\theta \approx 83°$. In the case of θ_o, we assumed it to be the same as the angular width of the type II burst source size. Since the observed size of any radio source is in general the convolution of instrument 'beam' size and the 'true' size of the radio source, we estimated the latter for the type II bursts in the present case at 53.3 and 80 MHz by subtracting the respective instrument 'beam' sizes from the corresponding observed source sizes (see for example Aubier, Leblanc, and Boischot (1971)). An inspection of Figure 4.5 indicates that the half-power size of the type II bursts at 53.3 and 80 MHz estimated as mentioned above are located within an angle $\approx 15°$ with respect to the magnetic field direction from the associated active region. So we assumed $\theta_o \approx 15°$. This is approximately the same as the angular spread of similar Langmuir waves in the case of type III radio bursts (see for example Ratcliffe, Kontar, and Reid (2014)). This was independently verified the values of θ_o from the B values obtained with splitband technique and found that it is reasonably close to $\theta_o = 19°$.

The above two values of θ and θ_o indicate that $a(\theta, \theta_o) \approx 1.4$ in the present case (Melrose, Dulk, and Gary, 1980). The estimated peak *dcp* from the GRASP observations (90 - 50 MHz) is in the range $\approx$ 8 - 11%. Substituting f_p = 45 - 25 MHz in equation 4.4, we then estimated B. Figure 4.8 shows the combined plot of B values obtained using the SDO/AIA 211 Å and radio observations (split-band and harmonic plasma emission techniques) in the distance range $r \approx 1.1$ - 2.2 $R_\odot$. There is good agreement between the estimates of B using the aforementioned two different radio techniques. Further, a single power law $B = 2.61 \times r^{-2.21}$ describes the estimates of B from the SDO/AIA 211 Å and the radio observations.

Chapter 5
Type III Bursts with LOFAR

5.1 Introduction

Transient radio emission from the Sun at different frequencies originate at different levels on the solar atmosphere (McLean and Labrum, 1985a). Radiation in the height range of 1.5 $R_\odot$ to 4.0 $R_\odot$ (where, $R_\odot$ is the radius of the optical Sun) (Lin, Kuhn, and Coulter, 2004), which falls in the frequency range of 100 - 10 MHz (Newkirk, 1961; McLean and Labrum, 1985a), is significant because most transient events that impact the solar terrestrial relations occur in the above height range (Benz, 1994). Most of these transient events are driven by the ambient magnetic field (Spangler, 2005). The orthogonal components of the emitted radiation, when traversing the solar corona - which is a plasma medium - in the presence of a magnetic field, are retarded differently due to the birefringent nature of the corona. The polarization of the resultant emission (Melrose and Sy, 1972) depends on the strength of the magnetic field. Thus, studying the nature of the polarized radiation from the corona provides a direct access to the ambient solar magnetic field strengths (McLean and Labrum, 1985a). Since these transient events originate at different layers on the corona almost simultaneously, broad-band spectro-polarimetry is a powerful method to probe the magnetic field variation.

One of the most common radio signature of any flicker on the Sun is a solar type III burst (Reid and Kontar, 2018). Type III bursts are the fast drifting structures in the solar dynamic spectra, which occurs when the electrons are accelerated along the open magnetic filed lines in the solar atmosphere. These radio bursts give information regarding electron acceleration along magnetic field lines in the middle corona as well as near-Earth region, which can not be studied currently in any other wavelengths. These bursts can be used to study the structure of the open coronal magnetic lines field (B) in the middle corona.

The details of the observations are described in Section 5.2. In Section 5.3, the data analysis of the tied array and interferometric observations are explained. The results obtained are written in Section 5.4.

5.2 Observations

On March 30, 2018, there was a weak X-ray flare at active region (AR) 22703[1], and the enhancement in X-ray flux was recorded with Geostationary Operational Environmental Satellite system (*GOES*[2]) during 13:20 - 13:45 UT. This was a B2.1 class flare which had its rise phase between 13:20 and 13:24 UT and the decay phase between 13:30 and 13:45 UT. The peak time of this B2.1 class was during 13:24 and 13:30 UT with a slight decrease in flux around 03:26 UT. The radio signatures of this flare were seen with various solar spectrographs worldwide, eg. e-CALLISTO[3], LOFAR, etc. LOFAR[4] is a large radio telescope network in the Netherlands and countries in Europe for astronomical observations at radio-frequencies below 250 MHz. It is operated by ASTRON, the Netherlands Institute for Radio Astronomy and its international partners. It uses array of omni-directional antennas. Figure 5.1a shows the enhancement in the X-ray flux during the flare and the corresponding radio bursts as seen with e-CALLISTO spectra. The same bursts were observed with LOFAR core stations in both tied-array beam and interferometric mode.

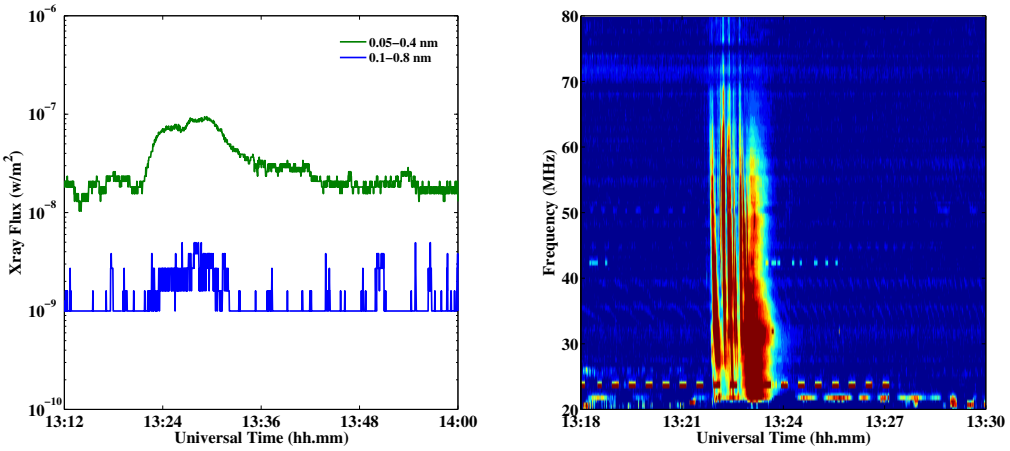

(a) (b)

Figure 5.1: (a) X-ray light curve for the B 2.1 class flare during 13:20 – 13:45 UT (data courtesy: GOES-15). (b) Type III and type V bursts recorded with e-CALLISTO BLEN station during 13:22 – 13:24 UT. The bursts have their extent from 80 - 20 MHz.

5.2.1 Tied-Array Beam Observations

A tied-array beam is formed by coherently combining all the station beams, one for each station (van Haarlem *et al.*, 2013). The bursts shown in Figure 5.1b were observed in all the four Stokes channels with tied-array beam observations with

[1] ftp://ftp.swpc.noaa.gov/pub/indices/events/20180330events.txt
[2] https://satdat.ngdc.noaa.gov/sem/goes/data/new_full/2018/03/goes15/csv/
[3] http://soleil.i4ds.ch/solarradio/callistoQuicklooks/?date=20180330
[4] http://www.lofar.org/

LOFAR core stations. The radio bursts were recorded with Low Band Antennas (LBAs), which operates over 90-10 MHz. There were simultaneously 168 beams in the sky, which had a FOV $\approx$ 10 $R_{\odot}$. The range of the full-width half maxima (FWHM) of the beams ranged between $\approx$ 7‘ at 90 MHz to $\approx$ 21‘ at 30 MHz. This observation has a spectral and temporal resolution of $\approx$ 12.5 kHz and $\approx$ 10 ms. The tied-array observations were used to produce the dynamic spectra of the event in all the four Stokes parameters. Figure 5.2 shows the tied-array beams position in the sky.

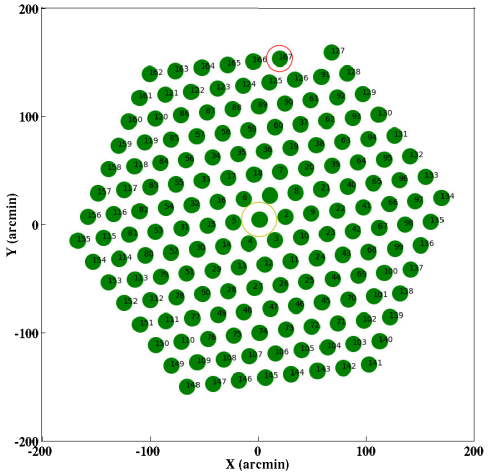

Figure 5.2: Beam positions in the sky for all the 167 beams. The yellow and red circles represents the size of the optical Sun and the beam size at 50 MHz, respectively.

5.2.2 Interferometric Observations

We used interferometric observations for high dynamic, high spatial resolution imaging between 80-20 MHz for the type III bursts observed on March 30, 2018. For this, the core LOFAR stations were used with spectral and temporal resolution of $\approx$ 195 kHz and $\approx$ 160 ms, respectively. The spatial resolution at 80 MHz and 20 MHz were $\approx$ 0.1 deg and $\approx$ 0.4 deg, respectively. This is the first time the aperture synthesis imaging observations for an active Sun using LOFAR has been presented.

5.3 Data Analysis

5.3.1 Spectro-Polarimetric Data Analysis

Tied-array beam observations with LOFAR on March 30, 2018 contained all Stokes observations between 80-20 MHz. For processing the raw data, we have used python script. To remove the Radio Frequency Interference (RFI), we have done pre-event data subtraction as well as a 5×5 median filtering. The cleaned dynamic spectra in the four Stokes channels are shown in figure 5.3.

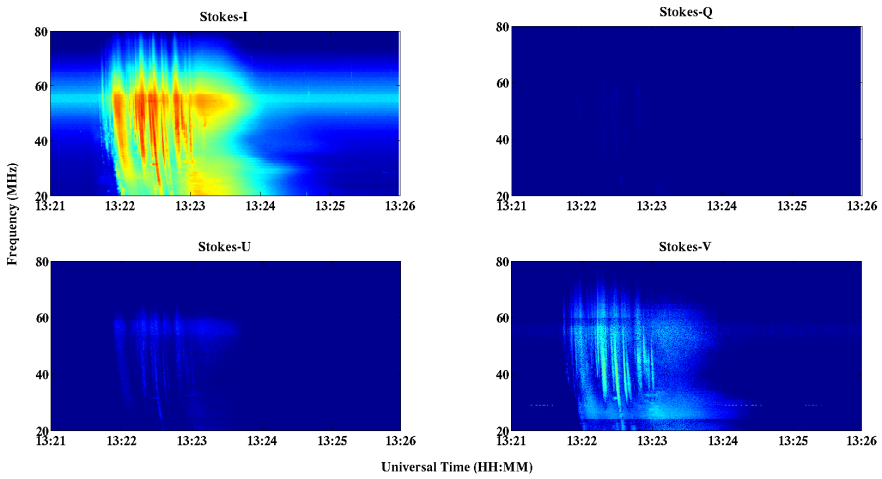

Figure 5.3: Dynamic spectra of the type III bursts on March 30, 2018 in all the Stokes channels.

At our desired frequencies (meter wavelength), because of large distance between the source and the observer, due to very high Faraday rotation, any linearly polarized component would vanish, hence we only expect the emission in total intensity (Stokes-I) and circular polarized intensity (Stokes-V). It is quite obvious from the Figure 5.3, that some residuals emission was also present in Stokes-U channel during the occurrence of type III bursts. Going by the Stokes parameters equations (Stokes-I and Stokes - V), as described below,

$$I =< E_x E_x^* + E_y E_y^* > \tag{5.1}$$

$$V = -i < E_x E_y^* - E_y E_x^* > \tag{5.2}$$

where, E_x and E_y are the electric fields received by the two orthogonal antennas, respectively. Therefore, any signal recorded in Stokes-U channel, which is the real part of the cross-correlation of the signal received by the two orthogonal dipoles, is a leakage from Stokes-V. Hence, to correct the Stokes-V channel, we used expression 5.3,

$$V_{corrected} = \sqrt{V^2 + U^2} \tag{5.3}$$

The processed, cleaned and corrected dynamic spectra in Stokes-I and Stokes-V channels are shown in Figure 5.4. With high spectral and temporal resolution of LOFAR observations (12.5 kHz and 10 ms), we were able to distinguish multiple type III bursts within this group of type III bursts. The broad enhancement mostly at low frequencies after 13:23 UT is type V burst. For our studies, we restricted ourselves to the type III bursts. We selected five strong trails in the dynamic spectra, from 80-20 MHz. The occurrence of these trails at three particular frequencies are shown in Table 5.1.

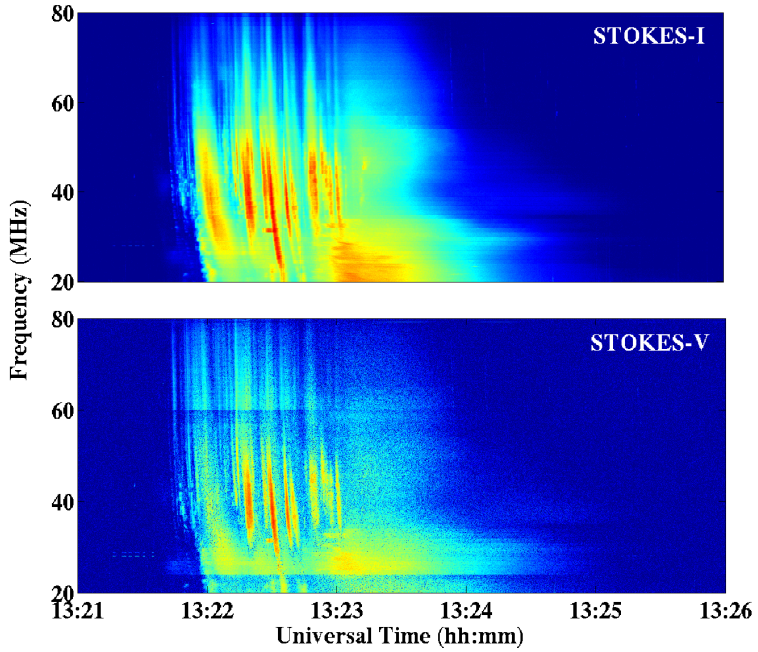

Figure 5.4: Clean and corrected spectra for the type III bursts in Stokes-I and Stokes-V channels.

Table 5.1: Type III trajectories

Trajectory		Frequency	
	20 MHz	50 MHz	80 MHz
		Time (UT)	
1	13:22:10	13:21:50	13:21:47
2	13:22:26	13:22:16	13:22:14
3	13:22:46	13:22:37	13:22:35
4	13:22:51	13:22:46	13:22:45
5	13:22:57	13:22:51	13:22:50

5.3.2 Interferometric Imaging

LOFAR had seamless interferometric observations of the Sun on March 30, 2018 during 12:00 - 16:00, with LBAs between 80 - 20 MHz. We took advantage of the same and produced snapshot synthesis images of the five individual type III trails (refer Table 5.1) in the spectra (refer Figure 5.4). For calibration of the target, we used Taurus sky model (Tau-A)[5], which is a point source to the telescope. The data was processed using New Default Preprocessing Pipeline (NDPPP)[6]. The interferometric snapshots at few time instances and few frequencies are shown in

[5] https://raw.githubusercontent.com/lofar-astron/prefactor/master/skymodels/Ateam_LBA_CC.skymodel

[6] https://www.astron.nl/lofarwiki/doku.php?id=public:user_software:documentation:ndppp

Figure 5.5.

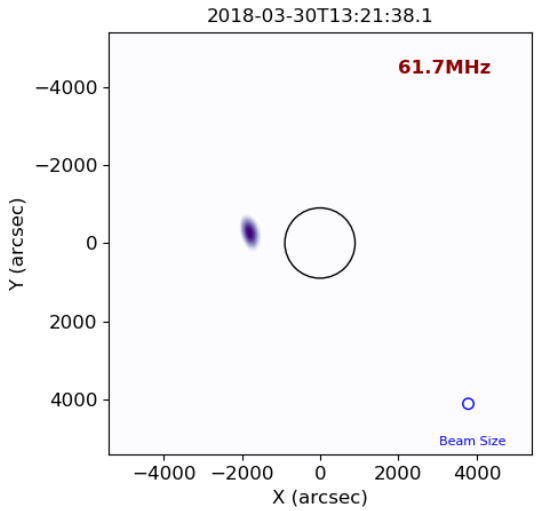

Figure 5.5: Snapshot of the group of type III bursts on March 30, 2018 at 61.7 MHz with LOFAR. The optical limb of the Sun is shown with closed black circle.

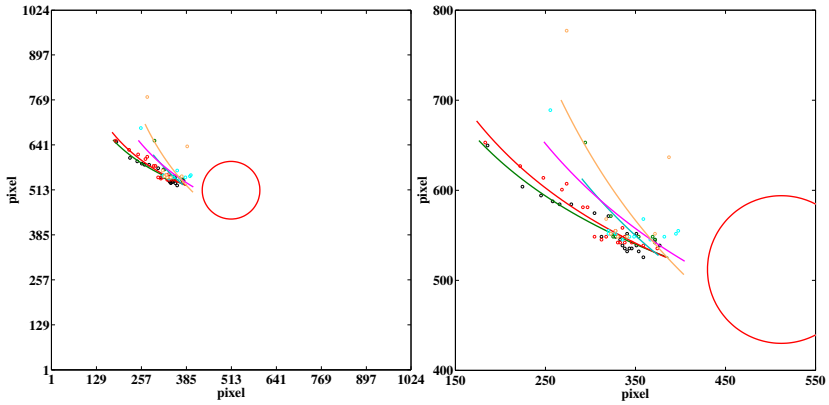

Figure 5.6: Left panel: Trajectories of the electrons gyrating along the open magnetic field lines traced from the individual type III bursts in the dynamic spectra. The closed red color circle represents the optical limb; Right Panel: Zoomed in version of the same figure.

The five trails in the spectra seems to be following five different lanes in the solar maps made with the interferometric observations at various times in different frequency channels. It is well known that type III bursts occurs when the electrons accelerate along the open magnetic fields in the solar atmosphere. Tracing the path of the type III bursts would provide us the information about the structure of the magnetic field along the electron path. Figure 5.6 shows that the five different trails in the spectra corresponds to five different open magnetic field configurations.

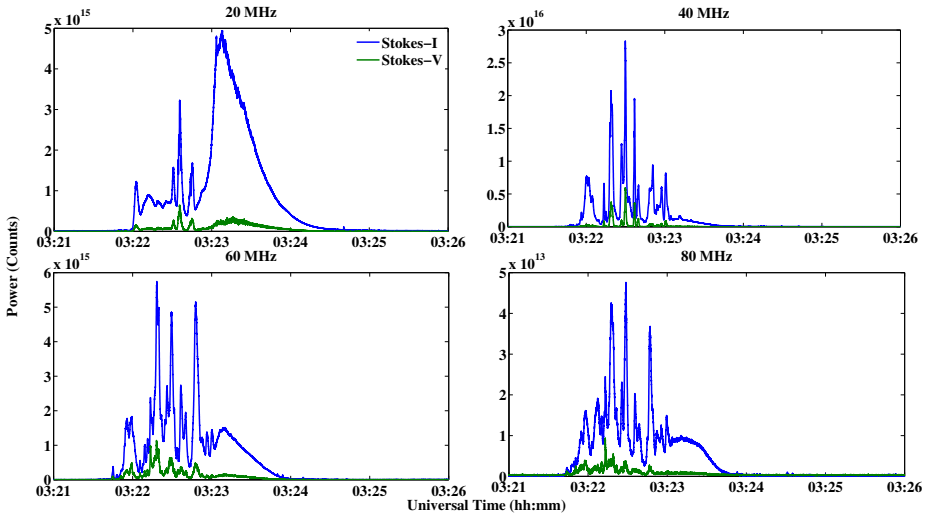

Figure 5.7: Stokes-I and Stokes-V profiles at various frequencies.

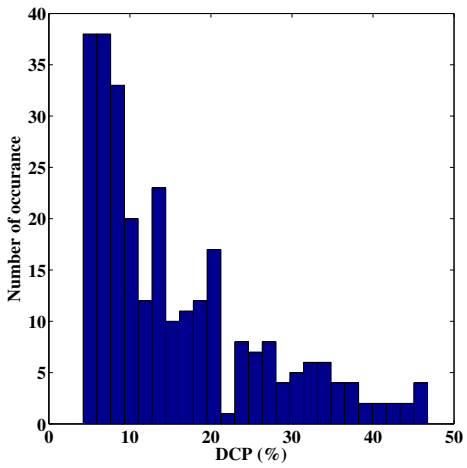

Figure 5.8: Histogram of DCP of the type III bursts.

5.4 Results & Discussions

5.4.1 Density vs Height

One of the advantages of having simultaneous spectral and imaging observations is getting the positional information of the source rather than relying on any existing density models. We calculated the densities at various heliocentric distances for the observed type III bursts between 80 - 20 MHz using $f_p = 9000\sqrt{N_e}$, where f_p & N_e are plasma frequency in MHz and electron number density in cm^{-3}. The obtained density values were compared with the densities obtained with two different methods, i.e. empirical relationship (Zucca *et al.*, 2014a), which is based on the density values obtained with extreme Ultra violet (EUV) and white-light

coronagraph data, and Newkirk's density model, both of which are in agreement with those values derived here. Figure 5.9 shows the comparison between the aforementioned quantities.

5.4.2 Magnetic Field estimates

5.4.2.1 DCP calculations

Direct estimation of coronal magnetic field in the middle corona is presently not available in any other wavelength except radio. By using the properties of radio bursts, B in the middle corona can be calculated. One of the most common way to do so is by using the spectro-polarimetric data. Since the degree of circular polarization (dcp) depends upon the ambient magnetic field, the former can be used to estimate the B fields. Figure 5.7 shows the Stokes-I and Stokes-V temporal profiles during the bursts. The dcp is the ratio of the $\frac{Stokes-V}{Stokes-I}$. The histogram in figure 5.8 shows the variation of dcp. Dulk & Mclean suggested if dcp values are $\leq$ 25 – 30 %, then the emission is second harmonic. Figure 5.8 shows the dcp values for the group of type III bursts are well below 30 % (mostly), we assumed that the type III bursts to be a second harmonic emission.

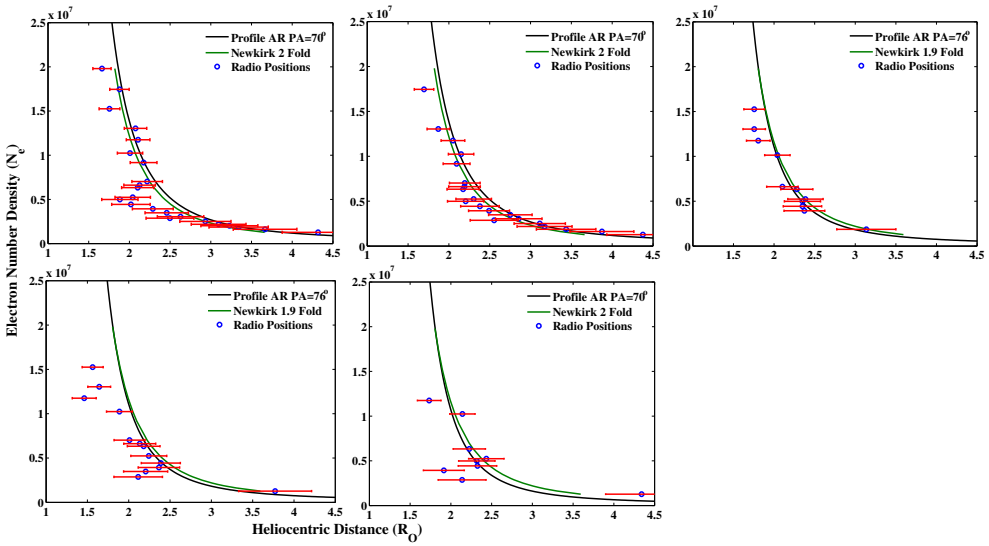

Figure 5.9: Comparison of densities obtained with interferometic imaging (present work), empirical formula and density model.

5.4.2.2 Estimation of B

Melrose(1972) & Dulk (1976) had shown that dcp and plasma frequencies are related and hence by calculating the dcp, we can estimate B along the heliocentric heights. From previous section, it is established that the type III bursts were due to second harmonic plasma emission, so $f_p = f_o$, where f_p and f_o are plasma and observed frequency, respectively. We used expression 5.4:

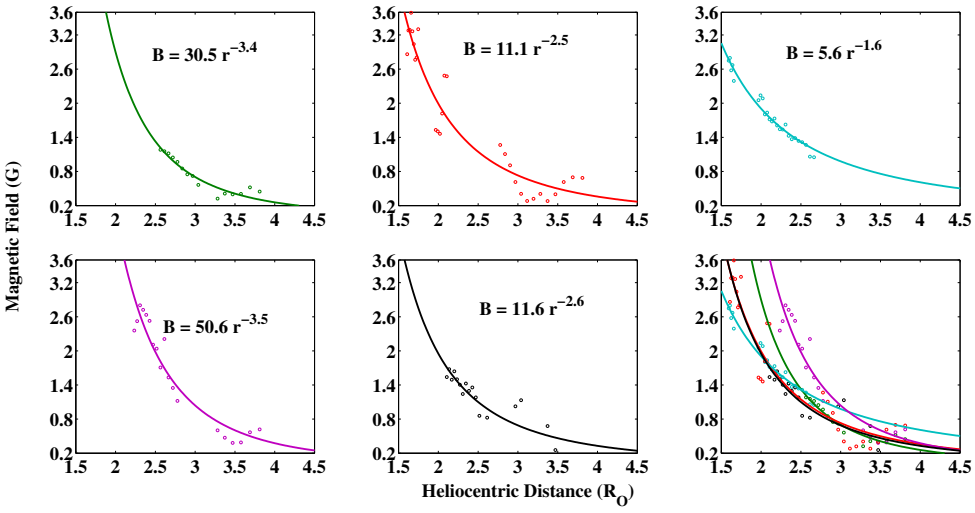

Figure 5.10: Magnetic field distribution for the five different trails of type III bursts in the dynamic spectra. The bottom right panel shows all the B distributions combined.

$$B = \frac{f_p \times dcp}{2.8 \times a(\theta)}[G] \tag{5.4}$$

where, B is the magnetic field in Gauss, and f_p is plasma frequency in MHz and $a(\theta)$ is a function of viewing angle and extent of Langmuir waves on the solar atmosphere.

We calculated the B values for all the five trails in the spectra and individual power law expressions were fit to the values (refer Figure 5.10). The different power law indices (1.6 - 3.4) indicates that the emission is coming from different magnetic field lines.

Chapter 6
Conclusion

6.1 Summary

6.1.1 Instrumentation

The prime focus of this thesis work is to design and develop a spectro-polarimeter with wideband, high sensitive, and high spectro-temporal resolution to observe the Sun at low radio frequencies at the Gauribidanur Radio Observatory. During the PhD tenure, the observing capabilities of existing Gauribidanur RAdio Spectro-Polarimter (GRASP; Kishore *et al.*, 2015) instrument were improved. The old GRASP worked between 35 - 85 MHz with a spectrum analyzer (SA) based back-end[1]. SA works on sweep mode, which uses the superheterodyne principle. The latter down-converts the observing frequency band by mixing a Local oscillator (LO) signal for recording the data. The shortcoming of this system is that it takes up to 4 ms to sweep through the observing band and takes $\sim$ 240 ms to write the data. It does not take any observations while writing the data. Therefore, we tend to lose short lived bursts. Also, the signal to noise ratio (SNR) in any system is directly proportional to the number of signals/spectra averaged. In the SA based system, for solar observations, about 2-10 spectra are averaged on-board in order to reduce the loss of data during the observation. But, the new GRASP contains two spectro-polarimeters : (1) Two mutually orthogonal LPDAs that can operate in the 15 - 85 MHz and are separated by 10 m apart; (2) a cross-polarized LPDA (CLPDA) that can operate in the 50 - 500 MHz range.

The spectral and temporal resolution are improved by a factor of 10 and 3, respectively with the new instrument. The improved spectral resolution over the SA based system is due to the excess data acquired during the writing period of the SA. The old GRASP observed the Sun between 35 and 85 MHz ; But now the observations are carried out between 15 and 500 MHz. The noise level is reduced

[1] https://www.keysight.com/en/pcx-x2015002/spectrum-analyzers-signal-analyzers?cc=IN&lc=eng

drastically and that gave rise to an improved SNR by $\sim$ 18 dB. The dynamic range (DR) is improved by $\sim$ 48 dB. So, the telescope's capabilities are improved overall and it can now detect weak bursts which were previously buried under the background noise level. The ROACH-based digital correlators would also help in the ongoing augmentation of GRAPH for multi-frequency observations. The spectro-polarimeteric correlator could be an initial step to image the Sun in Stokes-V using GRAPH. High resolution instrumentation for solar spectral observations is expected to provide insights into electron acceleration along different types of magnetic field lines in the corona, the effect of inhomogeneities due to turbulence, etc. and their relation to radio emission. Figure 6.1 shows **a few** radio bursts recorded with the improved spectro-polarimeter in both total intensity and circular polarized intensity.

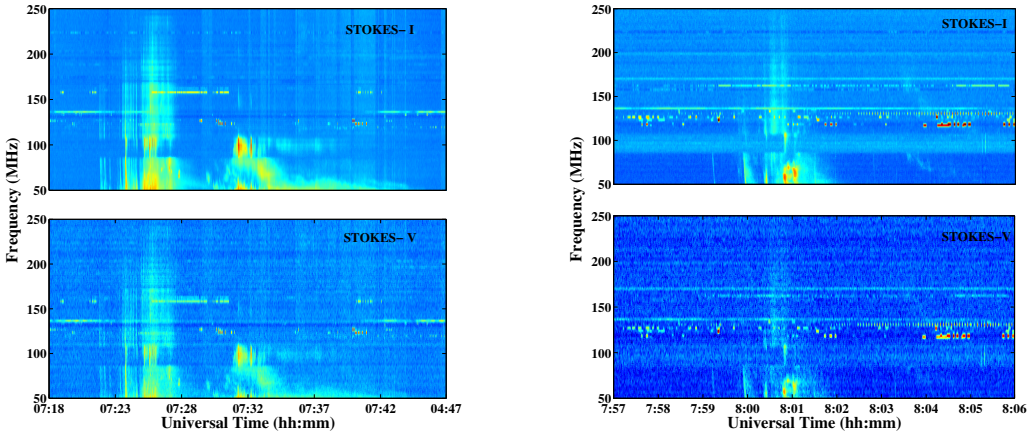

(a) **(b)**

Figure 6.1: The spectra obtained with the new spectro-polarimeter: (a) Stoke-I and Stokes-V profiles of type III and type II bursts observed with GRAPH on 12 Sep, 2017; (b) Solar dynamic spectra of a type V burst on 30 Mar, 2018.

6.1.2 Science Results

The new spectro-polarimeter instruments are currently being operated at the observatory and observations of the Sun are carried out regularly. The data analysis pipelines were developed in MATLAB and Python and about 50 bursts were detected so far. **A few** type II bursts were studied in detail by combining observations in whitelight, EUV and X-ray (Kumari *et al.*, 2017b,c, 2019a).

By using various methods for radio, EUV and whitelight observations, coronal magnetic fields were estimated and compared. A new technique was developed recently to estimate the coronal magnetic field strength using the geometrical properties of a CME/ EUV wavefront (Gopalswamy *et al.*, 2009a). For this, the EUV wavefront was assumed to have an elliptical structure and the distance between the

shock front, flux rope and expansion rate were calculated from 1 $R_\odot$ in SDO/AIA 211 Å images. For whitelight images, the same was done by assuming the CME to have a spherical structure. **The expression $B = v_a \times \sqrt{4\pi M N_e}$, where B, v_a, M and N_e are the magnetic field in *Gauss*, Alfv́en speed in cm/s, mass ascribed to each electron in the plasma in g and number density in cm^{-3}, respectively, was used to estimate the magnetic field strength**. For radio data, the split-band method was used. We also took advantage of polarization data obtained with the new instrument with which we used degree of circular polarization to determine B. Also, we combined estimates of B obtained at different wavelengths using different techniques and arrived at a common power-law expression for the radial distance range $1.1 - 4.5$ $R_\odot$. The newly determined power-law indices are very close to the previously obtained values (Patzold *et al.*, 1987; Lin, Kuhn, and Coulter, 2004; Mancuso and Garzelli, 2013b). This type of work is very rare and the results were published recently in Kumari *et al.* (2017c, 2019a).

Also, with the above observations, new density models were derived using STEREO-A/COR1, SOHO/LASCO-c2 and radio type II data. Hence the errors due to the assumption of different density model were minimized in the recent works. The polarized brightness intensities obtained with STEREO/COR1 and SOHO/ LASCO-c2 were converted to coronal densities over the region of interest using spherically symmetric inversion (SSI) technique (Wang and Davila, 2014). These were estimated before and during the onset of the CME, in order to calculate the density enhancement during the initiation phase. Also, the empirical models proposed / adopted in the works were found to be close to the existing extrapolation based density models (Newkirk, 1961; Zucca *et al.*, 2014a). Observations based density model, especially event specific are rarely adopted (Zucca *et al.*, 2014a; Kumari *et al.*, 2017c, 2019a). Taking advantage of high resolution imaging capabilities of the LOFAR, we were able to observe the type III bursts with better spatial resolution. A chapter-wise summary of science results are written in the following sections.

6.1.2.1 Chapter 2

For the split-band type II burst observed on 23 July 2016, independent estimates of $B(r)$ from radio and the associated white-light CME with flux rope structure were obtained. Instead of assuming one of the existing density model for the $N(r)$ values, the $N(r)$ values were obtained from STEREO-A/COR1 and SOHO/LASCO-C2 pB measurements. The $B(r)$ values, spread over the range $r \approx 2.5 - 4.5$ $R_\odot$ were used to arrive at a single power-law of the form $B(r) = 6.7r^{-2.6}$ G. The power-law index (i.e.-2.6) is in good agreement with that mentioned in the literature by different authors for the variation of $B(r)$ in the outer corona: i) for example, using Faraday rotation observations of the linearly polarized carrier signals of the HELIOS spacecraft, Patzold *et al.* (1987) found that $B(r)$ varies as $r^{-2.7}$ in the range $r \approx 3 - 10$

$R_\odot$; ii) recently, Mancuso and Garzelli (2013b) reported $B(r) = 3.76r^{-2.29}$ G in the range $r \approx 5-14$ $R_\odot$ using observations of similar signals from extragalactic radio sources occulted by the solar corona. Considering $B(r)$ values at specific r in the outer corona. Spangler (2005) and Gopalswamy and Yashiro (2011) have estimated $B(r) \approx 39$ mG and ≈ 48 mG at $r \approx 6.2$ $R_\odot$ and ≈ 6.0 $R_\odot$, respectively. Compared to these, the power-law expression derived here predicts $B(r) \approx 58$ mG and ≈ 63 mG at the above distances, respectively. Therefore, unambiguous estimates of $B(r)$ in the middle corona can be obtained using radio and white-light observations upon identifying the appropriate $N(r)$ there.

6.1.2.2 Chapter 3

The high frequency type II burst with an unusually high drift rate (≈ 2 MHz/s) was observed with the wideband spectro-polarimeter on Nov 4, 2015. The estimated speed of the MHD shock driver of the burst varies with time. The peak speed and acceleration are considerably large, ≈ 2500 km/s and ≈ 17 km/s^2 , respectively. The time profile of the shock speed derived from radio observations correlates well with the light curve of the associated soft X-ray flare. Since there is also spatio-temporal association between the type II burst and the associated CME, the results indicate that (i) the high frequency coronal type II burst is due to MHD shock driven by the CME and (ii) the shock speed profile of the type II burst represents the near-Sun kinematics of the CME.

6.1.2.3 Chapter 4

On March 16, 2016, a CME, coronal type II radio burst and flux rope structure (in EUV) were observed simultaneously. The radio burst was observed in both the imaging and spectral mode. The combined h-t plot indicates that all the three events are closely associated. An empirical relation for the coronal electron density ($N_e(r) = 2.3 \times 10^8 r^{-5.3}$) was derived using EUV observations of the flux rope structure associated with the CME, spectral and imaging observations of the type II burst associated with the CME, and pB measurements of the corresponding whitelight CME. Using the density values thus obtained and Alfv́en Mach number (M_a) values from EUV and radio observations, we independently estimated the coronal magnetic field strength ($B(r)$). The results indicate that $B(r) = 2.59 \times r^{-2.16}$ in the distance range $r \approx 1.1$ - 2.2 $R_\odot$. The only available two-dimensional magnetic field map obtained using coronal Zeeman magnetometry and full-Stokes spectro-polarimetric measurements indicate that $B \approx 3.6$ G at $r \approx 1.1$ $R_\odot$ (Lin, Kuhn, and Coulter, 2004). Compared to it, these results predict $B \approx 2.2$ G at the same distance. Gopalswamy *et al.* (2012) reported $B \approx$ 1.36 - 1.1 G in the range $r \approx 1.29$ - 1.47 $R_\odot$ using similar observations of a split-band type II burst associated with a CME flux rope structure and shock in EUV. These agree reasonably with the values predicted by the above expression for $B(r)$. Mancuso and Garzelli (2013a)

had derived $B(r) = 3.76 \times r^{-2.29}$ in the distance range $r \approx 1.8$ - 14 $R_\odot$ by combining split-band type II observations and Faraday rotation measurements of extragalactic radio sources occulted by the solar corona. This is nearly the same as the empirical relation for $B(r)$ in the present case. The consistency between the different results though they correspond to different active regions observed at different epochs strengthens the robustness of the estimates of $B(r)$ using radio observations and the empirical relationship for $B(r)$.

6.1.2.4 Chapter 5

A group of type III observed with LOFAR on March 30, 2018 were studied. With high spectral and temporal resolution of LOFAR, in both interferometric as well as tied-array beam imaging, there were distinguished five different trail of individual type III. Tracing the path of these individual trails, five different trajectories of the electrons on the solar surface were obtained, which in conclusion, provides the configuration of the magnetic fields profiles. This also gives a possible scenario that explains why type III radio bursts most often happens in groups. Using the tied-array full stokes capability, the coronal magnetic field distribution along these different field lines were estimated. The variation in the power law index were between $1.6 - 3.4$, which further indicates that there at least five open magnetic filed lines present near the active region.

6.1.3 Novelty of thesis

The **novel** aspects of this thesis are:

- **New Spectro-polarimeter :** The improvement over the existing GRASP, in terms of bandwidth of observation, better spectral and temporal resolution are achieved.
- **Detection of weak bursts :** With the new instrument, it was possible to detect few weak bursts, which were not seen by the regular SA based system or other spectrographs worldwide.
- **Evidence for CME driven type II burst :** Using high frequency type II burst observations the spatio-temporal association between the type II burst and the associated CME, it was unambiguously established that the CME is the driver of shock.
- **Magnetic field estimation :** Using the new spectro-polarimeter observations and other multi-wavelength observations, coronal magnetic field strengths were estimated between $1.1 - 4.5$ $R_\odot$. A single power-law index was derived to describe the B field distribution.

- **Constraining the density model :** Using multi-wavelngth observations one can constrain the selection of density model to determine different coronal parameters.
- **LOFAR interferometric images :** The type III images are one of the first active Sun interferometric images obtained with LOFAR.

6.2 Future Work

6.2.1 GRASP Improvements

The digital backend system developed in this PhD work can further be improved by using higher bit ADC, for eg. a 12 bit ADC would provide $\sim$ 64 dB dynamic range. Also, the spectral and temporal resolutions can be improved further in terms of tens of kHz and $\leq$ few ms. This would enable the recording of fine structures in the solar radio bursts, which can be used to study the fragmentation in the bursts, inhomogeneities in electron density distributions, turbulence in the solar corona, etc. Further, the operational bandwidth can be increased by relaxing the lower frequency cut-off (around $\sim$ 5 MHz) due to the unusual extended minimum period. Upper frequency can be increased up to $\sim$ 1 GHz, as the antenna frontends are capable of functioning till 1 GHz. For calibration, a more robust method may be adopted (for example, circularly polarized emission from the satellites). A realistic approach for real time automatic detection of solar radio bursts may be implemented on-board. Real time RFI mitigation could be a way to effectively use all the bits in the ADC, hence the DR of the system may improve further. This would increase the probability of detecting weak bursts.

6.2.2 GRAPH Backend

The ROACH based digital spectro-polarimeter backend can serve the first step for developing the augmented GRAPH new digital backend for polarimetric imaging of the Sun. The new GRAPH digital backend would overcome the limitations such as fixed bandwidth and fixed frequency of observation, etc. This FPGA based correlator may be implemented on ROACH[2] board with Xilinx Virtex-5 and 64ADCx64-12[3]. At present, the GRAPH back-end receiver system consist of **1024 channel** digital correlator (Ramesh *et al.*, 1998). The firmware will have the same functionality with additional features viz. four frequency observation within the time period of $\sim$ 256 ms . The proposed design may use a 10Gbe[4] Ethernet port for transferring the raw visibility data to the data acquisition system. Further these visibilities may be converted to Astronomical Image Processing System (AIPS) and Common

[2] https://casper.ssl.berkeley.edu/wiki/ROACH
[3] https://casper.ssl.berkeley.edu/wiki/64ADCx64-12
[4] https://casper.ssl.berkeley.edu/wiki/Recommended_10_GbE_Hardware

Astronomy Software Applications (CASA) readable fits format for processing and obtaining two dimensional solar images between 40 - 120 MHz. Figure 6.2 shows the simulated visibilites for the old GRAPH and upcoming GRAPH array.

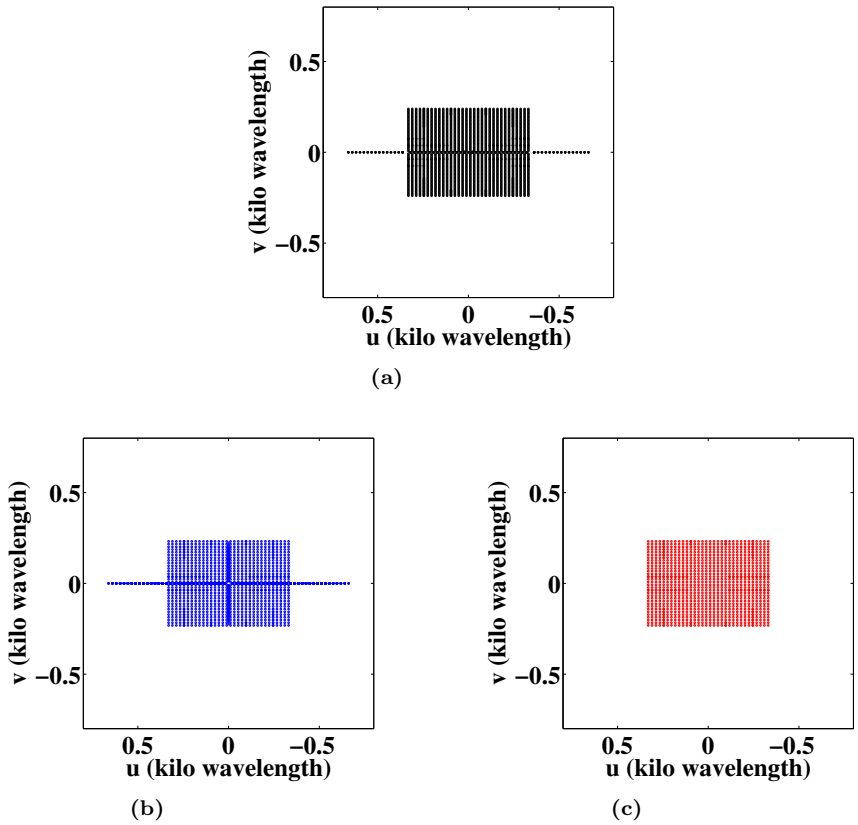

Figure 6.2: The UV plane distribution of visibilities (simulated) for (a) existing GRAPH in total intensity (Stokes-I); (b) for upcoming GRAPH in total intensity; (c) for upcoming GRAPH in circular polarized intensity (Stokes-V).

6.2.3 Compliments to other missions

Of late, there are many space based missions and ground based instruments (dedicated and non-dedicated) are available for solar observations. In meter wavelengths, the frequency coverage of Square Kilometer Array (SKA) which is under construction, the Murchison Widefield Array (MWA) that operate between $80 - 300$ MHz, overlap with GRASP. The observations with GRASP and upcoming GRAPH can be combined with that of the above instruments to study and understand complex events. Recently, ALMA has also produced few solar observations in GHz range; The metric counterparts observed with GRASP may be combined to improve our current understanding of the related subject matter. The observations of the radio emission from the Sun using SKA may be used to diagnose various phenomena that take place on the Sun and in the heliosphere as it is going to have square kilometre of collecting area. The improvement in sensitivity may open paths for new

discoveries[5]. LOFAR, which has high resolution observations, but are limited to $\leq$ 250 MHz, can take advantage of GRASP higher frequency range ($\sim$ 500 MHz), despite its limited sensitivity, DR and SNR. Solar orbiter mission of European Space Agency (ESA) has on-board Radio and Plasma Waves (RPW) instrument[6] that can observe the solar wind and measure the coronal magnetic fields. GRASP observations in the metric wavelengths will complement the decameter observations with RPW.

Solar orbiter also has Multi Element Telescope for Imaging and Spectroscopy (METIS) coronagraph[7], which can observe $1.4 - 3.0$ $R_\odot$ and can provide data on the dynamics of the corona. Since GRAPH also observes the above height range the data can be combined to extract new scienfitic results. The third satellite mission of ESA, PROBA-3 also has a coronagraph that can observe the corona in the same height range. GRASP can also compliment the observations of the solar corona with Aditya-L1, which is going to be the first Indian mission to study the Sun. The latter is going to carry the Visible Emission Line Coronagraph (VELC) payload[8] that is planned to observe the corona between 1.05 and 3.0 $R_\odot$. Recent NASA mission, Parker probe has one of the key goals as the determination of the structure and dynamics of the magnetic fields of the sources of solar wind that can be compared with the B field values obtained with GRASP in the 'middle' corona and may be combined to study the magnetic field distribution in the corona.

[5] https://www.skatelescope.org/the-ska-project/
[6] http://sci.esa.int/solar-orbiter/51217-instruments/
[7] http://metis.oato.inaf.it/
[8] https://www.isro.gov.in/aditya-l1-first-indian-mission-to-study-sun

Bibliography

Alfvén, H., Carlqvist, P.: 1967, Currents in the Solar Atmosphere and a Theory of Solar Flares. *Solar Physics* **1**(2), 220. DOI. ADS.

Allen, C.W.: 1947, Solar Radio-Noise of 200 Mc. /s. and its relation to Solar Observations. *Monthly Notices of the Royal Astronomical Society* **107**, 386. DOI. ADS.

Aschwanden, M.J.: 2005, *Physics of the Solar Corona. An Introduction with Problems and Solutions (2nd edition)*. ADS.

Aubier, M., Leblanc, Y., Boischot, A.: 1971, Observations of the Quiet Sun at Decameter Wavelengths - Effects of Scattering on the Brightness Distribution. *Astron. Astrophys.* **12**, 435. ADS.

Aurass, H.: 1997, Coronal Mass Ejections and Type II Radio Bursts. In: Trottet, G. (ed.) *Coronal Physics from Radio and Space Observations*, *Lecture Notes in Physics, Berlin Springer Verlag* **483**, 135. DOI. ADS.

Bakunin, L.M., Ledenev, V.G., Kosugi, T., McLean, D.J.: 1990, The harmonic structure of a type II burst on 12 May, 1983. *Solar Phys.* **129**, 379. DOI. ADS.

Barve, I.V., Kumari, A., Ramesh, R., Bane, K.: 2019, A high spectral and temporal resolution roach-based digital back-end for low radio frequency spectro-polarimetry. In: *2019 URSI Asia-Pacific Radio Science Conference (AP-RASC)*, 1. DOI.

Bastian, T.S., Pick, M., Kerdraon, A., Maia, D., Vourlidas, A.: 2001, The Coronal Mass Ejection of 1998 April 20: Direct Imaging at Radio Wavelengths. *Astrophys. J. Lett.* **558**, L65. DOI. ADS.

Baumbach, S.: 1937, Strahlung, Ergiebigkeit und Elektronendichte der Sonnenkorona. *Astron. Nach* **263**, 121. DOI. ADS.

Beck, R.: 1995, *Solar astronomy handbook*. ADS.

Bein, B.M., Berkebile-Stoiser, S., Veronig, A.M., Temmer, M., Muhr, N., Kienreich, I., Utz, D., Vršnak, B.: 2011, Impulsive Acceleration of Coronal Mass Ejections. I. Statistics and Coronal Mass Ejection Source Region Characteristics. *The Astrophysical Journal* **738**(2), 191. DOI. ADS.

Benz, A.: 1994, Books-Received - Plasma Astrophysics - Kinetic Processes in Solar and Stellar Coronae. *Science* **263**, 842. ADS.

Benz, A.O., Monstein, C., Meyer, H., Manoharan, P.K., Ramesh, R., Altyntsev, A., Lara, A., Paez, J., Cho, K.-S.: 2009, A World-Wide Net of Solar Radio Spectrometers: e-CALLISTO. *Earth Moon and Planets* **104**, 277. DOI. ADS.

Boischot, A.: 1957, Caractères d'un type d'émission hertzienne associé à certaines éruptions chromosphériques. *CRAS* **244**, 1326.

Bolton, J.G.: 1948, Discrete Sources of Galactic Radio Frequency Noise. *Nature* **162**(4108), 141. DOI. ADS.

Bougeret, J.-L., Kaiser, M.L., Kellogg, P.J., Manning, R., Goetz, K., Monson, S.J., Monge, N., Friel, L., Meetre, C.A., Perche, C., Sitruk, L., Hoang, S.: 1995a, Waves: The Radio and Plasma Wave Investigation on the Wind Spacecraft. *Space Sci. Rev.* **71**(1-4), 231. DOI. ADS.

Bougeret, J.-L., Kaiser, M.L., Kellogg, P.J., Manning, R., Goetz, K., Monson, S.J., Monge, N., Friel, L., Meetre, C.A., Perche, C., Sitruk, L., Hoang, S.: 1995b, Waves: The Radio and Plasma Wave Investigation on the Wind Spacecraft. *Space Science Reviews* **71**(1-4), 231. DOI. ADS.

Breneman, H.H., Stone, E.C.: 1985, Solar coronal and photospheric abundances from solar energetic particle measurements. *The Astrophysical Journal* **299**, L57. DOI. ADS.

Brueckner, G.E., Howard, R.A., Koomen, M.J., Korendyke, C.M., Michels, D.J., Moses, J.D., Socker, D.G., Dere, K.P., Lamy, P.L., Llebaria, A., Bout, M.V., Schwenn, R., Simnett, G.M., Bedford, D.K., Eyles, C.J.: 1995, The Large Angle Spectroscopic Coronagraph (LASCO). *Solar Phys.* **162**, 357. DOI. ADS.

Bumba, V., Howard, R.: 1965, Large-Scale Distribution of Solar Magnetic Fields. *The Astrophysical Journal* **141**, 1502. DOI. ADS.

Burke, B.F., Franklin, K.: 1955, Observations of a variable radio source associated with the planet jupiter. *Journal of Geophysical Research* **60**(2), 213.

Burke, B.F., Graham-Smith, F.: 1996, *An Introduction to Radio Astronomy*. ADS.

Cane, H.V., Stone, R.G.: 1984, Type II solar radio bursts, interplanetary shocks, and energetic particle events. *The Astrophysical Journal* **282**, 339. DOI. ADS.

Carrel, R.L.: 1961, Analysis and design of the log-periodic dipole antenna. Technical report, Illinois Univ at Urbana Electrical Engineering Research Lab.

Carrington, R.C.: 1860, On Dr. Sœmmering's Observations of the Solar Spots, in the years 1826-1829. *Monthly Notices of the Royal Astronomical Society* **20**, 71. DOI. ADS.

Chiuderi-Drago, F., Bandiera, R., Willson, R.F., Slottje, C., Falciani, R., Antonucci, E., Lang, K.R., Shibasaki, K.: 1982, Multiple wavelength observations of a solar active region. *Solar Phys.* **80**, 71. DOI. ADS.

Cho, K.-S., Lee, J., Gary, D.E., Moon, Y.-J., Park, Y.D.: 2007, Magnetic Field Strength in the Solar Corona from Type II Band Splitting. *Astrophys. J.* **665**, 799. DOI. ADS.

Cho, K.-S., Bong, Y.-H. S.-C. Kim, Moon, Y.-J., Dryer, M., Shanmugaraju, A., Lee, J., Park, Y.D.: 2008, Low coronal observations of metric type II associated CMEs by MLSO coronameters. *Astron. Astrophys.* **491**, 873. DOI. ADS.

Cho, K.-S., Gopalswamy, N., Kwon, R.-Y., Kim, R.-S., Yashiro, S.: 2013, A High-frequency Type II Solar Radio Burst Associated with the 2011 February 13 Coronal Mass Ejection. *The Astrophysical Journal* **765**(2), 148. DOI. ADS.

Claßen, H.T., Aurass, H.: 2002, On the association between type II radio bursts and CMEs. *Astron. Astrophys.* **384**, 1098. DOI. ADS.

Clerk Maxwell, J.: 1865, A Dynamical Theory of the Electromagnetic Field. *Philosophical Transactions of the Royal Society of London Series I* **155**, 459. ADS.

Clerk Maxwell, J., Niven, W.D.: 2011, *The Scientific Papers of James Clerk Maxwell*. ADS.

Cliver, E.W., Kahler, S.W., Reames, D.V.: 2004, Coronal Shocks and Solar Energetic Proton Events. *The Astrophysical Journal* **605**(2), 902. DOI. ADS.

Cliver, E.W., Webb, D.F., Howard, R.A.: 1999, On the origin of solar metric type II bursts. *Solar Physics* **187**(1), 89. DOI. ADS.

Collett, E.: 1992, *Polarized light. Fundamentals and applications*. ADS.

Copernicus, N.: 1543, *De revolutionibus orbium coelestium*. ADS.

Cowling, T.G.: 1933, The magnetic field of sunspots. *Mon. Not. Roy. Astron. Soc.* **94**, 39. DOI. ADS.

Das, A.K., Bhargava, B.N.: 1953, Radio Noise-bursts from Solar M-Regions. *Nature* **172**, 855. DOI. ADS.

DeForest, C., Hoeksema, J., Gurman, J., Thompson, B., Plunkett, S., Howard, R., Harrison, R., Hassler, D.: 1997, Polar plume anatomy: results of a coordinated observation. In: *The First Results from SOHO*, 393.

DuHamel, R., Isbell, D.: 1966, Broadband logarithmically periodic antenna structures. In: *1958 IRE International Convention Record* **5**, 119. IEEE.

Dulk, G.A.: 1970, Positions of the Fundamental and Harmonic Sources of a Type II Solar Burst. *Proceedings of the Astronomical Society of Australia* **1**, 308. DOI. ADS.

Dulk, G.A.: 1985, Radio emission from the sun and stars. *Annurev.aa.* **23**, 169. DOI. ADS.

Dulk, G.A., McLean, D.J.: 1978, Coronal magnetic fields. *Solar Phys.* **57**, 279. DOI. ADS.

Dulk, G.A., Suzuki, S.: 1980, The position and polarization of Type III solar bursts. *Astron. Astrophys.* **88**, 203. ADS.

Ebenezer, E., Ramesh, R., Subramanian, K.R., SundaraRajan, M.S., Sastry, C.V.: 2001, A new digital spectrograph for observations of radio burst emission from the Sun. *Astron. Astrophys.* **367**, 1112. DOI. ADS.

Ebenezer, E., Subramanian, K.R., Ramesh, R., Sundararajan, M.S., Kathiravan, C.: 2007, Gauribidanur radio array solar spectrograph (GRASS). *Bulletin of the Astronomical Society of India* **35**, 111. ADS.

Eddy, J.A.: 1974, A Nineteenth-century Coronal Transient. *Astronomy and Astrophysics* **34**, 235. ADS.

Elgaroy, O.: 1977, *Solar noise storms by eo elgaroy.*

Fainberg, J., Stone, R.G.: 1970, Type III Solar Radio Burst Storms Observed at Low Frequencies. *Solar Phys.* **15**, 222. DOI. ADS.

Forbes, T.G.: 2000, A review on the genesis of coronal mass ejections. *Journal of Geophysical Research* **105**(A10), 23153. DOI. ADS.

Gary, D.E., Dulk, G.A., House, L.L., Illing, R., Wagner, W.J.: 1985, The Type IV burst of 1980 June 29, 0233 UT - Harmonic plasma emission. *Astron. Astrophys.* **152**, 42. ADS.

Gelfreikh, G.B.: 2004, Coronal Magnetic Field Measurements Through Bremsstrahlung Emission. In: Gary, D.E., Keller, C.U. (eds.) *Astrophysics and Space Science Library*, *Astrophysics and Space Science Library* **314**, 115. DOI. ADS.

Gingerich, O.: 1999, The Copernican Revolution Revisited. In: *American Astronomical Society Meeting Abstracts* **195**, 123.02. ADS.

Gopalswamy, N.: 2006a, Coronal Mass Ejections and Type II Radio Bursts. *Washington DC American Geophysical Union Geophysical Monograph Series* **165**, 207. DOI. ADS.

Gopalswamy, N.: 2006b, Coronal Mass Ejections of Solar Cycle 23. *Journal of Astrophysics and Astronomy* **27**, 243. DOI. ADS.

Gopalswamy, N., Kundu, M.R.: 1990, Multiple moving magnetic structures in the solar corona. *Solar Phys.* **128**, 377. DOI. ADS.

Gopalswamy, N., Yashiro, S.: 2011, The Strength and Radial Profile of the Coronal Magnetic Field from the Standoff Distance of a Coronal Mass Ejection-driven Shock. *Astrophys. J. Lett.* **736**, L17. DOI. ADS.

Gopalswamy, N., Thejappa, G., Sastry, C.V., Tlamicha, A.: 1986, Estimation of Coronal Magnetic Fields Using Type-I Emission. *Bulletin of the Astronomical Institutes of Czechoslovakia* **37**, 115. ADS.

Gopalswamy, N., Yashiro, S., Kaiser, M.L., Thompson, B.J., Plunkett, S.: 1999, Multiwavelength Signatures of Coronal Mass Ejection. In: Bastian, T.S., Gopalswamy, N., Shibasaki, K. (eds.) *Proceedings of the Nobeyama Symposium*, 207. ADS.

Gopalswamy, N., Aguilar-Rodriguez, E., Yashiro, S., Nunes, S., Kaiser, M.L., Howard, R.A.: 2005, Type II radio bursts and energetic solar eruptions. *Journal of Geophysical Research (Space Physics)* **110**(A12), A12S07. DOI. ADS.

Gopalswamy, N., Yashiro, S., Temmer, M., Davila, J., Thompson, W.T., Jones, S., McAteer, R.T.J., Wuelser, J.-P., Freeland, S., Howard, R.A.: 2009a, EUV Wave Reflection from a Coronal Hole. *The Astrophysical Journal* **691**(2), L123. DOI. ADS.

Gopalswamy, N., Thompson, W.T., Davila, J.M., Kaiser, M.L., Yashiro, S., Mäkelä, P., Michalek, G., Bougeret, J.-L., Howard, R.A.: 2009b, Relation Between Type II Bursts and CMEs Inferred from STEREO Observations. *Solar Phys.* **259**, 227. DOI. ADS.

Gopalswamy, N., Nitta, N., Akiyama, S., Mäkelä, P., Yashiro, S.: 2012, Coronal Magnetic Field Measurement from EUV Images Made by the Solar Dynamics Observatory. *Astrophys. J.* **744**, 72. DOI. ADS.

Gopalswamy, N., Xie, P. H. Mäkelä, Yashiro, S., Akiyama, S.: 2013a, Height of shock formation in the solar corona inferred from observations of type II radio bursts and coronal mass ejections. *Adv. Sp. Res.* **51**, 1981. DOI. ADS.

Gopalswamy, N., Xie, H., Akiyama, S., Yashiro, S., Usoskin, I.G., Davila, J.M.: 2013b, The First Ground Level Enhancement Event of Solar Cycle 24: Direct Observation of Shock Formation and Particle Release Heights. *The Astrophysical Journal* **765**(2), L30. DOI. ADS.

Gosling, J.T.: 1997, Coronal mass ejections: An overview. *Washington DC American Geophysical Union Geophysical Monograph Series* **99**, 9. DOI. ADS.

Gosling, J.T., Asbridge, J.R., Bame, S.J., Feldman, W.C.: 1978, Solar wind stream interfaces. *Journal of Geophysical Research* **83**(A4), 1401. DOI. ADS.

Gosling, J.T., Bame, S.J., McComas, D.J., Phillips, J.L.: 1990, Coronal mass ejections and large geomagnetic storms. *Geophysical Research Letters* **17**(7), 901. DOI. ADS.

Graham, D.B., Cairns, I.H.: 2015, The Langmuir waves associated with the 1 December 2013 type II burst. *Journal of Geophysical Research (Space Physics)* **120**(6), 4126. DOI. ADS.

Grognard, R.J.M., McLean, D.J.: 1973, Non-Existence of Linear Polarization in Type III Solar Bursts at 80 MHz. *Solar Phys.* **29**, 149. DOI. ADS.

Hale, G.E.: 1908, On the Probable Existence of a Magnetic Field in Sun-Spots. *The Astrophysical Journal* **28**, 315. DOI. ADS.

Hale, G.E., Ellerman, F., Nicholson, S.B., Joy, A.H.: 1919, The Magnetic Polarity of Sun-Spots. *The Astrophysical Journal* **49**, 153. DOI. ADS.

Hariharan, K., Ramesh, R., Kathiravan, C.: 2015, Observations of Near-Simultaneous Split-Band Solar Type-II Radio Bursts at Low Frequencies. *Solar Phys.* **290**, 2479. DOI. ADS.

Hariharan, K., Ramesh, R., Kishore, P., Kathiravan, C., Gopalswamy, N.: 2014, An Estimate of the Coronal Magnetic Field near a Solar Coronal Mass Ejection from Low-frequency Radio Observations. *Astrophys. J.* **795**, 14. DOI. ADS.

Hariharan, K., Ramesh, R., Kathiravan, C., Wang, T.J.: 2016, Simultaneous Near-Sun Observations of a Moving Type IV Radio Burst and the Associated White-Light Coronal Mass Ejection. *Solar Phys.* **291**, 1405. DOI. ADS.

Harra-Murnion, L.K., Schmieder, B., van Driel-Gesztelyi, L., Sato, J., Plunkett, S.P., Rudawy, P., Rompolt, B., Akioka, M., Sakao, T., Ichimoto, K.: 1998, Multi-wavelength observations of POST flare loops in two long duration solar flares. *Astron. Astrophys.* **337**, 911. ADS.

Hetherington, B.: 1996, *A chronicle of pre-telescopic astronomy*. ADS.

Hewish, A.: 1970, Pulsars. *Annual Review of Astronomy and Astrophysics* **8**, 265. DOI. ADS.

Hey, J.: 1948, Galactic and solar radio noise. *Journal of the Institution of Electrical Engineers-Part III: Radio and Communication Engineering* **95**(37), 333.

Howard, R.A., Moses, J.D., Vourlidas, A., Newmark, J.S., Socker, D.G., Plunkett, S.P., Korendyke, C.M., Cook, J.W., Hurley, A., Davila, J.M., Thompson, W.T., St Cyr, O.C., Mentzell, E., Mehalick, K., Lemen, J.R., Wuelser, J.P., Duncan, D.W., Tarbell, T.D., Wolfson, C.J., Moore, A., Harrison, R.A., Waltham, N.R., Lang, J., Davis, C.J., Eyles, C.J., Mapson-Menard, H., Simnett, G.M., Halain, J.P., Defise, J.M., Mazy, E., Rochus, P., Mercier, R., Ravet, M.F., Delmotte, F., Auchere, F., Delaboudiniere, J.P., Bothmer, V., Deutsch, W., Wang, D., Rich, N., Cooper, S., Stephens, V., Maahs, G., Baugh, R., McMullin, D., Carter, T.: 2008, Sun Earth Connection Coronal and Heliospheric Investigation (SECCHI). *Space Sci. Rev.* **136**, 67. DOI. ADS.

Howard, R., Sheeley Jr, N., Koomen, M., Michels, D.: 1985, Coronal mass ejections: 1979–1981. *Journal of Geophysical Research: Space Physics* **90**(A9), 8173.

Hudson, H.: 1991, Solar flares, microflares, nanoflares, and coronal heating. *Solar Physics* **133**(2), 357.

Hundhausen, A.: 1999, Coronal mass ejections. In: *The Many Faces of the Sun*, 143.

Isbell, D.: 1960, Log periodic dipole arrays. *IRE transactions on antennas and propagation* **8**(3), 260.

Jansky, K.G.: 1933, Electrical disturbances apparently of extraterrestrial origin. *Proceedings of the Institute of Radio Engineers* **21**(10), 1387.

Jansky, K.G.: 1933, Radio Waves from Outside the Solar System. *Nature* **132**(3323), 66. DOI. ADS.

Kahler, S.W.: 1992, Solar flares and coronal mass ejections. *Annual Review of Astronomy and Astrophysics* **30**, 113. DOI. ADS.

Kaiser, M., Reiner, M., Gopalswamy, N., Howard, R., St. Cyr, O., Thompson, B., Bougeret, J.-L.: 1998, Type ii radio emissions in the frequency range from 1–14 mhz associated with the april 7, 1997 solar event. *Geophysical research letters* **25**(14), 2501.

Kathiravan, C., Ramesh, R., Indrajit V. Barve., Rajalingam, M.: 2011, Radio Observations of the Solar Corona During an Eclipse. *Astrophys. J.* **730**, 91. DOI. ADS.

Kippenhahn, R., Schlüter, A.: 1957, Eine theorie der solaren filamente. mit 7 textabbildungen. *Zeitschrift fur Astrophysik* **43**, 36.

Kishore, P., Kathiravan, C., Ramesh, R., Rajalingam, M., Barve, I.V.: 2014, Gauribidanur Low-Frequency Solar Spectrograph. *Solar Phys.* **289**, 3995. DOI. ADS.

Kishore, P., Ramesh, R., Kathiravan, C., Rajalingam, M.: 2015, A Low-Frequency Radio Spectropolarimeter for Observations of the Solar Corona. *Solar Phys.* **290**, 2409. DOI. ADS.

Kishore, P., Ramesh, R., Hariharan, K., Kathiravan, C., Gopalswamy, N.: 2016, Constraining the Solar Coronal Magnetic Field Strength using Split-band Type II Radio Burst Observations. *Astrophys. J.* **832**, 59. DOI. ADS.

Kishore, P., Kathiravan, C., Ramesh, R., Ebenezer, E.: 2017, Coronal Magnetic Field Lines and Electrons Associated with Type III-V Radio Bursts in a Solar Flare. *Journal of Astrophysics and Astronomy* **38**(2), 24. DOI. ADS.

Kivelson, A.: 1995, *Introduction to space physics.*

Klein, B., Philipp, S.D., Güsten, R., Krämer, I., Samtleben, D.: 2006, A new generation of spectrometers for radio astronomy: Fast fourier transform spectrometer. In: *Millimeter and Submillimeter Detectors and Instrumentation for Astronomy III* **6275**, 627511. International Society for Optics and Photonics.

Kliem, B., Krueger, A., Treumann, R.A.: 1992, Third plasma harmonic radiation in type II bursts. *Solar Phys.* **140**, 149. DOI. ADS.

Kojima, M., Fujiki, K.-i., Hirano, M., Tokumaru, M., Ohmi, T., Hakamada, K.: 2004, Solar wind properties from ips observations. In: *The Sun and the heliosphere as an Integrated System*, 147.

Kraus, J.D.: 1966, *Radio astronomy.* ADS.

Krucker, S., Benz, A.O.: 2000, Are Heating Events in the Quiet Solar Corona Small Flares Multiwavelength Observations of Individual Events. *Solar Physics* **191**(2), 341. DOI. ADS.

Kumar, P., Innes, D.E., Cho, K.-S.: 2016, Flare-generated Shock Wave Propagation through Solar Coronal Arcade Loops and an Associated Type II Radio Burst. *The Astrophysical Journal* **828**(1), 28. DOI. ADS.

Kumari, A., Ramesh, R., Kathiravan, C., Wang, T.J.: 2017a, Addendum to: Strength of the Solar Coronal Magnetic Field - A Comparison of Independent Estimates Using Contemporaneous Radio and White-Light Observations. *Solar Physics* **292**(12), 177. DOI. ADS.

Kumari, A., Ramesh, R., Kathiravan, C., Gopalswamy, N.: 2017b, New Evidence for a Coronal Mass Ejection-driven High Frequency Type II Burst near the Sun. *Astrophys. J.* **843**, 10. DOI. ADS.

Kumari, A., Ramesh, R., Kathiravan, C., Wang, T.J.: 2017c, Strength of the Solar Coronal Magnetic Field - A Comparison of Independent Estimates Using Contemporaneous Radio and White-Light Observations. *Solar Physics* **292**(11), 161. DOI. ADS.

Kumari, A., Ramesh, R., Kathiravan, C., Wang, T.J., Gopalswamy, N.: 2019a, Direct Estimates of the Solar Coronal Magnetic Field Using Contemporaneous Extreme-ultraviolet, Radio, and White-light Observations. *The Astrophysical Journal* **881**(1), 24. DOI. ADS.

Kumari, A., Kathiravan, C., Ramesh, R., Barve, I.V.: 2019b, *A radio spectro-polarimeter for monitoring the activities on the sun.*

Kundu, M.R., Firor, J.W.: 1961, Interferometric Studies of Type IV Solar Bursts of Continuum Radiation on 340 and 87 Mc/s. *Astrophys. J.* **134**, 389. DOI. ADS.

Kundu, M.R., Stone, R.G.: 1984, Observations of solar radio bursts from meter to kilometer wavelengths. *Advances in Space Research* **4**(7), 261. DOI. ADS.

Kwon, R.-Y., Kramar, M., Wang, T., Ofman, L., Davila, J.M., Chae, J., Zhang, J.: 2013a, Global Coronal Seismology in the Extended Solar Corona through Fast Magnetosonic Waves Observed by STEREO SECCHI COR1. *Astrophys. J.* **776**, 55. DOI. ADS.

Kwon, R.-Y., Ofman, L., Olmedo, O., Kramar, M., Davila, J.M., Thompson, B.J., Cho, K.-S.: 2013b, STEREO Observations of Fast Magnetosonic Waves in the Extended Solar Corona Associated with EIT/EUV Waves. *Astrophys. J.* **766**, 55. DOI. ADS.

Lemen, J.R., Title, A.M., Akin, D.J., Boerner, P.F., Chou, C., Drake, J.F., Duncan, D.W., Edwards, C.G.: 2012, The Atmospheric Imaging Assembly (AIA) on the Solar Dynamics Observatory (SDO). *Solar Phys.* **275**, 17. DOI. ADS.

Lin, H., Kuhn, J.R., Coulter, R.: 2004, Coronal Magnetic Field Measurements. *The Astrophysical Journal* **613**(2), L177. DOI. ADS.

Lin, H., Penn, M.J., Tomczyk, S.: 2000, A New Precise Measurement of the Coronal Magnetic Field Strength. *Astrophys. J. Lett.* **541**, L83. DOI. ADS.

Lin, J., Mancuso, S., Vourlidas, A.: 2006, Theoretical Investigation of the Onsets of Type II Radio Bursts during Solar Eruptions. *The Astrophysical Journal* **649**(2), 1110. DOI. ADS.

Lin, R.P., Hudson, H.S.: 1976, Non-thermal processes in large solar flares. *Solar Phys.* **50**(1), 153. DOI. ADS.

Liu, W., Ofman, L.: 2014, Advances in Observing Various Coronal EUV Waves in the SDO Era and Their Seismological Applications (Invited Review). *Solar Physics* **289**(9), 3233. DOI. ADS.

Lu, E.T., Hamilton, R.J.: 1991, Avalanches and the distribution of solar flares. *The astrophysical journal* **380**, L89.

Lyot, B.: 1939, The study of the solar corona and prominences without eclipses (George Darwin Lecture, 1939). *Monthly Notices of the Royal Astronomical Society* **99**, 538. DOI. ADS.

Ma, S., Raymond, J.C., Golub, L., Lin, J., Chen, H., Grigis, P., Testa, P., Long, D.: 2011, Observations and Interpretation of a Low Coronal Shock Wave Observed in the EUV by the SDO/AIA. *Astrophys. J.* **738**, 160. DOI. ADS.

Magdalenić, J., Marqué, C., Zhukov, A.N., Vršnak, B., Veronig, A.: 2012, Flare-generated Type II Burst without Associated Coronal Mass Ejection. *The Astrophysical Journal* **746**(2), 152. DOI. ADS.

Mancuso, S., Garzelli, M.V.: 2013a, Coronal magnetic field strength from Type II radio emission: complementarity with Faraday rotation measurements. *Astron. Astrophys.* **560**, L1. DOI. ADS.

Mancuso, S., Garzelli, M.V.: 2013b, Radial profile of the inner heliospheric magnetic field as deduced from Faraday rotation observations. *Astron. Astrophys.* **553**, A100. DOI. ADS.

Mancuso, S., Raymond, J.C.: 2004, Coronal transients and metric type II radio bursts. I. Effects of geometry. *Astronomy and Astrophysics* **413**, 363. DOI. ADS.

Mancuso, S., Raymond, J.C., Kohl, J., Ko, Y.-K., Uzzo, M., Wu, R.: 2003, Plasma properties above coronal active regions inferred from SOHO/UVCS and radio spectrograph observations. *Astron. Astrophys.* **400**, 347. DOI. ADS.

Mann, G., Classen, T., Aurass, H.: 1995, Characteristics of coronal shock waves and solar type II radio bursts. *Astron. Astrophys.* **295**, 775. ADS.

Mann, G., Klassen, A., Aurass, H., Classen, H.-T.: 2003, Formation and development of shock waves in the solar corona and the near-Sun interplanetary space. *Astronomy and Astrophysics* **400**, 329. DOI. ADS.

Marsch, E.: 2006, Kinetic Physics of the Solar Corona and Solar Wind. *Living Reviews in Solar Physics* **3**(1), 1. DOI. ADS.

Maxwell, A., Swarup, G., Thompson, A.: 1958, The radio spectrum of solar activity. *Proceedings of the IRE* **46**(1), 142.

McLean, D.J., Labrum, N.R.: 1985a, *Solar radiophysics : studies of emission from the sun at metre wavelengths*. ADS.

McLean, D.J., Labrum, N.R.: 1985b, *Solar radiophysics: Studies of emission from the sun at metre wavelengths*. ADS.

Melrose, D.B., Sy, W.N.: 1972, Plasma emission processes in a magnetoactive plasma. *Australian Journal of Physics* **25**, 387. DOI. ADS.

Melrose, D.B., Dulk, G.A., Gary, D.E.: 1980, Corrected formula for the polarization of second harmonic plasma emission. *Pub. Astron. Soc. Aust.* **4**, 50. ADS.

Melrose, D.B., Dulk, G.A., Smerd, S.F.: 1978, The polarization of second harmonic plasma emission. *Astron. Astrophys.* **66**, 315. ADS.

Mercier, C., Subramanian, P., Kerdraon, A., Pick, M., Ananthakrishnan, S., Janardhan, P.: 2006, Combining visibilities from the giant meterwave radio telescope and the Nancay radio heliograph. High dynamic range snapshot images of the solar corona at 327 MHz. *Astron. Astrophys.* **447**, 1189. DOI. ADS.

Mitra, A.P.: 1974, Ionospheric effects of solar flares.

Monnier, J.D.: 2003, Optical interferometry in astronomy. *Reports on Progress in Physics* **66**(5), 789. DOI. ADS.

Monstein, C., Ramesh, R., Kathiravan, C.: 2007, Radio spectrum measurements at the Gauribidanur observatory. *Bulletin of the Astronomical Society of India* **35**, 473. ADS.

Mossman, J.E.: 1989, A comprehensive search for sunspots without the aid of a telescope, 1981-1982. *Quarterly Journal of the Royal Astronomical Society* **30**, 59. ADS.

Mugundhan, V., Hariharan, K., Ramesh, R.: 2017, Solar Type IIIb Radio Bursts as Tracers for Electron Density Fluctuations in the Corona. *Solar Physics* **292**(11), 155. DOI. ADS.

Mugundhan, V., Hariharan, K., Ramesh, R.: 2017, Solar type iiib radio bursts as tracers for electron density fluctuations in the corona. *Solar Physics* **292**(11), 155.

Mugundhan, V., Ramesh, R., Kathiravan, C., Gireesh, G.V.S., Hegde, A.: 2018, Spectropolarimetric Observations of Solar Noise Storms at Low Frequencies. *Solar Physics* **293**(3), 41. DOI. ADS.

Nelson, G., Sheridan, K., Suzuki, S.: 1985, Measurements of solar flux density and polarization. *Solar Radiophysics: Studies of Emission from the Sun at Metre Wavelengths*, 113.

Nelson, G.J., Sheridan, K.V., Suzuki, S.: 1985, In: McLean, D.J., Labrum, N.R. (eds.) *Measurements of solar flux density and polarization.*, 113. ADS.

Newkirk, J. Gordon: 1961, The Solar Corona in Active Regions and the Thermal Origin of the Slowly Varying Component of Solar Radio Radiation. *The Astrophysical Journal* **133**, 983. DOI. ADS.

Newkirk, J. Gordon: 1967, Structure of the Solar Corona. *Annual Review of Astronomy and Astrophysics* **5**, 213. DOI. ADS.

Newton, I.: 1987, Philosophiæ naturalis principia mathematica (mathematical principles of natural philosophy). *London (1687)* **1687**.

Nindos, A., Aurass, H., Klein, K.-L., Trottet, G.: 2008, Radio Emission of Flares and Coronal Mass Ejections. Invited Review. *Solar Physics* **253**(1-2), 3. DOI. ADS.

Orozco Suárez, D., Bellot Rubio, L.R., del Toro Iniesta, J.C., Tsuneta, S.: 2008, Magnetic field emergence in quiet Sun granules. *Astron. Astrophys.* **481**, L33. DOI. ADS.

Pant, V., Dolla, L., Mazumder, R., Banerjee, D., Prasad, S.K., Panditi, V.: 2015, Dynamics of on-disk plumes as observed with the interface region imaging spectrograph, the atmospheric imaging assembly, and the helioseismic and magnetic imager. *The Astrophysical Journal* **807**(1), 71.

Patsourakos, S., Vourlidas, A.: 2012, On the Nature and Genesis of EUV Waves: A Synthesis of Observations from SOHO, STEREO, SDO, and Hinode (Invited Review). *Solar Phys.* **281**, 187. DOI. ADS.

Patzold, M., Bird, M.K., Volland, H., Levy, G.S., Seidel, B.L., Stelzried, C.T.: 1987, The mean coronal magnetic field determined from HELIOS Faraday rotation measurements. *Solar Phys.* **109**, 91. DOI. ADS.

Pawsey, J.L., Payne-Scott, R., McCready, L.L.: 1946, Radio-Frequency Energy from the Sun. *Nature* **157**(3980), 158. DOI. ADS.

Penzias, A.A., Wilson, R.W.: 1965, A Measurement of Excess Antenna Temperature at 4080 Mc/s. *The Astrophysical Journal* **142**, 419. DOI. ADS.

Piddington, J., Davies, R.: 1953, Thermal radio emission from the sun and the source of coronal heating. *Monthly Notices of the Royal Astronomical Society* **113**(5), 582.

Pivnenko, S.: 2006, Log-periodic dipole antenna with low cross-polarization. In: *Antennas and Propagation, 2006. EuCAP 2006. First European Conference on*, 1. IEEE.

Pohjolainen, S., Pomoell, J., Vainio, R.: 2008, CME liftoff with high-frequency fragmented type II burst emission. *Astron. Astrophys.* **490**, 357. DOI. ADS.

Pomoell, J., Vainio, R., Pohjolainen, S.: 2009, Simulations of shock structures of a flare/CME event in the low corona. In: Gopalswamy, N., Webb, D.F. (eds.) *Universal Heliophysical Processes*, *Proc. IAU Symp. 257*, 493. ADS.

Pozar, D.M.: 2009, *Microwave engineering*.

Price, D.C.: 2016, Spectrometers and Polyphase Filterbanks in Radio Astronomy. *arXiv e-prints*, arXiv:1607.03579. ADS.

Ramesh, R.: 2011, Low frequency solar radio astronomy at the Indian Institute of Astrophysics (IIA). In: *Astronomical Society of India Conference Series*, *Astronomical Society of India Conference Series* **2**. ADS.

Ramesh, R., Sastry, C.V.: 2000, Radio observations of a coronal mass ejection induced depletion in the outer solar corona. *Astronomy and Astrophysics* **358**, 749. ADS.

Ramesh, R., Kathiravan, C., Narayanan, A.S.: 2011, Low-frequency Observations of Polarized Emission from Long-lived Non-thermal Radio Sources in the Solar Corona. *Astrophys. J.* **734**, 39. DOI. ADS.

Ramesh, R., Kathiravan, C., Sastry, C.V.: 2003, Metric Radio Observations of the Evolution of a "Halo" Coronal Mass Ejection Close to the Sun. *Astrophys. J. Lett.* **591**, L163. DOI. ADS.

Ramesh, R., Kathiravan, C., Sastry, C.V.: 2010, Estimation of Magnetic Field in the Solar Coronal Streamers Through Low Frequency Radio Observations. *Astrophys. J.* **711**, 1029. DOI. ADS.

Ramesh, R., Kathiravan, C., Satya Narayanan, A.: 2004, Seismology of the solar corona through observations of metric type IV radio burst emission. *Asian Journal of Physics* **13**, 277. ADS.

Ramesh, R., Subramanian, K.R., Sastry, C.V.: 1999, Eclipse Observations of Compact Sources in the Outer Solar Corona. *Solar Physics* **185**(1), 77. DOI. ADS.

Ramesh, R., Subramanian, K.R., Sundararajan, M.S., Sastry, C.V.: 1998, The Gauribidanur Radioheliograph. *Solar Physics* **181**(2), 439. DOI. ADS.

Ramesh, R., Kathiravan, C., Narayanan, A.S., Ebenezer, E.: 2003, Metric observations of transient, quasi-periodic radio emission from the solar corona in association with a "halo" CME and an "EIT wave" event. *Astron. Astrophys.* **400**, 753. DOI. ADS.

Ramesh, R., Nataraj, H., Kathiravan, C., Sastry, C.V.: 2006, The equatorial background solar corona during solar minimum. *The Astrophysical Journal* **648**(1), 707.

Ramesh, R., Kathiravan, C., Sundararajan, M.S., Barve, I.V., Sastry, C.V.: 2008, A Low-Frequency (30 - 110 MHz) Antenna System for Observations of Polarized Radio Emission from the Solar Corona. *Solar Physics* **253**(1-2), 319. DOI. ADS.

Ramesh, R., Kathiravan, C., Barve, I.V., Beeharry, G.K., Rajasekara, G.N.: 2010a, Radio Observations of Weak Energy Releases in the Solar Corona. *Astrophys. J.* **719**, L41. DOI. ADS.

Ramesh, R., Kathiravan, C., Kartha, S.S., Gopalswamy, N.: 2010b, Radioheliograph Observations of Metric Type II Bursts and the Kinematics of Coronal Mass Ejections. *Astrophys. J.* **712**, 188. DOI. ADS.

Ramesh, R., Anna Lakshmi, M., Kathiravan, C., Gopalswamy, N., Umapathy, S.: 2012, The Location of Solar Metric Type II Radio Bursts with Respect to the Associated Coronal Mass Ejections. *Astrophys. J.* **752**, 107. DOI. ADS.

Ramesh, R., Kishore, P., Mulay, S.M., Barve, I.V., Kathiravan, C., Wang, T.J.: 2013, Low-frequency Observations of Drifting, Non-thermal Continuum Radio Emission Associated with the Solar Coronal Mass Ejections. *Astrophys. J.* **778**, 30. DOI. ADS.

Ratcliffe, H., Kontar, E.P., Reid, H.A.S.: 2014, Large-scale simulations of solar type III radio bursts: flux density, drift rate, duration, and bandwidth. *Astron. Astrophys.* **572**, A111. DOI. ADS.

Ravindra, B., Prabhu, K., Elayaveilli Rangarajan, K., Shekar, B., Jagdev, S., Madan Mohan, K., Lancelot, P., Chellappan Thulasidharen, K., Gabriel, F., Selvendran, R.: 2016, Full-disk synoptic observations of the chromosphere using Hα telescope at the Kodaikanal Observatory. *Research in Astronomy and Astrophysics* **16**(8), 127. DOI.

Reames, D.V.: 1995, Solar energetic particles: A paradigm shift. *Reviews of Geophysics* **33**(S1), 585. DOI. ADS.

Reber, G.: 1949, Radio Astronomy. *Scientific American* **181**(3), 34. DOI. ADS.

Reber, G.: 1950, Galactic Radio Waves. *Leaflet of the Astronomical Society of the Pacific* **6**(259), 67. ADS.

Reber, G.: 1988, A Play Entitled the Beginning of Radio Astronomy. *Journal of the Royal Astronomical Society of Canada* **82**, 93. ADS.

Reid, H.A.S., Kontar, E.P.: 2018, Solar type III radio burst time characteristics at LOFAR frequencies and the implications for electron beam transport. *Astron. Astrophys.* **614**, A69. DOI. ADS.

Riddle, A.C.: 1970, 80 MHz Observations of a Moving Type IV Solar Burst, March 1, 1969. *Solar Phys.* **13**, 448. DOI. ADS.

Riddle, A.C.: 1974, On the Observation of Scattered Radio Emission from Sources in the Solar Corona. *Solar Physics* **35**(1), 153. DOI. ADS.

Rincon, F., Rieutord, M.: 2018, The Sun's supergranulation. *Living Reviews in Solar Physics* **15**, 6. DOI. ADS.

Roberts, J.A.: 1959, Solar Radio Bursts of Spectral Type II. *Australian Journal of Physics* **12**, 327. DOI. ADS.

Robinson, R.D.: 1985, Velocities of Type-II Solar Radio Events. *Solar Physics* **95**(2), 343. DOI. ADS.

Rodríguez, L.F.: 2007, Radio Astronomy: The Achievements and the Challenges. *Astrophysics and Space Science Proceedings* **2**, 199. DOI. ADS.

Ross, J.E., Aller, L.H.: 1976, The Chemical Composition of the Sun. *Science* **191**, 1223. DOI. ADS.

Rumsey, V.: 1966, Frequency independent antennas. In: *1958 IRE International Convention Record* **5**, 114. IEEE.

Ryabov, B.: 2004, Coronal Magnetic Field Measurements Through Quasi-Transverse Propagation. In: Gary, D.E., Keller, C.U. (eds.) *Astrophysics and Space Science Library*, *Astrophysics and Space Science Library* **314**, 135. DOI. ADS.

Ryle, M.: 1948, Some observations of solar radiation on wavelengths of 1.7 and 3.8 metres. *Journal of the Institution of Electrical Engineers-Part III: Radio and Communication Engineering* **95**(37), 333.

Sasikumar Raja, K., Ramesh, R.: 2013, Low-frequency Observations of Transient Quasi-periodic Radio Emission from the Solar Atmosphere. *Astrophys. J.* **775**, 38. DOI. ADS.

Sasikumar Raja, K., Kathiravan, C., Ramesh, R., Rajalingam, M., Barve, I.V.: 2013, Design and Performance of a Low-frequency Cross-polarized Log-periodic Dipole Antenna. *The Astrophysical Journal Supplement Series* **207**(1), 2. DOI. ADS.

Sasikumar Raja, K., Ramesh, R., Hariharan, K., Kathiravan, C., Wang, T.J.: 2014, An Estimate of the Magnetic Field Strength Associated with a Solar Coronal Mass Ejection from Low Frequency Radio Observations. *Astrophys. J.* **796**, 56. DOI. ADS.

Sasikumar Raja, K., Ingale, M., Ramesh, R., Subramanian, P., Manoharan, P.K., Janardhan, P.: 2016, Amplitude of solar wind density turbulence from 10 to 45 . *J. Geophys. Res.: Space Phys.* **121**, 11605. DOI. ADS.

Sastry, C.V.: 1989, The Gauribidanur radio observatory. *Indian Journal of Pure and Applied Physics* **27**, 331. ADS.

Sastry, C.V.: 2009, Polarization of the Thermal Radio Emission from Outer Solar Corona. *Astrophys. J.* **697**, 1934. DOI. ADS.

Shanmugaraju, A., Moon, Y.-J., Vrsnak, B.: 2009, Type II Radio Bursts with High and Low Starting Frequencies. *Solar Phys.* **254**, 297. DOI. ADS.

Sheeley, J. N. R.: 1967, Observations of Small-Scale Solar Magnetic Fields. *Solar Physics* **1**(2), 171. DOI. ADS.

Sheeley, N.R. Jr., Howard, R.A., Michels, D.J., Koomen, M.J., Schwenn, R., Muehlhaeuser, K.H., Rosenbauer, H.: 1985, Coronal mass ejections and interplanetary shocks. *J. Geophys. Res.* **90**, 163. DOI. ADS.

Shibasaki, K., Alissandrakis, C.E., Pohjolainen, S.: 2011, Radio Emission of the Quiet Sun and Active Regions (Invited Review). *Solar Phys.* **273**, 309. DOI. ADS.

Smerd, S.F., Sheridan, K.V., Stewart, R.T.: 1974, On Split-Band Structure in Type II Radio Bursts from the Sun. In: Newkirk, G.A. (ed.) *Coronal Disturbances*, *Proc. IAU Symp. 57*, 389. ADS.

Smerd, S.F., Sheridan, K.V., Stewart, R.T.: 1975, Split-Band Structure in Type II Radio Bursts from the Sun. *Astrophys. Lett.* **16**, 23. ADS.

Smerd, S.F., Wild, J.P., Sheridan, K.V.: 1962, On the Relative Position and Origin of Harmonics in the Spectra of Solar Radio Bursts of Spectral Types II and III. *Australian Journal of Physics* **15**, 180. DOI. ADS.

Spangler, S.R.: 2005, The Strength and Structure of the Coronal Magnetic Field. *Space Sci. Rev.* **121**, 189. DOI. ADS.

Srivastava, N., Venkatakrishnan, P.: 2002, Relationship between CME Speed and Geomagnetic Storm Intensity. *Geophys. Res. Lett.* **29**, 1287. DOI. ADS.

Stewart, R., *et al.*: 1965, Solar radio bursts of spectral type v. *Australian Journal of Physics* **18**(2), 143.

Stewart, R.T., McLean, D.J.: 1982, Correcting low-frequency solar radio source positions for ionospheric refraction. *Pub. Astron. Soc. Aust.* **4**, 386. ADS.

Stix, M.: 2004, *The sun : an introduction*. ADS.

Stutzman, W., Thiele, G.: 1981, *Antenna the-ory and design*, New York: Wiley.

Suzuki, S., Dulk, G.A.: 1985, In: McLean, D.J., Labrum, N.R. (eds.) *Bursts of Type III and Type V*, 289. ADS.

Tapping, K.F.: 1978, Meter wavelength pulsating bursts during the May 21, 1972, solar noise storm. *Solar Phys.* **59**, 145. DOI. ADS.

Temmer, M., Veronig, A.M., Vršnak, B., Rybák, J., Gömöry, P., Stoiser, S., Maričić, D.: 2008, Acceleration in Fast Halo CMEs and Synchronized Flare HXR Bursts. *Astrophys. J. Lett.* **673**, L95. DOI. ADS.

Temmer, M., Veronig, A.M., Kontar, E.P., Krucker, S., Vršnak, B.: 2010, Combined STEREO/RHESSI Study of Coronal Mass Ejection Acceleration and Particle Acceleration in Solar Flares. *Astrophys. J.* **712**, 1410. DOI. ADS.

Tesla, N.: 1912, The disturbing influence of solar radiation on the wireless transmission of energy. *Electrical Review and Western Electrician*.

Thompson, B.J., Cliver, E.W., Nitta, N., Delannée, C., Delaboudinière, J.-P.: 2000, Coronal dimmings and energetic CMEs in April-May 1998. *Geophys. Res. Lett.* **27**, 1431. DOI. ADS.

Tian, H., DeLuca, E., Cranmer, S., De Pontieu, B., Peter, H., Martínez-Sykora, J., Golub, L., McKillop, S., Reeves, K.K., Miralles, M., *et al.*: 2014, Prevalence of small-scale jets from the networks of the solar transition region and chromosphere. *Science* **346**(6207), 1255711.

Tomczyk, S., Card, G.L., Darnell, T., Elmore, D.F., Lull, R., Nelson, P.G., Streander, K.V., Burkepile, J., Casini, R., Judge, P.G.: 2008, An Instrument to Measure Coronal Emission Line Polarization. *Solar Phys.* **247**, 411. DOI. ADS.

Townes, C.H.: 1957, Microwave and radio-frequency resonance lines of interest to radio astronomy. In: van de Hulst, H.C. (ed.) *Radio astronomy*, *IAU Symposium* **4**, 92. ADS.

Tun, S.D., Vourlidas, A.: 2013, Derivation of the Magnetic Field in a Coronal Mass Ejection Core via Multi-frequency Radio Imaging. *Astrophys. J.* **766**, 130. DOI. ADS.

Vaidyanathan, P.P.: 1990, Multirate digital filters, filter banks, polyphase networks, and applications: a tutorial. *Proceedings of the IEEE* **78**(1), 56.

van de Hulst, H.C.: 1950, The electron density of the solar corona. *Bulletin of the Astronomical Institutes of the Netherlands* **11**, 135. ADS.

van Haarlem, M.P., Wise, M.W., Gunst, A.W., Heald, G., McKean, J.P., Hessels, J.W.T., de Bruyn, A.G., Nijboer, R., Swinbank, J., Fallows, R., Brentjens, M., Nelles, A., Beck, R., Falcke, H., Fender, R., Hörandel, J., Koopmans, L.V.E., Mann, G., Miley, G., Röttgering, H., Stappers, B.W., Wijers, R.A.M.J., Zaroubi, S., van den Akker, M., Alexov, A., Anderson, J., Anderson, K., van Ardenne, A., Arts, M., Asgekar, A., Avruch, I.M., Batejat, F., Bähren, L., Bell, M.E., Bell, M.R., van Bemmel, I., Bennema, P., Bentum, M.J., Bernardi, G., Best, P., Bîrzan, L., Bonafede, A., Boonstra, A.-J., Braun, R., Bregman, J., Breitling, F., van de Brink, R.H., Broderick, J., Broekema, P.C., Brouw, W.N., Brüggen, M., Butcher, H.R., van Cappellen, W., Ciardi, B., Coenen, T., Conway, J., Coolen, A., Corstanje, A., Damstra, S., Davies, O., Deller, A.T., Dettmar, R.-J., van Diepen, G., Dijkstra, K., Donker, P., Doorduin, A., Dromer, J., Drost, M., van Duin, A., Eislöffel, J., van Enst, J., Ferrari, C., Frieswijk, W., Gankema, H., Garrett, M.A., de Gasperin, F., Gerbers, M., de Geus, E., Grießmeier, J.-M., Grit, T., Gruppen, P., Hamaker, J.P., Hassall, T., Hoeft, M., Holties, H.A., Horneffer, A., van der Horst, A., van Houwelingen, A., Huijgen, A., Iacobelli, M., Intema, H., Jackson, N., Jelic, V., de Jong, A., Juette, E., Kant, D., Karastergiou, A., Koers, A., Kollen, H., Kondratiev, V.I., Kooistra, E., Koopman, Y., Koster, A., Kuniyoshi, M., Kramer, M., Kuper, G., Lambropoulos, P., Law, C., van Leeuwen, J., Lemaitre, J., Loose, M., Maat, P., Macario, G., Markoff, S., Masters, J., McFadden, R.A., McKay-Bukowski, D., Meijering, H., Meulman, H., Mevius, M., Middelberg, E., Millenaar, R., Miller-Jones, J.C.A., Mohan, R.N., Mol, J.D., Morawietz, J., Morganti, R., Mulcahy, D.D., Mulder, E., Munk, H., Nieuwenhuis, L., van Nieuwpoort, R., Noordam, J.E., Norden, M., Noutsos, A., Offringa,

A.R., Olofsson, H., Omar, A., Orrú, E., Overeem, R., Paas, H., Pand ey-Pommier, M., Pandey, V.N., Pizzo, R., Polatidis, A., Rafferty, D., Rawlings, S., Reich, W., de Reijer, J.-P., Reitsma, J., Renting, G.A., Riemers, P., Rol, E., Romein, J.W., Roosjen, J., Ruiter, M., Scaife, A., van der Schaaf, K., Scheers, B., Schellart, P., Schoenmakers, A., Schoonderbeek, G., Serylak, M., Shulevski, A., Sluman, J., Smirnov, O., Sobey, C., Spreeuw, H., Steinmetz, M., Sterks, C.G.M., Stiepel, H.-J., Stuurwold, K., Tagger, M., Tang, Y., Tasse, C., Thomas, I., Thoudam, S., Toribio, M.C., van der Tol, B., Usov, O., van Veelen, M., van der Veen, A.-J., ter Veen, S., Verbiest, J.P.W., Vermeulen, R., Vermaas, N., Vocks, C., Vogt, C., de Vos, M., van der Wal, E., van Weeren, R., Weggemans, H., Weltevrede, P., White, S., Wijnholds, S.J., Wilhelmsson, T., Wucknitz, O., Yatawatta, S., Zarka, P., Zensus, A., van Zwieten, J.: 2013, LOFAR: The LOw-Frequency ARray. *Astron. Astrophys.* **556**, A2. DOI. ADS.

Veronig, A.M., Muhr, N., Kienreich, I.W., Temmer, M., Vršnak, B.: 2010, First observations of a dome-shaped large-scale coronal extreme-ultraviolet wave. *Astrophys. J. Lett.* **716**, L57. DOI. ADS.

Vršnak, B., Cliver, E.W.: 2008, Origin of coronal shock waves. *Solar Physics* **253**(1-2), 215.

Vrsnak, B., Ruzdjak, V., Zlobec, P., Aurass, H.: 1995, Ignition of MHD shocks associated with solar flares. *Solar Phys.* **158**, 331. DOI. ADS.

Vršnak, B.: 2001, Solar flares and coronal shock waves. *J. Geophys. Res.* **106**, 25291. DOI. ADS.

Vršnak, B., Cliver, E.W.: 2008, Origin of Coronal Shock Waves. Invited Review. *Solar Phys.* **253**, 215. DOI. ADS.

Vršnak, B., Magdalenić, J., Aurass, H., Mann, G.: 2002, Band-splitting of coronal and interplanetary type II bursts. II. Coronal magnetic field and Alfvén velocity. *Astron. Astrophys.* **396**, 673. DOI. ADS.

Švestka, Z.: 1966, Optical Observations of Solar Flares. *Space Science Reviews* **5**(3), 388. DOI. ADS.

Wakabayashi, R., Shimada, K., Kawakami, H., Sato, G.: 1999, Circularly polarized log-periodic dipole antenna for emi measurements. *IEEE transactions on electromagnetic compatibility* **41**(2), 93.

Wang, T., Davila, J.M.: 2014, Validation of Spherically Symmetric Inversion by Use of a Tomographically Reconstructed Three-Dimensional Electron Density of the Solar Corona. *Solar Phys.* **289**, 3723. DOI. ADS.

Wang, T., Reginald, N.L., Davila, J.M., St. Cyr, O.C., Thompson, W.T.: 2017, Variation in Coronal Activity from Solar Cycle 24 Minimum to Maximum Using Three-Dimensional Reconstructions of the Coronal Electron Density from STEREO/COR1. *Solar Phys.* **292**, 97. DOI. ADS.

Warmuth, A., Mann, G.: 2005, A model of the Alfvén speed in the solar corona. *Astronomy and Astrophysics* **435**(3), 1123. DOI. ADS.

Warmuth, A., Vršnak, B., Magdalenić, J., Hanslmeier, A., Otruba, W.: 2004, A multi-wavelength study of solar flare waves. I. Observations and basic properties. *Astron. Astrophys.* **418**, 1101. DOI. ADS.

White, S.M.: 2004, Coronal Magnetic Field Measurements Through Gyroresonance Emission. In: Gary, D.E., Keller, C.U. (eds.) *Astrophysics and Space Science Library*, *Astrophysics and Space Science Library* **314**, 89. DOI. ADS.

Wiegelmann, T., Petrie, G.J.D., Riley, P.: 2017, Coronal Magnetic Field Models. *Space Sci. Rev.* **210**, 249. DOI. ADS.

Wild, J.P., McCready, L.L.: 1950, Observations of the Spectrum of High-Intensity Solar Radiation at Metre Wavelengths. I. The Apparatus and Spectral Types of Solar Burst Observed. *Australian Journal of Scientific Research A Physical Sciences* **3**, 387. DOI. ADS.

Wild, J.P., Smerd, S.F.: 1972, Radio Bursts from the Solar Corona. *Annurev.aa.* **10**, 159. DOI. ADS.

Wild, J.P., Smerd, S.F., Weiss, A.A.: 1963, Solar Bursts. *Annurev.aa.* **1**, 291. DOI. ADS.

Wilson, T.L., Rohlfs, K., Hüttemeister, S.: 2009, *Tools of Radio Astronomy*. DOI. ADS.

Zhang, J., Cheng, X., Ding, M.: 2012, Observation of an evolving magnetic flux rope before and during a solar eruption. *Nat. Comm.* **3**, 747. DOI. ADS.

Zhang, J., Wang, J., Deng, Y., Wu, D.: 2001, Magnetic Flux Cancellation Associated with the Major Solar Event on 2000 July 14. *Astrophys. J. Lett.* **548**, L99. DOI. ADS.

Zimovets, I., Vilmer, N., Chian, A.C.-L., Sharykin, I., Struminsky, A.: 2012, Spatially resolved observations of a split-band coronal type II radio burst. *Astron. Astrophys.* **547**, A6. DOI. ADS.

Zirin, H.: 1988, *Astrophysics of the sun*. ADS.

Zirker, J.: 1995, Book review: Total eclipses of the sun/princeton u press, 1981; paperback 1995. *Journal of the British Astronomical Association* **105**, 187.

Zlotnik, E.Y., Klassen, A., Klein, K.-L., Aurass, H., Mann, G.: 1998, Third harmonic plasma emission in solar type II radio bursts. *Astron. Astrophys.* **331**, 1087. ADS.

Zucca, P., Carley, E.P., Bloomfield, D.S., Gallagher, P.T.: 2014a, The formation heights of coronal shocks from 2D density and Alfv́en speed maps. *Astron. Astrophys.* **564**, A47. DOI. ADS.

Zucca, P., Pick, M., Démoulin, P., Kerdraon, A., Lecacheux, A., Gallagher, P.T.: 2014b, Understanding Coronal Mass Ejections and Associated Shocks in the Solar Corona by Merging Multiwavelength Observations. *Astrophys. J.* **795**, 68. DOI. ADS.

List of Corrections

I thank the referee for his valuable comments. I have revised the thesis on the suggested lines and addressed the concerns raised by the referee. Following are the list of corrections made in the thesis.
I would like to note that the page numbers in referee comments are with respect to the old thesis and the page numbers in the reply are according to the corrected version of the thesis.

Referee's comments and my replies:

1. Page iii, Abstract. Try to make it clear as to which aspects of the instrument you dealt with and which part was done by others both in the first and second polarimeter described in the thesis.

Reply: In Page iii, the abstract has been modified and rephrased to highlight the work done by me.

2. Page v, Abstract. Has the DCP acronym been defined earlier? If not, say Degree of Circular Polarization (DCP); better would be to state in the earlier page where you mentioned it first.

Reply: In page iv, I have added 'dcp' as an acronym for 'degree of circular polarization'.

3. Page 8, Chapter 1. there X-ray brightness?? Or their X-ray brightness.

Reply: In page 8, the word 'there' has been replaced with 'their'.

4. Page 9, Chapter 1. No comment.

Reply: -

5. Page 9, Chapter 1. but failed (delete were).

Reply: In page 9, the word 'were' has been deleted.

6. Page 10, Chapter 1. contour map (160 MHz) showing.

Reply: In page 10, the caption of Fig. 1.9 has been modified as per the suggestions made.

7. Page 10, Chapter 1. Burke, B. F., and Franklin, K. L., J. Geophy. Res., 60, 213 (1955) on sporadic emission from Jupiter at 22 MHz was an important addition.

Reply: In page 10, the reference 'sporadic emission from Jupiter at 22 MHz by Burke and Franklin in 1955' has been added.

8. Page 10, Chapter 1. Sun is not a discrete source! It is 30 arcmin wide! It has a few discrete sources from time to time due to the emergence of active regions. Sun

is, of course, a radio source.

Reply: In page 10, the word 'discrete' has been removed from the sentence.

9. Page 11, Chapter 1. This can be controversial! It was not Mclean and Labrum, but Ms. Ruby Payne-Scott who helped to establish the field of radio astronomy in 1940 by using radio waves to detect solar bursts, but she was forced to resign after she got married. Better to delete this line in the thesis. You can use any result from their paper, though. Before them, there are tons of people who have done solar work, including Profs. Mukul Kundu, Paul Wild, Govind Swarup and others.

Reply: In page 11, McLean and Labrum (1985b) was used as reference to mention the contribution from Heavyside, Lorentz, Schott, Tonks and Langmuir. I have modified the sentence to '(refer McLean and Labrum (1985b) and the references therein for more details)'. I have also added a few sentences to highlight the works of the pioneers in the field as mentioned in the comment. There were several important milestones in solar radio astronomy; to name a few: observations of radio emission from the Sun by Pawsey, Payne-Scott, and McCready in 1946, solar radio noise by Allen in 1947, study of the slow drifting radio bursts by Wild and McCready in 1950, continuum burst observations by Boischot in 1957, type II radio bursts by Roberts in 1959, interferometric studies of continuum bursts by Kundu and Firor in 1961, radio spectrum of solar activity by Maxwell, Swarup, and Thompson in 1958.

10. Page 14, Chapter 1. Strictly speaking few means none! 'a few' means 2 or 3! Replace all 'few' as appropriate by 'a few'!!

Reply: In page 14, the word 'few' is replaced with 'a few'. 'Few' has been replaced with 'a few' wherever required.

11. Page 15, Chapter 1. same comment as on page 41, where ever you have written 'few'!

Reply: In page 15, the word 'few' has been replaced with 'a few'.

12. Page 16, Chapter 1. same comment as before for 'few'

Reply: In page 16, the word 'few' has been replaced with 'a few'.

13. Page 16, Chapter 1. same comment as before for 'few'

Reply: In page 17, the word 'few' has been replaced with 'a few'.

14. Page 18, Chapter 1. delete s in transients (transient).

Reply: In page 18, the word 'transients' has been replaced with 'transient'.

15. Page 20, Chapter 2. Why is this titled 15-18 MHz? The description is for 15 -85 MHz! Is it a typo?

Reply: In page 21, it was a typo. The word '18' has been replaced with '85'.

16. Page 21, Chapter 2. Who is this We? Is it only you or a team? In such places, try to be specific. If it is 'Royal We', remove it and replace with I!

Reply: In page 22, the word 'we' has been replaced with 'I' in this sentence and in the other sentences wherever required.

17. Page 24, Chapter 2. Normally acceptable, but you need to give an explanation as to why you are getting such a high value at 35 MHz. It could have been tweaked down to less than 3!

Reply: Since this log-periodic antenna was designed for low frequencies, the length of the dipole arms were longer. I have used supporting-structures to avoid the sagging of the dipole arms of the antenna. Due to this reason, the VSWR values are higher than 3.0 at a few frequencies.

18. Page 25, Chapter 2. you need to define the insertion loss numbers. It may be small, but the measurement is to be recorded.

Reply: In page 26, the insertion loss value (0.2 dB) has been included.

19. Page 36, Chapter 2. 3.5 dB corresponds to only a factor of 2.3. But the SNR is 31? It should correspond to 14 dB or so. Isn't it?

Reply: In page 37, the improved SNR is $\sim$ 14.5 dB. It has been corrected.

20. Page 36, Chapter 2. delete 'the'.

Reply: In page 37, the word 'the' has been deleted.

21. Page 39, Chapter 2. Since this is a chapter on the low frequency spectrometer in the thesis, the author needs to make it clear who built the spectrometer and what role she had in it. I am not seeing any reference to the built spectrometer. Was it only presented in a conference?

Reply: In page 41, the spectro-polarimeter front-end and back-end were designed, developed and characterized by me. This was presented at the International Space Weather Initiative Workshop, 2019 at the International Centre for Theoretical Physics, Italy (Link: http://indico.ictp.it/event/8682/session/5/contribution/13; Kumari *et al.* (2019b); Barve *et al.* (2019)). The manuscript is under preparation and shall be submitted to the Journal of Astronomical Telescopes, Instruments, and Systems (JATIS) shortly. The other members gave their suggestions during the development and characterization of the spectro-polarimeter. I have changed the text in this chapter from 'we' to 'I'.

22. Page 47, Chapter 2. A line explaining why you took that value?

Reply: In page 49, this was the minimum value of γ for which the mach number was positive (Gopalswamy *et al.*, 2012). This has been added in the corrected version of the thesis.

23. Page 49, Chapter 2. A line explaining why your (Kwon's) result differs significantly from Dulk and Melrose or Kwon et al (2013 b)?

Reply: In page 49, We find that the $B(r)$ curve obtained in this study matches the result of Kwon *et al.* (2013a) as it is within the error bar of our results. The power law index value computed by Dulk and McLean (1978) is 1.5 whereas the B field associated with the Type-II burst presented in this chapter seems to be steeper. This has been added in the corrected version of the thesis.

24. Page 52, Chapter 3. Will it be useful to say here that these lengths were modified later to bring down the resonant peaks seen in the VSWR?

Reply: In page 53, the table 3.1 caption has been modified.

25. Page 57, Chapter 3. Effective area calculation of a LPDA is a bit tricky. It will be worth describing it.

Reply: In page 57, I have described the procedure in the corrected version of the thesis. The half power beam width in E and H plane were used to obtain the directional gain of an antenna. This directional gain value was used to calculate the effective collecting area of the antenna.

$$A_e = \frac{\lambda^2}{4\pi} \times G \tag{6.1}$$

where, A_e, λ and G are the total effective collecting area, observational wavelength and gain, respectively.

$$G = \frac{4\pi \frac{180}{\pi}^2}{HPBW_E \times HPBW_H} dBi \tag{6.2}$$

where, $HPBW_E$ and $HPBW_H$ are the HPBW in E and H planes, respectively.

26. Page 64, Chapter 3. Why 800 MHz? It should be 1000 MHz as mentioned in the next page!

Reply: In page 66, to operate the ADC/FPGA in the safer range, we have reduced the sampling rate from 1000 MHz/s (maximum limit) to 800 MHz/s. This was mentioned in the text already and, hence the sentence has been retained.

27. Page 65, Chapter 3. Replace sapling with sampling!

Reply: In page 66, the word 'sapling' has been replaced with 'sampling'.

28. Page 66, Chapter 3. A better description of the various spikes and the step in the middle (2.5 units of time) of the graph?

Reply: In page 67, the three peaks at time samples $\sim$ 7500, 12500 and 37500 are due to the Global Positioning System (GPS) satellites[9]. The narrow band spikes in the data are due to local RFIs. The step at $\sim$ 26000 time sample is because of

[9] https://www.spaceacademy.net.au/spacelink/radiospace.htm

the occasional gain compression of the ADC.

29. Page 69, Chapter 3. Rather than saying heliocentric distance you could simply say 'in terms of distance from the Sun, solar radius being R'. Usually Heliocentric distance refers to the distance between nearby celestial bodies within the solar system in terms of 1 AU.

Reply: In page 71, I have changed 'heliocentric distance' to 'distance from the Sun'.

30. Page 70, Chapter 3. 80 MHz? Not clear because you have talked above a big range of 500 to 50 MHz.

Reply: In page 72, GRAPH is an existing imaging instrument at the Gauribidanur Radio Observatory and the data were available at only one frequency on the day of observation. I have used GRAPH radio images to compliment the observations with the wideband spectro-polarimeter.

31. Page 85, Chapter 4. How does the density vary with frequency and as a function of distance?

Reply: In page 87, I have modified figure 4.6 by having added the frequency scale on the top x-axis.

32. Page 102, Chapter 6. a few ! Candidate should know the difference between 'few' and 'a few'!

Reply: In page 104, the word 'few' has been replaced with 'a few'. 'Few' has been replaced with 'a few' wherever required.

33. Page 102, Chapter 6. A few

Reply: In page 104, the word 'few' has been replaced with 'a few'.

34. Page 103, Chapter 6. In a summary, one should define various parameters like va, Me, Ne, etc and their units.

Reply: In page 105, this has been incorporated in the corrected version of the thesis.

35. Page 105, Chapter 6. Delete 'Nobility' and replace with 'Novelty'! Nobility is an absurd word in this context! In the next line 'noble' is to be replaced by 'novel;.

Reply: In page 107, the spellings have been corrected.

36. Page 106, Chapter 6. How did the 1 bit number become 1084? If it is a 10 bit ADC, it should be 1024?

Reply: In page 108, this has been modified.